0 0 0 0 4 7 0 6 3 2 7

LBL-5947 c.1
UC-90
TID-4500-R65

For Reference

Not to be taken from this room

Energy and Environment Division

The Furnace Combustion and Radiation Characteristics Of Methanol And A Methanol/Coal Slurry

William Lytle Grosshandler

January 1977

Lawrence Berkeley Laboratory University of California/Berkeley

Prepared for the U.S. Energy Research and Development Administration under Contract No. W-7405-ENG-48

LBL-5947 c.1

LEGAL NOTICE

This report was prepared as an account of work sponsored by the United States Government. Neither the United States nor the United States Energy Research and Development Administration, nor any of their employees, nor any of their contractors, subcontractors, or their employees, makes any warranty, express or implied, or assumes any legal liability or responsibility for the accuracy, completeness or usefulness of any information, apparatus, product or process disclosed, or represents that its use would not infringe privately owned rights.

Printed in the United States of America
Available from
National Technical Information Service
U.S. Department of Commerce
5285 Port Royal Road
Springfield, Virginia 22161
Price: Printed Copy $8.50; Microfiche $3.00

0 0 1 0 4 7 0 0 3 2 8

THE FURNACE COMBUSTION AND RADIATION CHARACTERISTICS OF METHANOL AND A METHANOL/COAL SLURRY

by

William Lytle Grosshandler

Principal Investigator: Robert F. Sawyer

January 1977

ABSTRACT

An experimental facility has been built to study the combustion of methanol and a slurry of methanol plus 5% coal in an environment similar to industrial and utility boilers. The furnace is a horizontal water cooled cylinder, 20 cm in diameter by one meter long, with a firing rate of 60 kW. The measurements taken throughout the furnace include temperature and concentration of carbon monoxide, carbon dioxide, water, oxides of nitrogen, methanol and particulates. Spectral radiation intensity measurements are taken along the axis of the furnace burning methanol and the methanol/coal slurry.

The effect of the fuel on flame structure is reported. The temperatures in the pure methanol flame are, in general, higher than in the methanol/coal flame. The levels of the oxides of nitrogen are low in the pure methanol flame (less than 20 ppm NO). Addition of 5% coal to the methanol causes NO concentration to increase to 100 ppm. This represents a conversion of 40% of the coal bound nitrogen to NO. Particulate levels increase from less than .001 g/m^3 for the pure methanol to over .25 g/m^3 when pulverized coal is added.

The low levels of soot and particulates in the methanol flame have an effect on the spectral intensity. No continuous radiation is measured in the methanol flame, but small amounts of particulate radiation can be seen from the spectra of the methanol/coal flame. The total emittance of the flame is increased from about .10 to .135 with the addition of 5%

pulverized coal, but the radiation intensity is reduced because of the lower flame temperatures. This effect is partly due to the presence of the coal particles and partly due to the different nozzle which is used to burn the slurry.

A numerical program has been written to calculate the spectral intensity from an inhomogeneous mixture of combustion products. Comparisons are made between the calculated intensity and the measured intensity for both fuel systems. The results of other simplified models are also mentioned. The numerical results are about 25% lower than the measured results. Reasons for this are discussed.

PREFACE

This report has been extracted from the doctoral thesis of W. L. Grosshandler, "A Study of a Model Furnace Burning Methanol and Methanol/Coal Slurry" (Grosshandler, 1976), which was prepared and submitted to the Graduate Division of the University of California. These studies were conducted in the Combustion Laboratories of the Department of Mechanical Engineering, College of Engineering, University of California, Berkeley.

In addition to the material of this report, the thesis contains a detailed description of the experimental apparatus and its operation, background information on the analytical instrumentation used, a listing and description of computer codes used in data analysis and modeling of the combustion and radiation processes, a review of the chemical kinetics of the oxidation of methanol, and a compilation of the experimental data.

The current address of the primary author is: Professor W. L. Grosshandler, Mechanical Engineering Department, Washington State University, Pullman, Washington, 99163.

0 0 0 0 4 7 0 5 3 3 0

TABLE OF CONTENTS

	Page
ABSTRACT	i
PREFACE	iii
TABLE OF CONTENTS	iv
LIST OF FIGURES	vii
LIST OF TABLES	x
NOMENCLATURE	xi
CHAPTER I. Introduction	1
A. Background	1
B. Purpose of Present Study	3
CHAPTER II. Design of the Furnace	8
A. Sizing the Model Furnace	8
B. Major Component Design	9
1. Primary and Secondary Air Delivery System.	9
2. Fuel Delivery System	12
3. Igniter System	14
4. Burner Assembly	15
5. Combustion Chamber	20
6. Exhaust System	20
CHAPTER III. Instrumentation of the Furnace	21
A. Temperature Measurement	21
B. Chemical Composition Measurement	29
1. Sampling Probes	29
2. Sample Analyzers	30

TABLE OF CONTENTS (Continued)

Page

a. Beckman Infrared Analyzers 33

b. Gas Chromatograph 33

c. Chemiluminescent Analyzer 35

3. Sample Transferring Sections 41

C. Particulate Measurement 43

D. Radiation Measurement 46

CHAPTER IV. Structure of the Furnace Flames 51

A. Methanol as the Fuel 51

1. Temperature 51

2. Chemical Composition 56

3. Comparison of Structure with Theoretical Predictions 70

B. Methanol/Coal Slurry as the Fuel 77

1. Temperature Composition 77

2. Chemical Composition 80

CHAPTER V. Modeling of Radiation from Furnace Flames 87

A. Fundamentals of Radiation 87

1. Radiation from Surfaces 87

2. Radiation from Particles 89

3. Radiation from Gases 92

4. The Equation of Transfer 99

B. Calculation of Radiation Properties 101

1. Particle Radiation 101

2. Gas Radiation 103

C. Computational Procedure for Integration of Equation of Transfer 109

TABLE OF CONTENTS (Continued)

		Page
CHAPTER VI.	Results of Radiation Measurements in the Furnace . .	113
	A. Methanol as the Fuel	113
	B. Methanol/Coal Slurry as the Fuel	122
	C. Comparison of Results to Those of Radiation Models	129
	D. Comparison of Results to Those of Other Experimenters	143
CHAPTER VII.	Conclusions	150
	A. Summary of Results	150
	B. Conclusions	151
REFERENCES		153

LIST OF FIGURES

Figure		Page
II-1.	Flow Diagram of Methanol Furnace	10
II-2.	Furnace and Control Panel	11
II-3.	Burner Assembly for Methanol Furnace	16
II-4.	Liquid Fuel Atomizers	17
III-1.	Thermocouple Probe	23
III-2.	Temperatures and Calculated Emissivity for Pt/Pt-13% Rh Thermocouple	27
III-3.	Gas Sampling Probe	31
III-4.	Quartz Sample Probe Mounted on Traverse Mechanism	32
III-5.	Elements of the Gas Chromatographic System	34
III-6.	Chromatogram of Sample Taken from Methanol Furnace. (Operating conditions are as shown in Table III-2.)	37
III-7.	Components of Chemiluminescent Analyzer	38
III-8.	Schematic of Sample Transfer Systems	42
III-9.	Particulate Probe and Collection System	45
III-10.	Radiation Measurement Equipment	47
III-11.	Output of Monochromator Detector With and Without Polystyrene Film in Front of Window	50
IV-1.	Temperature (K) Distribution in Methanol Furance (uncorrected)	52
IV-2.	Temperature Profiles in Methanol Furnace	54
IV-3.	Distribution of H_2O Concentration (%, vol.) in Methanol Furnace	58
IV-4.	Distribution of CO Concentration (%, vol.) in Methanol Furnace	60

LIST OF FIGURES (Continued)

Figure		Page
IV-5.	Distribution of CO_2 Concentration (%, vol.) in Methanol Furnace	61
IV-6.	Chemical Composition of Methanol Furnace	62
IV-7.	Distribution of NO Concentration (ppm, vol.) in Methanol Furnace	66
IV-8.	Distribution of NX Concentration (ppm, vol.) in Methanol Furnace	67
IV-9.	Profiles of NO and NX in Methanol Furnace	68
IV-10.	Grid System Used for Computer Simulation of Methanol Furnace	72
IV-11.	Computer Predicted Velocity Profiles in Methanol Furnace	75
IV-12.	Temperature Profiles: Predicted and Experimental . . .	76
IV-13.	CO_2 Concentration Profiles: Predicted and Experimental	76
IV-14.	Temperature Profiles (Corrected) Comparing Slurry to Pure Methanol.	78
IV-15.	CO_2 Concentration Profiles Comparing Slurry to Pure Methanol	81
IV-16.	NO and NX Concentration Profiles With Slurry as Fuel .	83
IV-17.	Particulate Concentration Profiles With Slurry as Fuel	85
IV-18.	Particulates Collected at Axial Position, x, and Radial Position, y, in a Methanol/5.3% Coal Flame	86
V-1.	Energy Transition for a Diatomic Gas	93
V-2.	Definition of Lorentz Profile Line Parameters	93
VI-1.	Visible Radiation from Experimental Furnace	114
VI-2.	Visible Particulate Radiation from First Three Ports of Furnace Burning Methanol/Coal Slurry	115
VI-3.	Measured Spectral Intensity (x = 12.7 cm)	116
VI-4.	Measured Spectral Intensity (x = 26.9 cm)	117
VI-5.	Measured Spectral Intensity (x = 58.4 cm)	119

LIST OF FIGURES (Continued)

Figure		Page
VI-6.	Measured Spectral Intensity (x = 86.9 cm)	120
VI-7.	Total Intensity Variation Along Axis of Methanol Furnace	121
VI-8.	Measured Spectral Intensity With 5% Coal (x = 26.9 cm) .	123
VI-9.	Measured Spectral Intensity With 5% Coal (x = 58.4 cm) .	124
VI-10.	Measured Spectral Intensity With 5% Coal (x = 86.9 cm) .	125
VI-11.	Spectral Emittance of Furnace Burning Methanol and a Methanol/Coal Slurry (x = 26.9 cm)	127
VI-12.	Total Intensity Variation Along Axis of Furnace	130
VI-13.	Calculated Spectral Intensity (x = 26.9 cm)	131
VI-14.	Calculated Spectral Intensity (x = 58.4 cm)	132
VI-15.	Calculated Spectral Intensity (x = 86.9 cm)	133
VI-16.	Calculated Spectral Intensity (x = 26.9 cm)	134
VI-17.	Calculated Spectral Intensity With 5% Coal (x = 58.4 cm)	135
VI-18.	Calculated Spectral Intensity With 5% Coal (x = 86.9 cm)	136
VI-19.	Calculated Spectral Intensity Assuming Homogeneous Equilibrium Concentrations and Experimental Temperatures (x = 58.4 cm)	140
VI-20.	Calculated Spectral Intensity Using Homogeneous Adiabatic Equilibrium Furnace Conditions	141
VI-21.	Calculated Spectral Intensity Using Furnace Conditions Predicted by Gosman Program (x = 58.4 cm)	142
VI-22.	Calculated Intensity Using Wide Band Model and Average Homogeneous Conditions (x = 58.4 cm)	144
VI-23.	Intensities and Emittances of Various Fuels and Furnace Systems	147
VI-24.	Spectral Emittance of a Furnace Burning City of Heavy Fuel Oil (from Sato, *et al.*, 1969)	149

LIST OF TABLES

Table		Page
I-1.	Costs of Various Fuels (From Reed and Lerner, 1973) . .	3
I-2.	Enthalpies of Combustion and Maximum Temperatures of Various Fuels With Air	4
I-3.	Minimum Premixed Air/Fuel Ratio Required to Suppress Carbon Formation in a Bunsen Burner Flame.	5
II-1.	Size of Furnace Systems	9
II-2.	Properties of Fuel	13
II-3.	Burner Design Characteristics	19
III-1.	Analysis Equipment for Measuring Chemical Species . . .	30
III-2.	Operating Conditions of Gas Chromatograph	36
III-3.	Chemiluminescent Analyzer Operating Conditions	40
III-4.	Operating Conditions for Infrared Radiation Measurements	49
IV-1.	Adiabatic Equilibrium Conditions for $CH_3OH(L)+\frac{1.5}{\Phi}(AIR)$.	57
IV-2.	Input Parameters for Numerical Model of Methanol Furnace	73
V.	Vibrational Spectra Data	104
VI-1.	Total Intensities of Experimental Measurements Compared to Calculated Intensities	137
VI-2.	Total Normal Emittance of Pure Methanol Flame	143

NOMENCLATURE

a	line width parameter
a_o	constant in size frequency distribution function
A	geometrical cross section
$\tilde{A}$	total projected area per unit volume of cloud
Ar	Archimedes number
b_o	constant in size frequency distribution function
B	molecular rotational constant
B_e	rotational constant at equilibrium bond length
c	velocity of light
c_o	constant in size distribution function
C	ratio of zeroth to first order term in expansion of electric dipole moment
C_1	first radiation constant
C_2	second radiation constant
d, D	diameter
$d_\nu(\omega)$	average line spacing
$(\overline{1/d})$	inverse line spacing parameter
D_e	correction factor for rotational-vibrational interaction
e	energy
$F(r)$	size frequency distribution function
g	acceleration due to gravity
g_i	degeneracy of energy level i
h	convective heat transfer coefficient, or Planck's constant

I	total intensity, W/cm^2-sr, or moment of inertia
I_ν	spectral intensity, W/cm^2-sr-sec^{-1}
I_λ	spectral intensity, W/cm^2-sr-μm
I_{b_λ}	spectral intensity of a blackbody
J	rotational quantum number
k	thermal conductivity
k'	spring constant
k_o	Boltzmann's constant
k_ν, k_ω	pressure absorption coefficient, $atm^{-1}cm^{-1}$
K	total extinction coefficient, cm^{-1}, or constant in effective viscosity equation (Chapter IV)
K_a	absorption coefficient, cm^{-1}
K_s	scatter coefficient, cm^{-1}
ℓ	path length, cm
m	J + 1 for R-branch, -J for P-branch
$\dot{m}_f$	mass flow rate of fuel
$\dot{m}_o$	mass flow rate of oxidizer
n_1, n_2	simple refractive indices of mediums 1 and 2
$N(r)$	size frequency distribution function per unit volume
N_i	number of molecules in state i
P	pressure
P_i	partial pressure of species i
Pr	Prandtl number
q_{cat}	catalytic heat flux
$q_{conduction}$	conducted heat rate
$q_{convection}$	convected heat rate
$q_{radiation}$	radiated heat rate

r	radius
r^*	radius separating small particle limit from large particle limit
R	outer radius of swirl generator
R_h	hub radius of swirl generator
S	integrated line strength, or swirl number (Chapter II)
$S_{\upsilon,J}^{\upsilon+1,J\mp1}$	integrated line strength for a particular vibrational-rotational transition
$(\overline{S/d})$	mean absorption coefficient
$(\overline{S^{1/2}/d})$	mean strong line parameter
T_g	gas temperature
T_j	thermocouple junction temperature
T_w	wall temperature
T_∞	representative gas temperature
u	velocity, or pressure path-length (Chapter V)
U	free stream velocity
υ	vibrational quantum number
V_f	fuel inlet velocity
V_o	oxidizer inlet velocity
$\tilde{V}$	particle volume per total cloud volume
W	length in effective viscosity equation; or effective line width (Chapter V)
$\tilde{W}$	particle load per unit volume of cloud
x	distance
x_e	correction factor for anharmonic vibration
X	optical depth
X_a	absorption efficiency factor
X_s	scatter efficiency factor
y_e	correction factor for anharmonic vibration
z_e	correction factor for anharmonic vibration

α	angle of swirl vane with swirl generator, or empirical constant in soot absorption coefficient (Chapter VI)
α_e	correction factor for rotational-vibrational interaction
α_λ	spectral absorptivity
$\alpha_\upsilon^{\upsilon+1}$	total band intensity for transition υ to $\upsilon+1$
β	transmittance parameter (Chapter III), angle of incidence (Chapter V), or empirical constant in soot absorption coefficient (Chapter VI)
γ_Δ	Doppler line half-width
γ_L	Lorentz line half-width
ε_j	emissivity of thermocouple junction
ε_λ	spectral emissivity
θ	angle relative to incident light
$\eta_{i,j}$	line broadening parameter
κ_1, κ_2	extinction coefficients in complex refractive indicies of mediums 1 and 2
λ	wavelength, μm
μ	reduced mass
μ_{eff}	effective turbulent viscosity
ν	vibration frequency, or kinematic viscosity (Chapter III)
ρ	density
ρ_λ	spectral reflectivity
$\rho'_{\lambda\|\|}$, $\rho'_{\lambda\perp}$	directional spectral reflectivities for parallel and perpendicular components of electromagnetic wave
σ	Stefan-Boltzmann constant
τ	transmittance
Φ_s, Φ_d	phase functions for specular and diffuse reflectors
χ	angle of refraction
ω	wave number, ν/c
Ω	solid angle

I. INTRODUCTION

A. Background

Much has been written lately about the problems of producing energy safely, efficiently and economically. Although many new and exciting techniques have been discussed, most ideas suffer from either the economic aspect (e.g. solar), or the public safety aspect (e.g. nuclear). While it is probable that these shortcomings will be overcome, fossil fuels are likely to dominate as the primary source of energy, at least throughout the remainder of this century.

Natural gas is the most desirable of the fossil fuels for producing energy because it can be burned without creating significant amounts of pollutants like carbon monoxide, sulfur dioxide, unburned hydrocarbons and particulates. The one pollutant which burning natural gas can create, nitric oxide, has been reduced from 50% to 80% in some existing power plants by using the techniques of staged combustion, reduced excess air and flue gas recirculation (Bagwell, et al., 1971; Barr and James, 1973). Unfortunately, the world's production of natural gas has probably peaked (Hubbert, 1971) and availability will decrease while energy demands increase.

Petroleum will be a feasible substitute for natural gas only for the next 50 years or so because even optimistic estimates predict the decline in oil production to begin around the turn of the century (Hubbert). The increased nitrogen content in new sources of petroleum, such as shale oil, will make emission control much more difficult than burning either the low sulfur oils currently in use or natural gas.

The most promising fossil fuel for the United States from the standpoint of availability is coal. Its production is not expected to peak until after 2100, and it will not drop back down to its present level until after 2350. This is especially important to the United States since 21% of the world's minable coal resources are located here (Hubbert). However, burning untreated coal in existing power plants results in high levels of particulates in addition to the sulfur and nitrogen oxides.

The problem of pollutant formation from coal can be attacked in three ways: modification of the coal before burning, modification of the combustion process, or clean-up of the stack gases. One way to modify the coal before it is burnt is to completely reform it to more desirable fuels such as methane, hydrogen, or methanol. Methanol is attractive because it is a liquid and can be stored and transported much more cheaply and safely than either methane or hydrogen. In pilot plant and full scale boiler demonstrations, both the carbon monoxide and nitric oxide levels were lower when burning methanol than when burning methane. Additionally, existing carbon deposits within the furnace were removed by burning methanol (Reed and Lerner, 1973).

Historically, methanol was produced by the destructive distillation of wood. Since 1925, most methanol has been synthesized by the reaction of carbon monoxide with hydrogen. The earlier processes required high pressures (300×10^5 N/m^2) at 200° C (Reed and Lerner). The Lurgi process is a recently perfected low pressure process (50×10^5 N/m^2) which passes the synthesis gas ($H_2 + CO_2 + CO$) over a copper catalyst. The synthesis gas can be made from heavy fuel oil, naptha, or natural gas. Imperial Chemical Industries (ICI) has developed its own low pressure methanol synthesis system which also uses a copper catalyst and naptha as feed stock (Hiller, et al., 1971). Two inter-

mediate pressure processes have been developed by Nissui-Tapso (Tani and Tukawa, 1971) and the Japan Gas Chemical Company (Morita, Takahashi, and Koseki, 1971). There is even some discussion of producing methanol as a by-product from the steel industry and the electric utility industry with coal as the fuel (Steinberg, et al., 1973). The possibility of an advanced combined cycle using nuclear energy and coal to produce electrical power and methanol is mentioned in the same reference.

TABLE I-1. COSTS OF VARIOUS FUELS (From Reed and Lerner, 1973)

Fuel	Raw Material	Cost, $\$/10^6$kJ
Methanol	Coal	1.40
	Lignite	1.18
	Natural Gas	1.49
Gasoline	Crude Oil	1.00
Methane (gas)	Well Head	.14-.37
	Imported LNG	.76-.95
	Coal	.76-.95
Hydrogen (gas)	Natural Gas	.92
	Coal	1.25

The economics of producing methanol and other fuels are compared in Table I-1. From these cost estimates it appears that methanol is not likely to dominate the fuel market in the near future. Because of its other advantages, it is likely to become an important alternative fuel, especially as the cost of natural gas and crude oil increase relative to the cost of coal.

B. Purpose of Present Study

With the increase in methanol usage almost a certainty, it becomes important to be able to predict how it will behave in a combustion system. In particular, how do the heat release rates and pollutant forming abilities of methanol compare to those of other fuels?

The enthalpy of reaction of liquid methanol with air is compared to that of other fuels in Table I-2 along with the adiabatic flame temperatures.

TABLE I-2.
ENTHALPIES OF COMBUSTION AND MAXIMUM TEMPERATURES OF VARIOUS FUELS WITH AIR
(298 K and 1.01×10^5 N/m^2)

Fuel	Enthalpy of Combustion kJ/g	kJ/mole	Equilibrium Adiabatic Stoichiometric Temperature
$CH_3OH(\ell)$	20.1	643	2152 K
CH_4	49.5	792	2226 K
H_2	50.2	1004	2382 K
#4 Fuel Oil	43.9	----	------
Bituminous Coal (Group 4)	31.4	----	------

The lower combustion temperature of methanol would lead one to predict lower nitric oxide production when compared to methane or other paraffinic compounds. This has been verified in tests with internal combustion engines (Adelman, Andrews, and Devoto; 1972) and in a steam boiler, as mentioned earlier. One purpose of the present study is to reconfirm the prediction of low nitric oxide concentrations from a methanol fueled furnace. Additionally, other pollutants were measured and the general structure of the flame determined by measuring concentrations of stable species and temperatures throughout the furnace.

The structure and temperature of a flame are not only important because of their influence on pollutant formation, but also because of their influence on the heat transfer from the combustion system. The heat transfer, pollutant formation, and efficiency of a combustion system are all tightly interrelated. Also, it is important to be able to predict the heat transfer from the flame to insure the mechanical integrity of the system. If methanol is to be burnt in existing boilers or gas turbines, it is important to be able to predict the heat transfer characteristics relative to those of other fuels. A decrease in flame radiation could cause higher temperatures

in the convective section of a furnace, possibly rupturing boiler tubes. Significantly less radiation in a gas turbine combustor could increase the liner life.

The two mechanisms involved in transferring heat from the flame of a combustion system are convection and radiation. The relative amounts by these two modes varies with the flame structure and composition. Radiation increases with fuels that form soot. Based upon studies by Street and Thomas (1955), there is reason to believe that methanol will produce much less soot in a turbulent diffusion flame than most other organic fuels. In their experiments, a Bunsen type burner was used in which the premixed air-fuel ratio was variable. The amount of premixed air was decreased until a luminous region just became visible. The minimum amount of air which was needed to produce a non-luminous flame was the criterion used to rate the soot forming ability of the organic compounds. The minimum air/fuel ratio needed to produce a non-luminous flame for different fuels is shown in Table I-3. There was no quantitative measurement for methane, but from personal experience with a laboratory Bunsen burner, if the air mixture is sufficiently decreased, the flame becomes luminous.

TABLE I-3. MINIMUM PREMIXED AIR/FUEL RATIO REQUIRED TO SUPPRESS CARBON FORMATION IN A BUNSEN BURNER FLAME (Street and Thomas, 1955)

Fuel	Air/Fuel	Equivalence Ratio
Methanol	0	∞
Ethanol	6.0	1.52
Ethane	9.7	1.67
Propane	10.1	1.56
iso Octane	10.5	1.45
n - Cetane	11.0	1.35
Acetylene	6.4	2.08
Benzene	9.3	1.43

Radiation from soot and particulates is the dominant source of radiation in coal and oil flames. Even for natural gas flames, continuous emission can contribute a significant amount to the total radiation. With no expected soot from a methanol flame, the total radiation can be predicted to be less than for any of the other fuels. Another purpose of this study is to measure this radiation and see how it varies with location and composition along the axis of the furnace.

If a mixture of coal and methanol could be burned as the furnace fuel, two benefits would be obtained. The first is that the mixture could serve as an extender for the more expensive pure methanol without a significant increase in pollutant emissions. Secondly, the continuous radiation from the coal particles would increase the total radiation from the flame, a generally desirable effect in utility boilers and steel furnaces.

A final intent of this study was to attempt to predict the radiation from the flame knowing the inhomogenous temperature and concentration distributions in the furnace.

To summarize, the primary goals in this work are listed here:

1. Measure the temperature distribution and composition of stable species in a flame similar to those found in utility boilers and industrial furnaces.
2. Measure the important pollutants emitted from a model furnace burning methanol.
3. Measure the spectral infrared radiation from this same furnace.

4. Determine the effect of adding coal to the methanol on pollutant emissions and infrared radiation.
5. Predict the spectral radiation from the furnace, with and without coal, based upon measured composition, temperature, and particulate profiles.

To accomplish the above objectives, a model furnace has been built with a thermal power output of 60 kw and a cylindrical water-cooled combustion chamber 1 meter long by 20 cm in diameter. The experimental measurements desired have been taken, and comparisons between measured radiation data and that predicted by a computer model have been made. All of this is reported in the following chapters.

The next chapter discusses the techniques involved in designing the furnace. Chapter III deals with the instrumentation required for the experimental measurements, and Chapter IV presents the results of the flame structure measurements. In Chapter V, a digression is made to allow for a discussion on the physics of radiation in general and, in particular, how it relates to radiation from combustion systems. This information is used to formulate a model for radiation from the methanol flame. Chapter VI presents the results of the radiation measurements for the furnace burning both pure methanol and methanol/coal slurries. Conclusions and recommendations are given in Chapter VII.

II. DESIGN OF THE FURNACE

The engineering literature contains many sources of information helpful in the design of a furnace. Fluid mechanical considerations are set forth in Combustion Aerodynamics by Beér and Chigier. The Journal of the Institute of Fuel has carried many articles applying fluid mechanics and heat transfer to the solution of practical furnace design problems (see reference list). Furnace and boiler manufacturers such as Combustion Engineering and Babcock and Wilcox have their own publications which also contain practical information for the designer. All of these references were consulted and contributed to the design of the experimental furnace.

A. Sizing the Model Furnace

Ideally, in an experiment modeling furnace combustion processes, the closer one can approach the size of a functional furnace the better. It is immediately obvious that the ideal is impossible to obtain in this case since even a small package boiler produces over 10,000 kW (Babcock and Wilcox). The size of different furnace systems is compared in Table II-1.

A 200 g/sec air flow rate for this study is the maximum which can be obtained with the existing laboratory compressor. Although the power input to the model furnace is orders of magnitude less than utility boilers the power density is actually larger. Radiant energy fluxes from the larger furnaces are typically 50 W/cm^2 while that of the IJmuiden furnace is about 40 W/cm^2. Maximum radiation flux in the model furnace is 5 W/cm^2.

TABLE II-1. SIZE OF FURNACE SYSTEMS

Furnace System	Thermal Power	Volume	Power Density[4]	Air Flow Rate
PG&E Pitts[1] Unit #7	2×10^6 kW			3×10^5 g/sec
PG&E Pitts[1] Unit #1	4×10^5 kW	2200 m^3	200 kW/m^3	6×10^4 g/sec
Package Boiler[2]	10^4-10^5 kW			
IJmuiden Model[3] Furnace	3×10^3 kW	25 m^3	120 kW/m^3	1200 g/sec
This Study	50-150 kW	.03 m^3	2000 kW/m^3	20-200 g/sec

1. Pacific Gas and Electric, Pittsburg Power Plant, Units 1-7.
2. Babcock and Wilcox.
3. Flame Radiation Research Joint Committee, 1953.
4. Based on total boiler volume. In the flame zone power densities for boilers are approximately 10 times greater.

B. Major Component Design

Figure II-1 shows a flow diagram of the major components of the model furnace. It consists of the primary air delivery system, the secondary air delivery system, the fuel delivery system, the igniter system, the burner assembly, the combustion chamber, and the exhaust system. A photograph of the entire furnace is in Figure II-2. A general description of the major components is given in this section.

1. Primary and Secondary Air Delivery Systems

The major portion of these sections was built by previous workers (Pratt, 1968; Samuelsen, 1970; Cernansky, 1974). All that remained was to adapt them to the new burner section and to verify existing, or install new, pressure gauges, thermocouples, rotameters, and manometers.

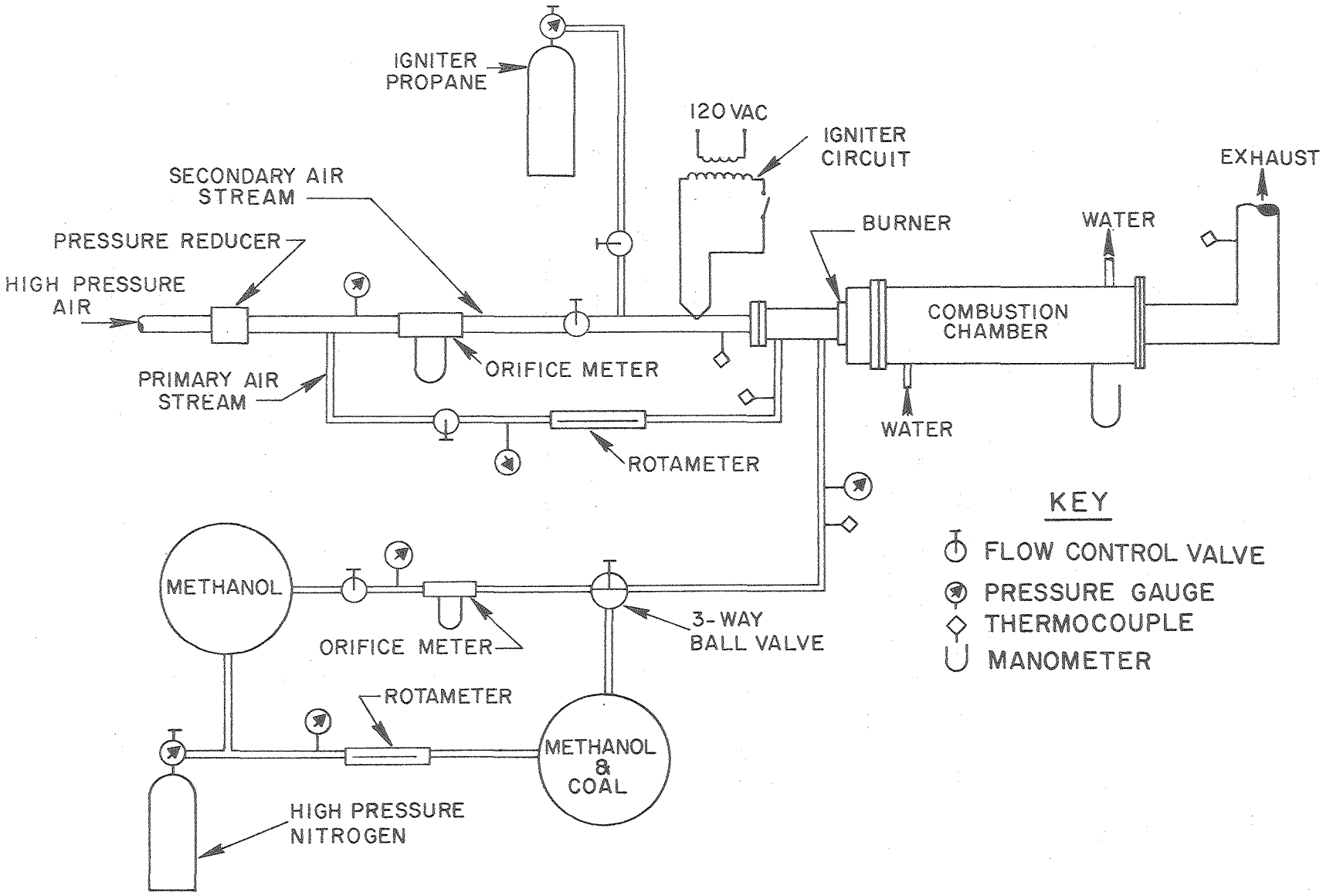

FIGURE II-1. Flow Diagram of Methanol Furnace

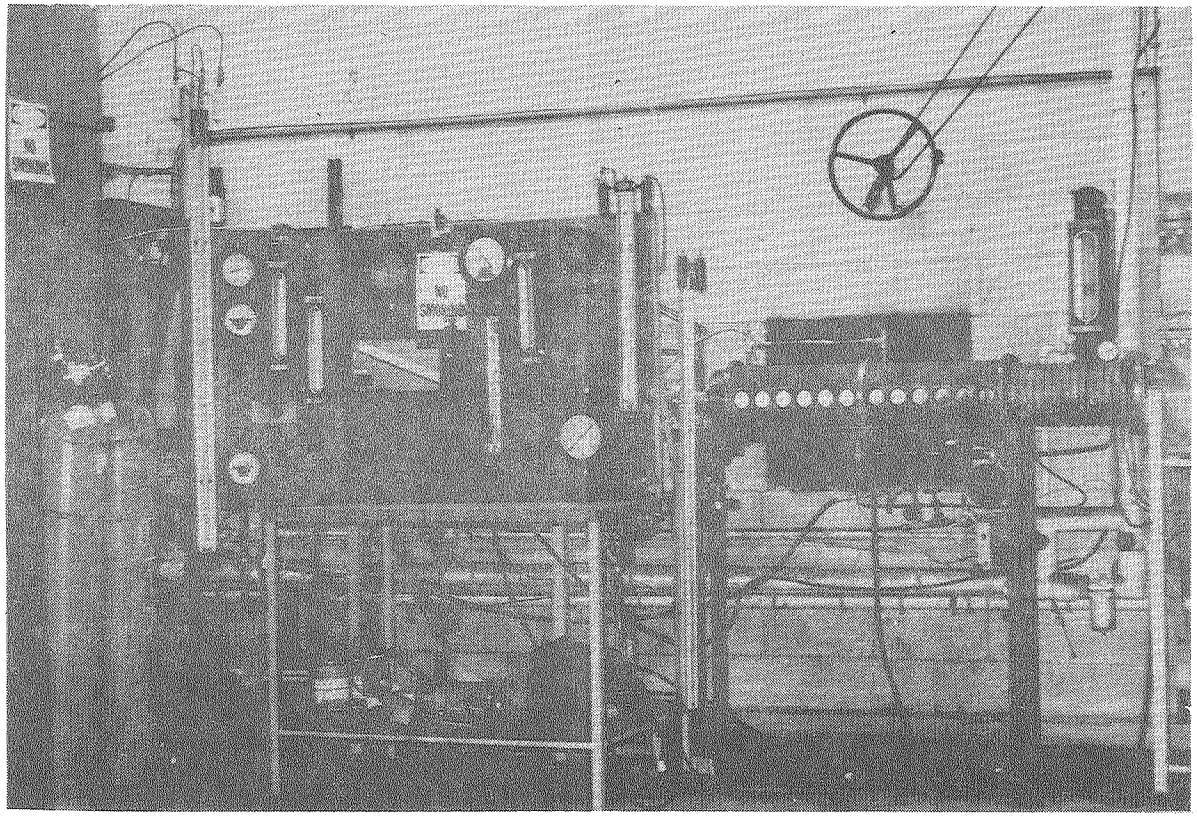

FIGURE II-2. Furnace and Control Panel

Air is supplied at 13.8 x 10^5 N/m^2 from an air compressor. The pressure is reduced to 5.5 x 10^5 N/m^2 before the flow is split into a primary and secondary stream (see Figure II-1). The major portion of the air goes to the secondary air system. This flow rate is measured with a calibrated orifice before it passes through a control valve. It then goes to the burner section.

The primary air flow is measured with a rotameter, controlled with a needle valve, and then enters the burner section. Pressure and temperature are monitored in both streams where the flow rate is measured and where the burner section is entered.

2. Fuel Delivery System

The fuels used are methanol and a methanol/coal slurry. Properties of methanol and the coal are listed in Table II-2. To provide methanol at the pressures desired (up to 8.5 x10^5 N/m^2 gauge), it is transferred by an air driven pump from a 54 gallon drum to a 34 ℓ pressure vessel safety tested to 13.6 x10^5 N/m^2 gauge and equipped with a pressure relief valve. The 34 ℓ vessel is pressurized with dry nitrogen. The high pressure methanol flow is metered with a needle valve and the flow rate is determined with a calibrated orifice. Pressure and temperature are monitored with a Bourdon gauge and thermocouple, respectively, both at the orifice and at the entrance to the burner (see Figure II-1).

Delivery of the methanol/coal slurry had two design difficulties: 1. keeping the coal in suspension and 2. preventing the coal from building up in the fuel lines and nozzle. The first problem is addressed by Rudzki, Pease, and Weidner (1965) for a mixture of fuel oil with pulverized coal. They discuss the effect of particle size, percentage of coal, type of coal, temperature of oil, and viscosity of

TABLE II-2.

Properties of Fuel

a) Methanol

Formula:	CH_3OH
Molecular Weight:	32.04 g/mole
Boiling Point @ 1atm:	338 K
Density @ 1atm, 298 K:	.792 g/cm^3
Vapor Pressure @ 311 K:	.314 x 10^5 N/m^2
Heat of Vaporization:	-5.94 kJ/g
Viscosity @ 340 K, 1atm:	135.6 x 10^{-6} g/sec-cm
Enthalpy of Reaction with Air (CH_3OH liquid, H_2O gas):	20.083 kJ/g

b) Coal (Pittsburgh seam)

Chemical Composition, Weight %:	C,	76.72 %
	H,	5.12 %
	N,	1.45 %
	S,	1.16 %
	Ash,	6.05 %
Estimated Size Distribution, wt. % (Milne, Greene & Beachey, 1974):	> 85 μm,	1.3 %
	74 to 85 μm,	.8 %
	43 to 74 μm,	6.6 %
	30 to 43 μm,	5.3 %
	20 to 30 μm,	18.0 %
	10 to 20 μm,	42.0 %
	< 10 μm,	26.0 %
Estimated Enthalpy of Reaction with Air (Babcock & Wilcox, 1963, p 2-8):	31.4 kJ/g	

oil on the sedimentation rate. It was apparent from their work that it would be impossible to keep 10 μm coal particles in suspension for more than a few minutes in a liquid as inviscid as methanol. This suggested that some sort of mechanical stirrer would be required. Another 34 ℓ pressure vessel rotating at about 30 rpm meets this requirement. Ball bearings .5 cm in diameter placed in the rotating vessel aid in the agitation.

The problem of coal build-up has been met with a less satisfactory solution. When burning the slurry, a larger nozzle is used than when burning pure methanol. If the coal builds up in the nozzle, increasing the fuel tank pressure overcomes the decrease in nozzle area. The result is a constant fuel flow rate, but a varying droplet size distribution and fuel jet momentum.

Because the coal would plug the flow measuring orifice, the orifice is by-passed when burning the slurry. Flow rate is then measured by monitoring the nitrogen flow as it enters the pressure vessel and displaces the methanol/coal mixture.

3. Igniter System

The igniter system is used only during start-up. The furnace, when adjusted properly, is self-sustaining. The final stage of the secondary air line contains a venturi mixing section with injection ports. Propane, at a predetermined flow rate, is injected into the mixing section. A spark plug is located just upstream of the burner. As the combustible mixture passes over the spark plug electrodes, a spark discharge ignites the gas. Pure propane is then injected into the primary air stream while the secondary propane is shut off. The liquid fuel can then be truned on and the propane turned off.

4. Burner Assembly

The burner assembly contains a fuel nozzle surrounded by a primary air stream, as is shown in Figure II-3. The secondary air is brought into the burner in an annulus parallel to the primary stream. A conical shaped quarl is attached to the downstream side of the burner.

The design of the fuel nozzle consisted of choosing between two techniques for fuel atomization: a pressure jet nozzle or an air blast atomizer (see Figure II-4). The pressure jet nozzle works by forcing the liquid to swirl rapidly within the nozzle. The swirling liquid is forced through a small orifice at the tip, so that it leaves with a large amount of both angular and translational momentum. The radial forces on the thin column of liquid cause it to spread rapidly into a thin sheet which quickly breaks down into fine droplets. By adjusting the exit orifice diameter, the amount of swirl, and the pressure, one can control the angle of spread and the droplet size distribution. The density and surface tension of the liquid are important parameters in controlling droplet size. Pressure jet nozzles operate around 7×10^5 N/m^2 gauge and the flow rates vary about proportionally to the square root of the pressure drop across them.

The second nozzle design is the blast atomizer. These operate at significantly lower pressures (less than $.7 \times 10^5$ N/m^2 gauge) and use the momentum of an air or steam stream to break up the liquid stream. This type of atomizer cannot be used to meter the fuel since there are no small orifices. It also does not give as uniform a fuel distribution as the pressure jet nozzles. But, because the atomizing air mixes intimately with the fuel, this type of atomizer can produce a more satisfactory flame than the pressure jet nozzle. A discussion on droplet

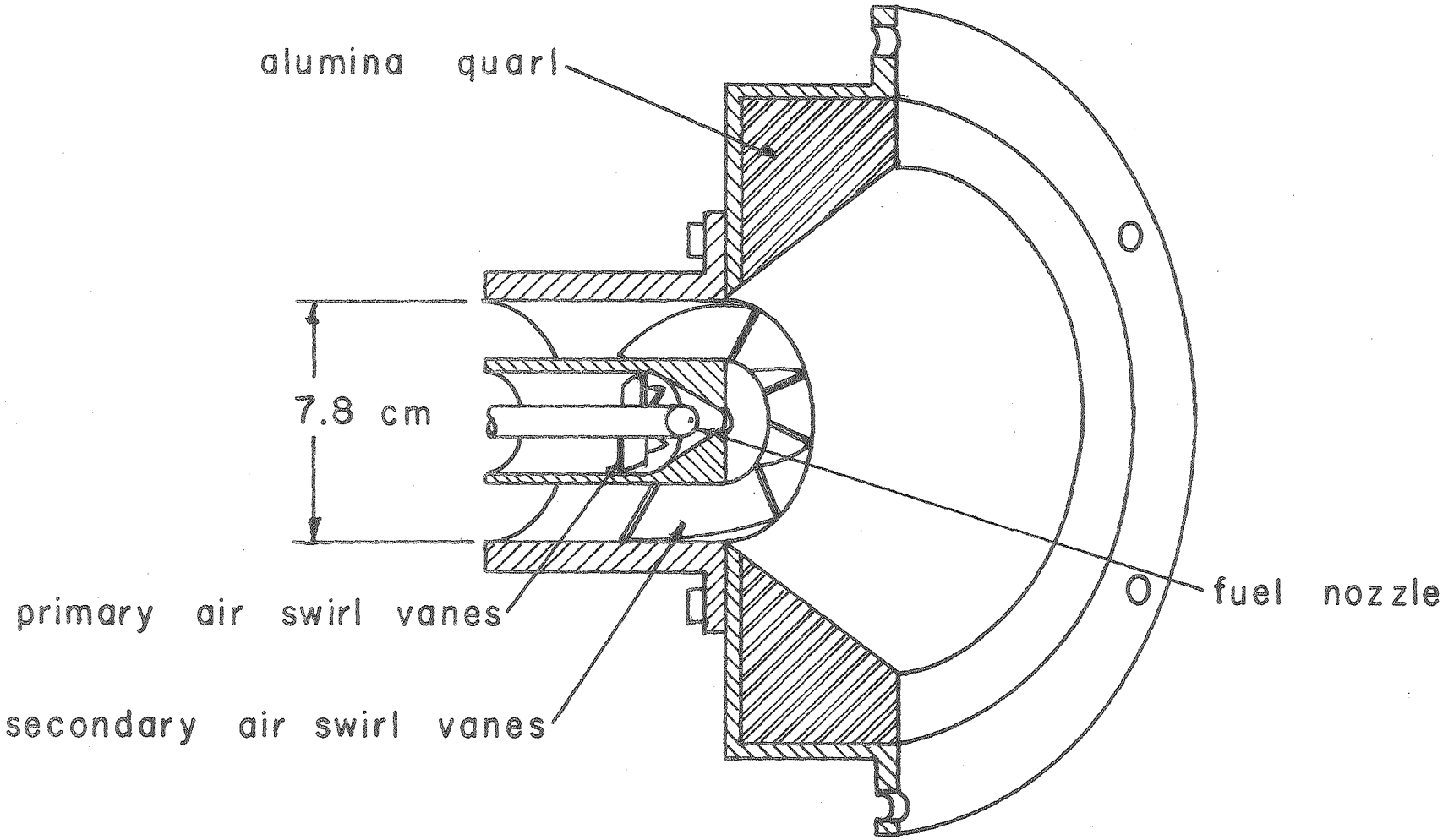

FIGURE II-3.

Burner Assembly for Methanol Furnace

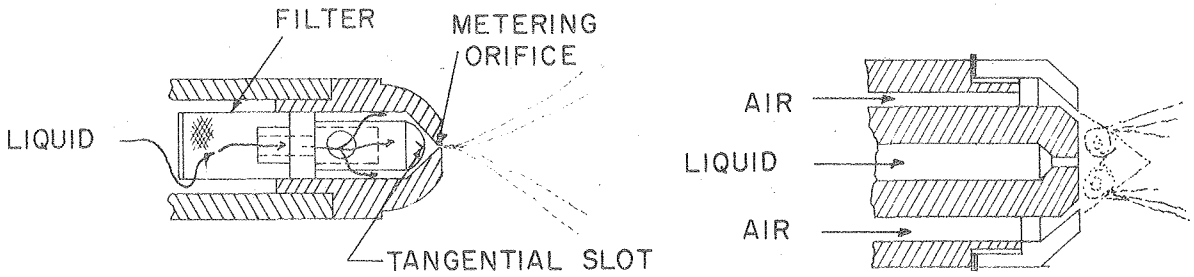

(a) PRESSURE JET NOZZLE (b) AIR BLAST ATOMIZER

FIGURE II-4. Liquid Fuel Atomizers

formation in spray nozzles is given in Beér and Chigier (Chapter 6). More details on nozzle design and performance are given in the reports of the Joint Committee of the International Flame Research Foundation (1953 and 1959).

Because commercially built pressure jet nozzles are inexpensive and available in a wide range of flow rates, this type of fuel atomizer was chosen. Different sizes are interchangable so that flow rates from .5 to 10 g/sec can be obtained with proper droplet size distribution.

To control the momentum of the fuel jet and allow for partial pre-mixing of liquid fuel and air, a primary air annulus surrounds the pressure jet nozzle. This also permits burning of gaseous fuels with the same burner by substituting fuel for the primary air.

The majority of the combustion air comes into the burner as secondary air in a tube concentric to the fuel and primary air flows.

Stability of the burner was increased by installing swirl vanes in the primary and secondary air streams which are shown in Figure II-3. The swirl number, S, is defined as the ratio of jet angular momentum to the product of axial thrust and exit radius. For weak swirl numbers ($S < .6$), stability is increased simply by increasing the effective residence time between the fuel and air jets. For strong swirl ($S > .6$), a recirculation zone occurs because of the negative pressure gradient developed in the flow from the outward moving gases. This zone provides a continuous source of radicals and high temperature which acts as a flame holder. As an approximation to the swirl number of a flow in an annulus passing through a vane type swirl generator, Beér and Chigier (Chapter 5) give

$$S = \frac{2}{3}\left(\frac{1 - (R_h/R)^3}{1 - (R_h/R)^2}\right) \tan \alpha$$

where R_h is the inner hub radius, R is the outer radius, and α is the angle the vane makes with the burner axis. The value of α was chosen to produce strong swirl with the swirl numbers listed in Table II-2.

Flame stability was further enhanced by adding a divergent cone at the exit of the burner. The cone increases the radial distance of separation between peaks of axial and tangential velocites and also increases the mass flow rate in the recirculation zone (Beér and Chigier, Chapter 5). The optimum divergence angle (60°), throat location and swirl were determined from Figure 5.16 of Beér and Chigier (p. 126).

The divergent cone, or quarl, was made of alumina to minimize heat transfer from the recirculation zone.

The parameters used for the design of the burner and the actual operating conditions are given in Table II-2.

TABLE II-3
Burner Design Characteristics

Parameter	Design	Operation
Fuel Flow Rate	.5 to 10 g/sec	3 g/sec
Fuel Pressure	1.7 to 8.5×10^5 N/m^2 gauge	2 and 5.5×10^5 N/m^2 gauge
Fuel Temperature	294 K	294 K
Primary Air Flow Rate	0 to 3.5 g/sec	3 g/sec
Primary Velocity	0 to 42 m/sec	36 m/sec
Primary Swirl Number	0 to .6	3
Primary Pressure	0×10^5 N/m^2 gauge	$.24 \times 10^5$ N/m^2 gauge
Primary Temperature	294 K	294 K
Secondary Air Flow Rate	0 - 100 g/sec	18.4 g/sec
Secondary Velocity	0 - 23 m/sec	4.3 m/sec
Secondary Swirl Number	.6	.6
Secondary Pressure	0 N/m^2 gauge	0 N/m^2 gauge
Secondary Temperature	294 K	294 K

5. Combustion Chamber

The size of the combustion chamber was dictated by the material available and the size of the experimental facility. The diameter is 19.6 cm and the length of the test section is one meter. Based upon the flow rates listed in Table II-2 and an average temperature of 1500 K, the characteristic residence time in the combustion chamber is 250 msec.

The test section is water cooled and made in two halves for ease of assembly. Twelve ports, 5 cm in diameter, are provided along the axis of the furnace to allow optical measurements and probing of the flame.

6. Exhaust System

As with the air delivery system, the exhaust system was constructed for a previous experiment (Pratt, 1968). The only new design required was to adapt the combustion chamber to the exhaust pipe and install a water sprayer to cool the combustion products. The high temperature of the exhaust gases did, in fact, limit the fuel flow. Fuel flows much greater than 3 g/sec resulted in charring of the lagging material around the exhaust pipe flanges.

To control the pressure in the combustion chamber, steam is injected in the exhaust stack. After mixing with the steam, the gases exit through a muffler to reduce noise. As a safety measure, the exhaust system is equipped with an aluminum foil burst disc which ruptures at pressures over about $.03 \times 10^5$ N/m^2 gauge.

III. INSTRUMENTATION OF THE FURNACE

A thorough characterization of the performance of a furnace, requires more than determination of the inlet conditions and the outlet conditions. Heat release and radiation calculations require, as a minimum, a knowledge of the temperature, water, carbon dioxide, carbon monoxide, fuel and oxygen concentrations throughout the furnace. If the pollutant forming characteristics of the furnace are of interest, then, in addition to the above information, one should measure nitric oxide, nitrogen dioxide, formaldehyde, particulates, unburned hydrocarbons, and a multitude of trace pollutants such as hydrogen cyanide and ammonia. The instrumentation of the furnace is designed to measure most of these parameters, if not quantitatively, at least qualitatively, throughout the combustion chamber.

A. Temperature Measurement

Temperature is probably the most important single parameter to be measured in a combustion system. It can be related to the extent of reaction, the turbulence levels, the heat transfer (radiative and convective), and the nitric oxide forming ability of the furnace. Fristrom and Westenberg (1965, Table VIII-1) list different techniques available for measuring temperature in flame systems. More recent developments in optical techniques using lasers to measure Rayleigh scattering (Pitz, et al., 1976) and Raman radiation are encouraging, but they offer no big improvement over the simple thermocouple when it comes to measurements in complex furnace systems.

It is because of versatility, low cost, and ease of measurement that a thermocouple is used in this study. The temperature range within the furnace suggests that a Pt/Pt-13% Rh thermocouple would be most suitable. The maximum recommended temperatures for this type of thermocouple is 1725 K, which is slightly less than the maximum uncorrected temperature recorded in the furnace. The design of the probe follows that of Schefer (1976) and Cernansky (1974) and is shown in Figure III-1. It employs a .0762 mm diameter junction with .254 mm lead wires. The thermocouple emf is referenced to a water/ice bath and is read to the nearest .1 mv on a Honeywell model 2745 potentiometer and a Hewlett-Packard model 7100 B strip-chart recorder.

There are four specific problems encountered when using a thermocouple to measure high temperature in turbulent gases: time response, aerodynamic wakes, catalytic surface reactions, and heat transfer errors. Even though it is recognized that turbulent temperature fluctuations can increase the formation of nitric oxide and the radiation from the flame, time averaged values are measured; so time response is not critical. For the existing system the time response (approximately .1 sec) is limited by the strip-chart recorder and not the thermocouple. The aerodynamic wake is also not considered to be a problem with this system because of its small size compared to the furnace flame.

It is well known that catalytic reactions can occur on a platinum surface, especially in a reducing atmosphere and one with a large radical

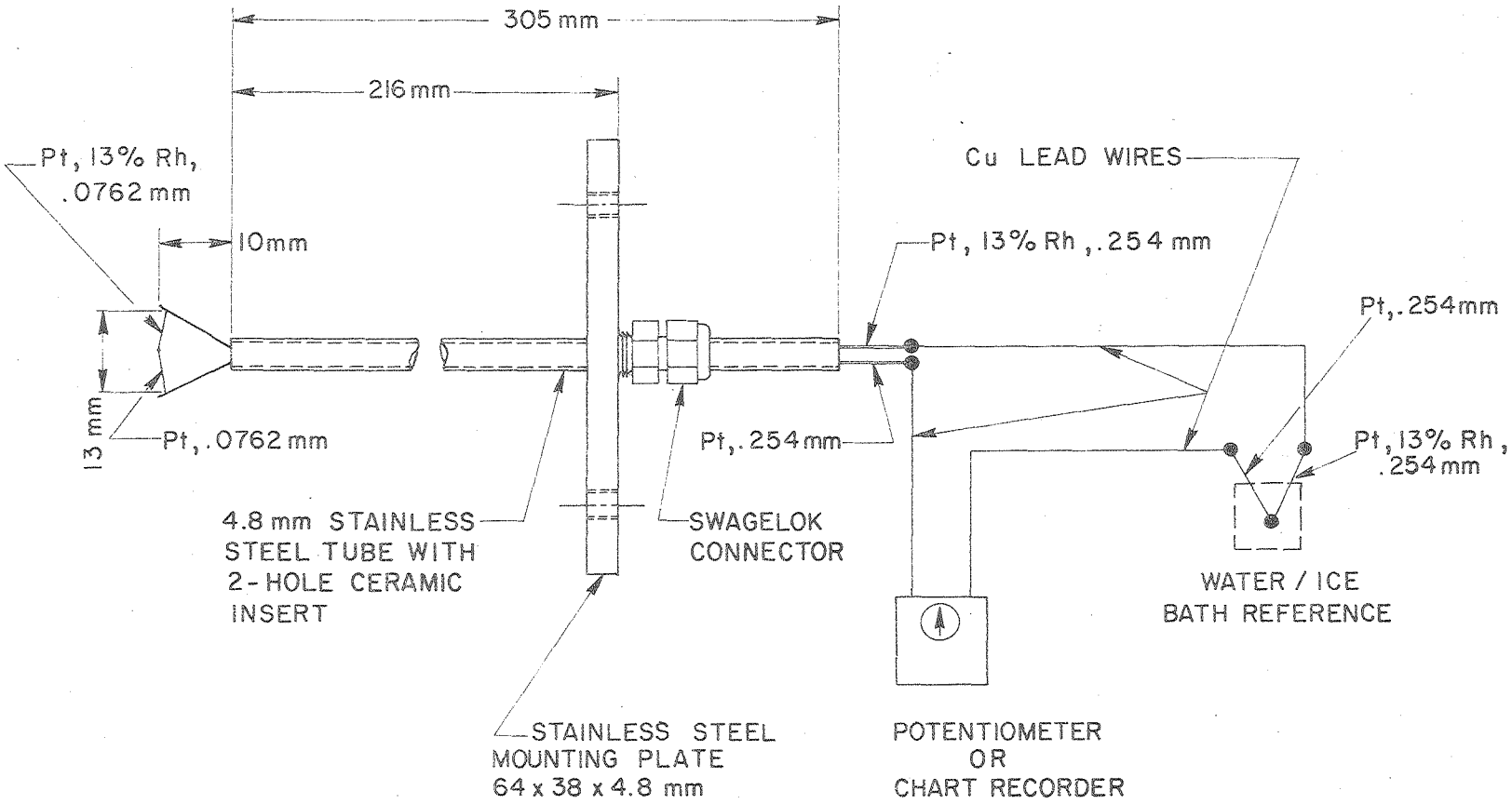

NOTE :
.0762 mm WIRES ARE
COATED TO .102 mm WITH Y_2O_3 + BeO

FIGURE III-1. Thermocouple Probe

concentrations. Until recently, it had been customary to coat the thermocouple junction with silica to reduce catalytic reactions (Kaskan, 1957). But, at temperatures as high as exist in the furnace, it has been found that the silica coating is not as effective as coating as one composed of a combination of yttrium and beryllium oxide (Kent, 1970). This coating and the procedure suggested by Kent that is used on the thermocouple junction.

The last problem associated with high temperature thermocouple measurements, heat transfer errors, is difficult to overcome. Many authors have addressed this problem (Bradley and Matthews, 1968; Fristrom and Westenberg, 1965, Chapter VIII; Herzfeld, 1961). The voltage measured from a thermocouple indicates the true temperature of the thermocouple junction, not the gas surrounding the junction. It is an equilibrium temperature reached by an energy balance involving conductive, convective, and radiative heat transfer as shown in the following equation:

$$q_{conduction} + q_{convection} + q_{radiation} = 0$$

where the energy conducted into the junction along the wire of diameter d, length ℓ, and thermal conductivity k is:

$$q_{conduction} = k\pi d\ell \frac{dT_j}{dx}$$

The convection and radiation terms are:

$$q_{convection} = h\pi d\ell \, (T_g - T_j)$$

$$q_{radiation} = -\pi d\ell\varepsilon_j \, \sigma \left(T_j^4 - T_w^4 \, \beta - T_\infty^4 \, (1-\beta)\right)$$

with h equal to the convection coefficient of the wire, at temperature T_j, to the gas immediately surrounding the wire, at T_g. T_w is the wall temperature, ε_j the emissivity of the junction, T_∞ some average temperature representative of the gas between the junction and the wall, and β a

parameter which is a measure of the transmissivity of the gas.

For a furnace with little particulate radiation and a reasonably small optical depth, β approaches one and the radiation term approaches the conventional form

$$q_{radiation} = \pi d \, \ell \, \varepsilon_j \, \sigma \, (T_j^4 - T_w^4)$$

Even when the coal/methanol slurry is burned, the optical depth is small, so setting β to one is reasonable; but for a flame with a significant optical depth, β becomes smaller and, in the limit, approaches zero. This means that the thermocouple will be exchanging radiant energy with the gas and not the wall. If the gas at a distance from the junction is hotter than that near the junction, it is possible to have a net flux into the thermocouple due to radiation even when the walls are cold.

The energy conducted away from the junction is directly proportional to the temperature gradient along the wire. The junction is positioned perpendicular to both the furnace axis and radius; maximum temperature gradients in this direction do not exceed 2000 K/m. With a wire diameter of 7.62×10^{-5} m and a thermal conductivity for platinum of 73 W/mK, the maximum conducted energy rate is .00066 W. This is well over an order of magnitude less than the energy rate for other modes, and so conduction will not be considered further.

An expression for the convection coefficient of a gas flowing perpendicularly to a cylinder is given by Holman (1972, p. 186) as

$$\frac{hd}{k} = .989 \left(\frac{U\,d}{\nu}\right)^{1/3} Pr^{1/3}$$

where U is the free stream gas velocity around the thermocouple, ν and k are kinematic viscosity and thermal conductivity of the gas, and Pr is the Prandtl number.

With these definitions and approximations, the energy equation becomes,

$$.989 \, \frac{k}{d} \left(\frac{U\,d}{\nu}\right)^{1/3} Pr^{1/3} \, (T_g - T_j) - \varepsilon_j \, \sigma (T_j^4 - T_w^4) = 0$$

In theory, the gas properties and emissivity are known and the wall temperature and gas velocity can either be measured or estimated, so the true gas temperature, T_g, can be determined by measuring the junction temperature, T_j.

$$T_g = T_j + \frac{\varepsilon_j \sigma (T_j^4 - T_w^4)}{.989\ k} \left(\frac{\nu d^2}{uPr}\right)^{1/3}$$

From the above equation, it is apparent that one parameter the probe designer has complete control over is the diameter of the wire. As the diameter decreases, the temperature correction decreases by the 2/3 power. It is for this reason that the smallest wire that will remain sound under measuring conditions is the most desirable.

Estimating the emissivity of the thermocouple junction is not always straight forward. For unoxidized platinum, the Handbook of Chemistry and Physics (CRC, 1972) gives the total emissivity as .152 at 1273 K and .191 at 1773 K. In the same reference, the emissivities for beryllium oxide and yttrium oxide are, respectively, .07 to .37 and .60. The value used by Kent and Bilger (1973) for a platinum wire coated with Y_2O_3 and BeO is .72. To check the emissivity of the existing thermocouple, a second uncoated thermocouple made from .0762 mm platinum wire was made. Both the coated and uncoated thermocouples were inserted into a hydrogen/oxygen/argon flame in a flat flame burner and the temperatures recorded as a function of height above the burner. The results are shown in Figure III-2.

The energy equation should be modified to allow for catalytic heating.

$$h\ (T_g - T_j) - \varepsilon_j \sigma (T_j^4 - T_w^4) + q_{cat} = 0$$

where the heat flux due to catalysis is a positive quantity for exothermic recombination reactions, and is a function of temperature and radical concentration.

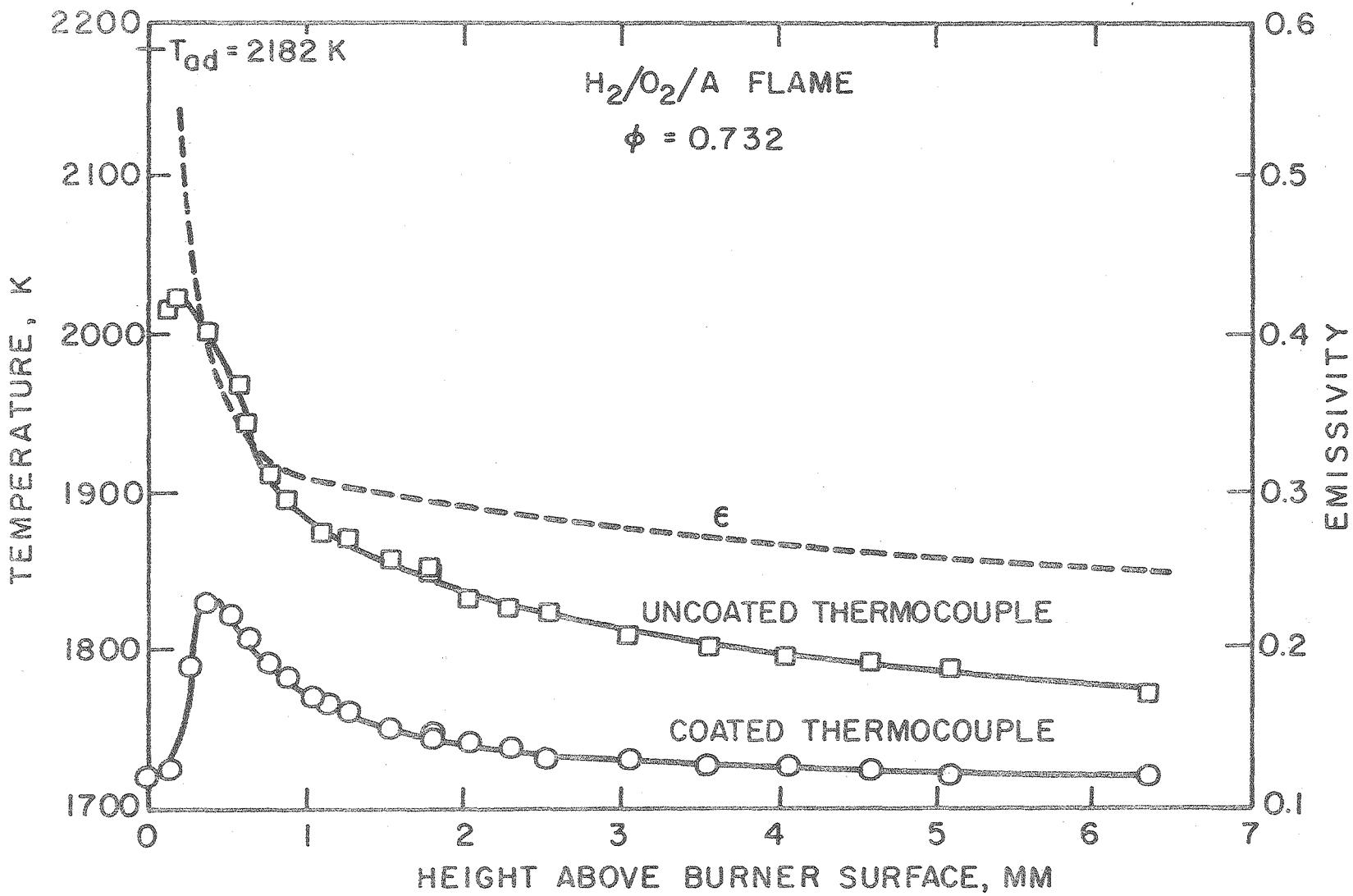

FIGURE III-2. Temperatures and Calculated Emissivity for Pt/Pt-13% Rh Thermocouple

An energy equation can be written for each of the two thermocouples; and, since T_g is the same in each equation, the emissivity of the coated thermocouple can be found in terms of the emissivity of the uncoated thermocouple.

$$\varepsilon_j = \varepsilon_j' \left[\frac{h}{h'} \frac{(T_j'^4 - T_w^4)}{(T_j^4 - T_w^4)} \right] + \frac{(h/h')(T_j' - T_j) + q_{cat} - (h/h')\, q'_{cat}}{\sigma\,(T_j^4 - T_w^4)}$$

The prime indicates the uncoated thermocouple. The difference in h and h' is due only to the difference in diameter between the uncoated wire (.0762 mm) and the coated wire (.1016 mm). The ratio of h to h' equals $(d'/d)^{2/3}$, .825. It is impossible to predict the values of q_{cat} and q'_{cat}, but if these terms are set to zero, a maximum value for ε_j can be determined since $(q_{cat} - h/h'\, q'_{cat})$ is a negative quantity.

Figure III-2 shows the results for $\varepsilon_j' = .191$. Early in the flame, the effect of catalysis can easily be seen. This is expected since the radical concentrations and temperatures are highest there. As the combustion products reach equilibrium, the catalytic effect diminishes and the plotted emissivity approaches the true emissivity. A value of .25 appears to be a good estimate for the true emissivity.

The large discrepancy between the emissivity estimate of this study and that of Kent and Bilger (1973) cannot be completely reconciled. If the coating on the wire had voids, then it is possible that the predicted emissivity would be somewhat lower than that of Kent and Bilger. However, the emissivity values of pure BeO, Y_2O_3, and platinum suggest that a value of .72 is too large.

B. Chemical Composition Measurement

The gas sampling system consists of a probe, a sample transfer section and an analysis section. Each of these three sections is tailored to the individual species being measured (CO_2, H_2O, CO, CH_3OH, HCHO, O_2, NO, or NX), and their design will now be discussed.

1. Sampling probes

A properly designed probe will extract a truly representative sample from the furnace without seriously perturbing the flow field of the furnace at the position under study. To keep the sample representative, the chemical reactions must be quickly quenched by reducing their pressure, temperature, or both. For stable species like CO_2, CO, H_2O, O_2, and CH_3OH, this can be done successfully with a probe which drops the pressure in the sample through a sonic orifice. For highly reactive radicals, for example, OH, O, H and CH_3, there is no hope of extracting a representative sample with this conventional type of probe since reaction times are much shorter than the characteristic residence time within the probe (Schefer, 1976, Appendix B). For species of questionable stability (NO, NO_2 HCHO) nothing as definitive can be stated. Schefer, Matthews, Cernansky, and Sawyer (1973) have looked specifically at the problems of probe design on the measurements of NO and NO_2 in combustion systems and have found a difference in results between stainless steel and quartz probes and whether they are cooled or uncooled. Formaldehyde (HCHO) is troublesome because it is easily oxidized, so anything which will reduce the temperature, pressure or catalytic activity of the probe walls will increase the reliability of its measurement.

The flow field in the furnace can be disturbed by the physical presence of the probe. This effect can be reduced by keeping the diameter

of the probe to a minimum and by locating it such that it is parallel to and pointing upstream towards the furnace flow. The fact that the probe is acting as a mass sink within the furnace additionally alters the flow field. The extent of this effect can be calculated (Fristrom and Westenberg, 1965, p. 190). In this study, the mass flow in the probe is less than .02% of the total furnace flow and the probe diameter to furnace diameter ratio is .015. Therefore, the disturbances within the flow field due to the probe are considered to have a negligible effect on the position of the time averaged concentration measurements.

With the above facts in mind, a partially cooled quartz probe has been built following the designs of Schefer (1976, Chapter 2 and Appendix B) and Fristrom and Westenberg (1975, Chapter IX). A diagram is shown in Figure III-3.

To position accurately the probe ($\pm$ 1/2 mm), a traverse mechanism was built that can be bolted to any of the twelve ports along the axis of the furnace. a photograph of the quartz probe in position on the traverse mechanism is shown in Figure III-4.

2. Sample analyzers

Table III-1 lists the analyzers used for the various combustion products.

TABLE III-1. ANALYSIS EQUIPMENT FOR MEASURING CHEMICAL SPECIES

Analyzer	Detector	Species
Beckman Model 315	infrared absorption, CO_2 specific	CO_2
Beckman Model 315A	infrared absorption, CO specific	CO
Hewlett-Packard Research Chromatograph Model 5750	dual flame ionization	CO, CO_2 HCHO, CH_3OH
	thermal conductivity	H_2O, $N_2 + O_2$
NO/NX analyzer (local design)	chemiluminescent	NO, NX

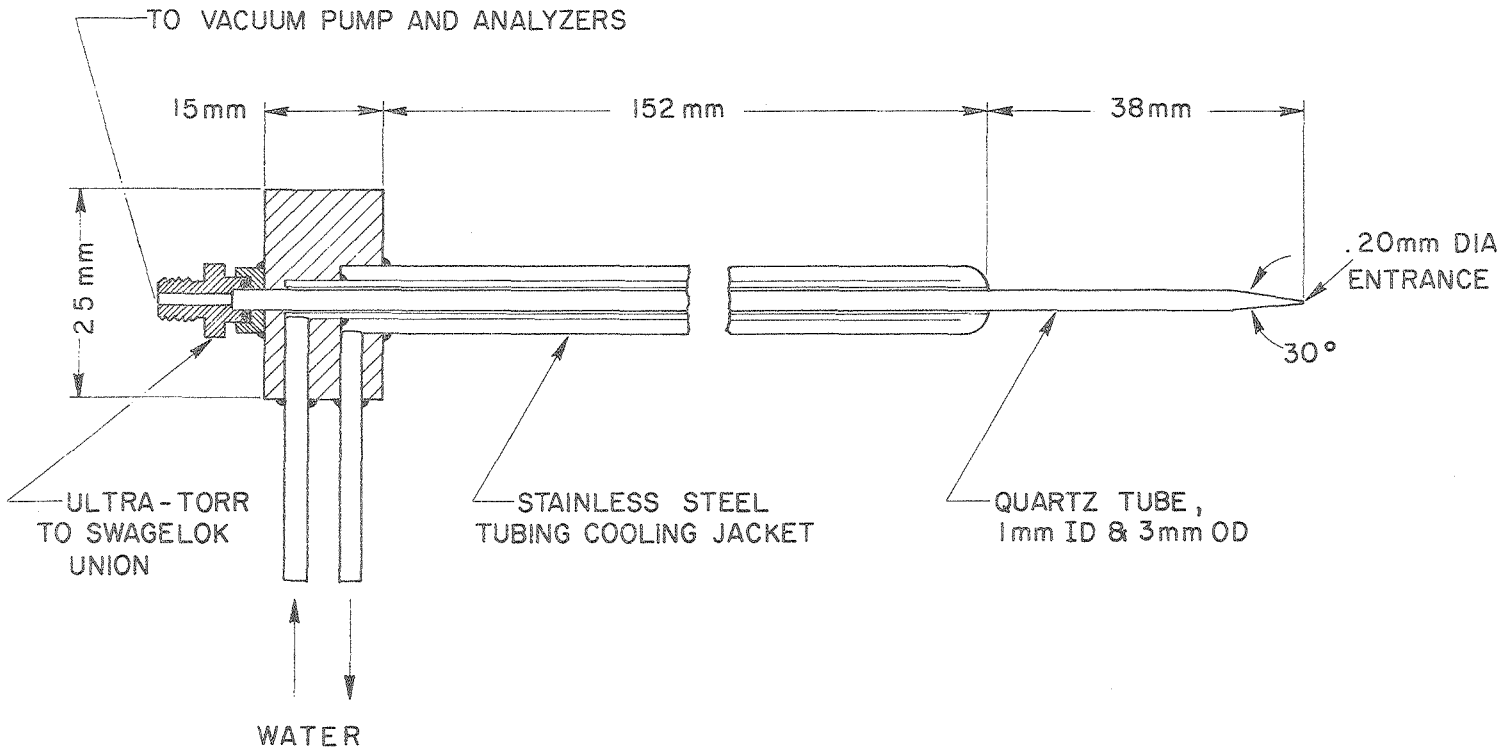

FIGURE III-3. Gas Sampling Probe

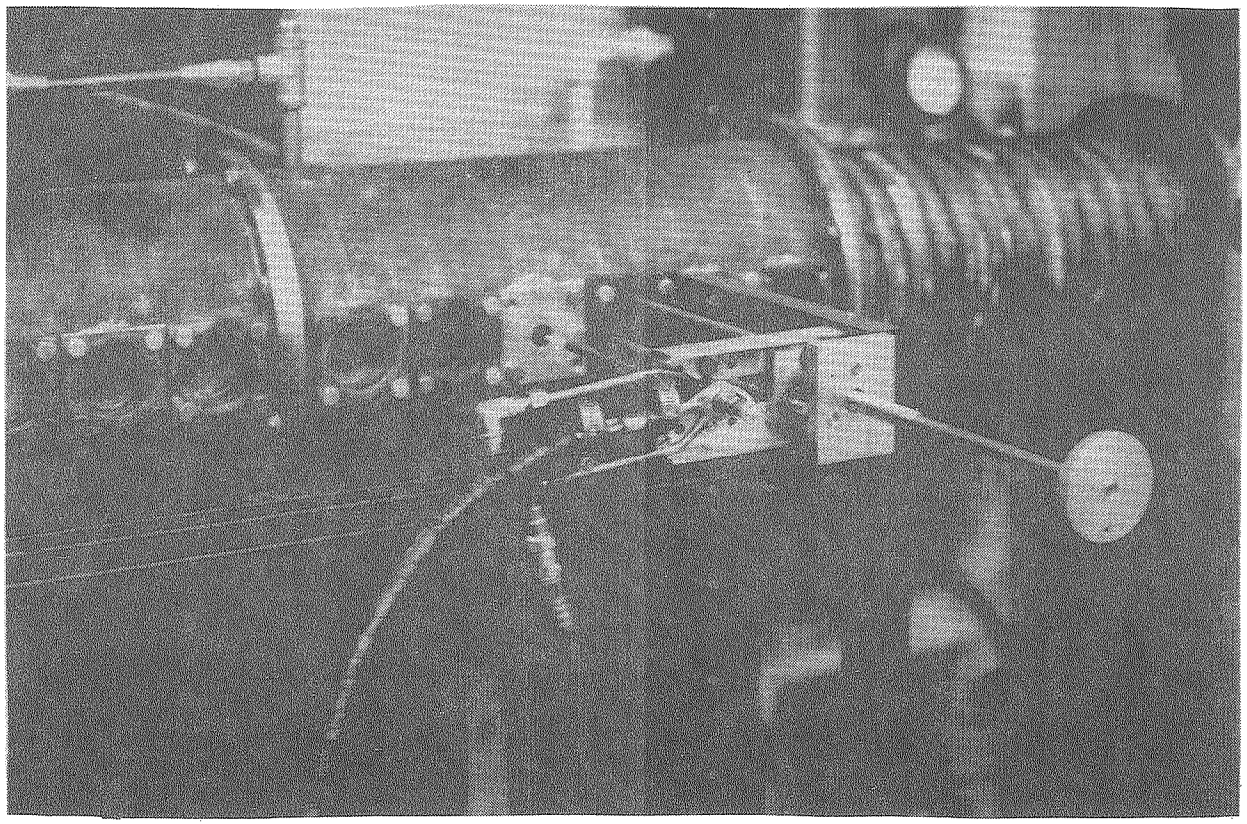

FIGURE III-4. Quartz Sample Probe Mounted on Traverse Mechanism

a. Beckman Infrared Analyzers

The Beckman infrared analyzers require the continuous flow of an atmospheric pressure sample through the sample chamber. Calibration curves are provided with each instrument to correlate the strength of the signal with partial pressure of CO or CO_2. Both the zero point and an upscale concentration are checked before data is taken. The carbon dioxide analyzer operates in the range of partial pressures from 0 to .15 atm with an accuracy of about 1% of full scale. The carbon monoxide analyzer operates in any of three following ranges with an accuracy of 1% of full scale: 0 to 500 x 10^{-6} atm, 0 to .03 atm, and 0 to .10 atm.

To reduce the possibility of interference, water is condensed out before passing through the sample tube. Some small interference also exists between CO and CO_2, but this can be accounted for if both species are measured.

b. Gas Chromatograph

The major components of the 5750 gas chromatograph are shown in Figure III-5. Briefly, the sample is injected into the carrier gas stream with the sampling valve. The carrier gas transports the sample through the column where it is separated. As each species elutes from the column, it is detected with the thermal conductivity of flame ionization detector. The detector signal is amplified and fed into an integrator and strip chart recorder. The integrator calculates the area under the eluting peaks, which can then be related to species concentration.

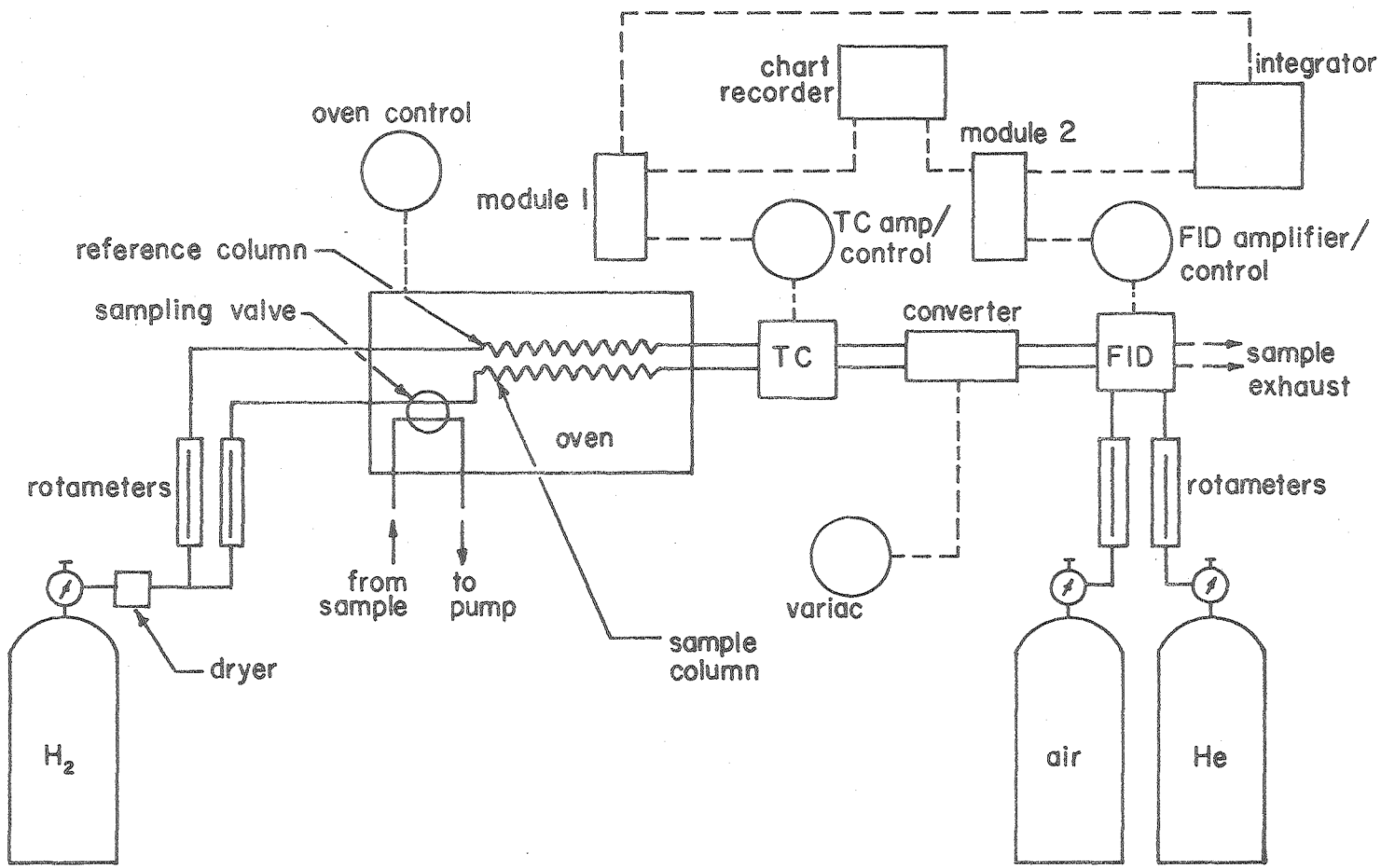

FIGURE III-5. Elements of the Gas Chromatographic System

To take advantage of the high sensitivity of the FID, Colket, Naegeli, Dryer and Glassman (1974) have devised a catalyst which hydrogenates carbon containing compounds to their homologous alkanes. This permits detection of CO, CO_2 and HCHO with an FID when normally there would be no signal, and causes the response of CH_3OH to increase to that of CH_4. The catalyst consists of ruthenium coated glass beads packed in a copper tube heated to 550 K and is located between the TC detector and the FID as shown in Figure III-5. Details of catalyst construction and performance are given in the original paper (Colket, et al., 1974).

To fully realize the potential of the gas chromatograph, a sophisticated integrator is necessary. The one shown in Figure III-5 is an Autolab System IV with two channel modules. This equipment allows detection of peaks which would normally go unnoticed, and is able to resolve, in a systematic manner, two or more peaks which appear hopelessly fused. The operation manual by Spectra Physics gives a complete description of system capabilities.

The chromatograph operating conditions used for this present study and a typical chromatogram are shown in Table III-2 and Figure III-6, respectively.

c. Chemiluminescent Analyzer

The analyzer used for measuring nitric oxide was built by previous workers (Patterson, McElroy, Sawyer and Singh, 1970) and is shown in Figure III-7. It operates on the principle that NO reacts with ozone, O_3, to produce NO_2 in an electronically excited state. Chemiluminescence occurs when the NO_2 relaxes to its ground state. The primary reaction sequence is

TABLE III-2. OPERATING CONDITIONS OF GAS CHROMATOGRAPH

Column: Porapak T, 80/100 mesh, 1.83 m long, 3.18 mm diameter aluminum tubing.

Carrier: Hydrogen, 3.16×10^5 N/m^2 gauge, 1.25 cm on flow meter.

Thermal Conductivity Detector: 196 ma bridge current, polarity A, 150° C.

Flame Ionization Detector: Electrometer on dual operation and 10^2 scale, air flow is 440 ml/min at 2×10^5 N/m^2 gauge, helium make-up is 55 ml/min at 3.44 N/m^2 gauge, 150° C.

Temperatures: Injection port at 150° C, sample loop at 110° C, ruthenium converter at 270° C; column oven programmed to start at 80° C, hold for 1 min, increase at 20° C/min to 120° C, hold 20 minutes.

Sample: 1/2 cm^3 loop, 70° C, $.067 \times 10^5$ N/m^2 gauge.

Integrator:

	Channel 1	Channel 2
Detector	FID	TC
Peak Width	20 sec	4 sec
Slope Sensitivity	500/200/500	100
T1	10 sec	5 sec
T2	0	80 sec
T3	0	0
Minimum Area	0	0
Spike Trap	off	off
Tailing Peak	30	30
Base Line	5	5

Recorder: .5 in/min, 1 mv scale.

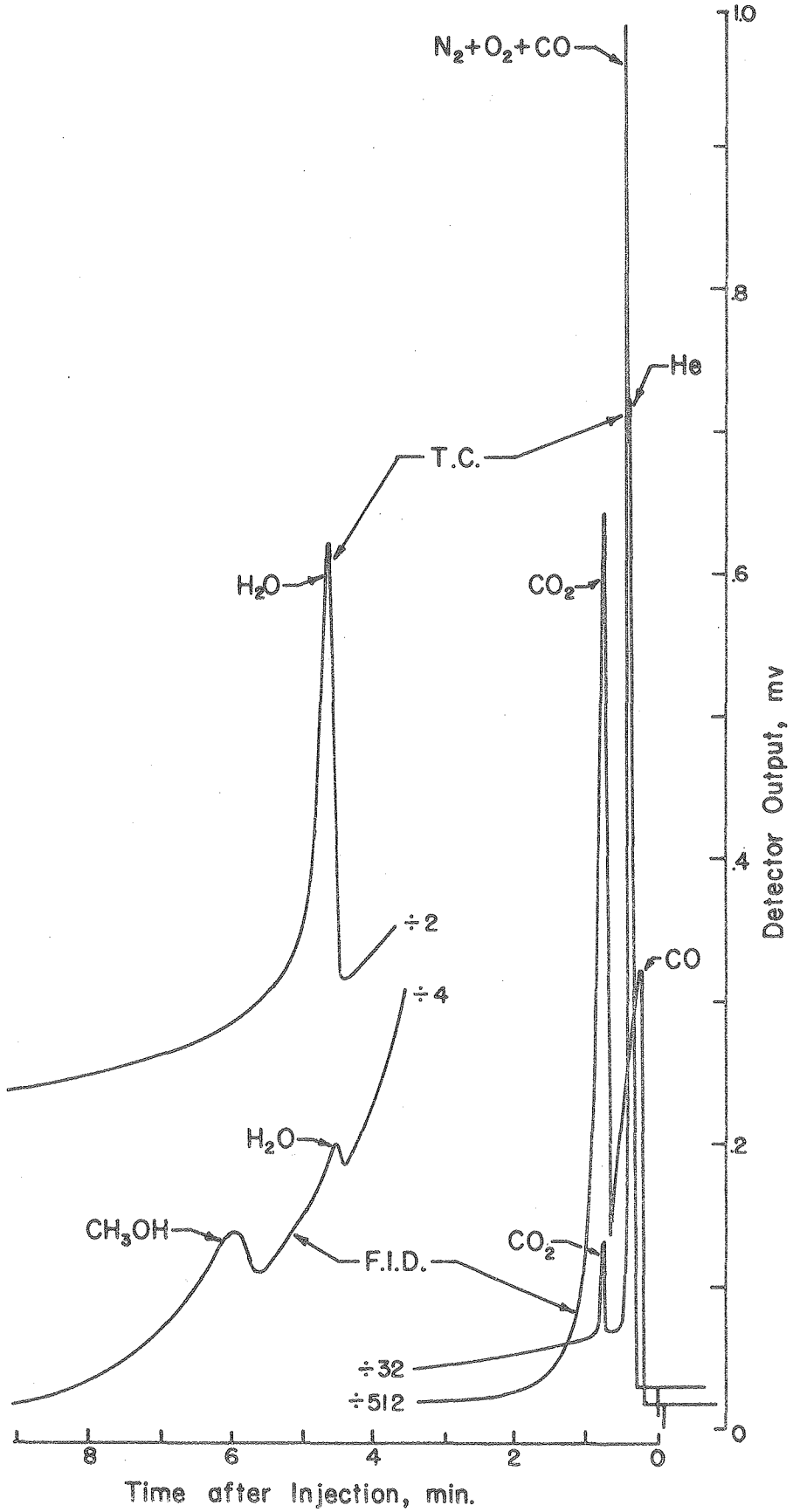

FIGURE III-6. Chromatogram of Sample Taken From Methanol Furnace. (Operating conditions are as shown in Table III-2.)

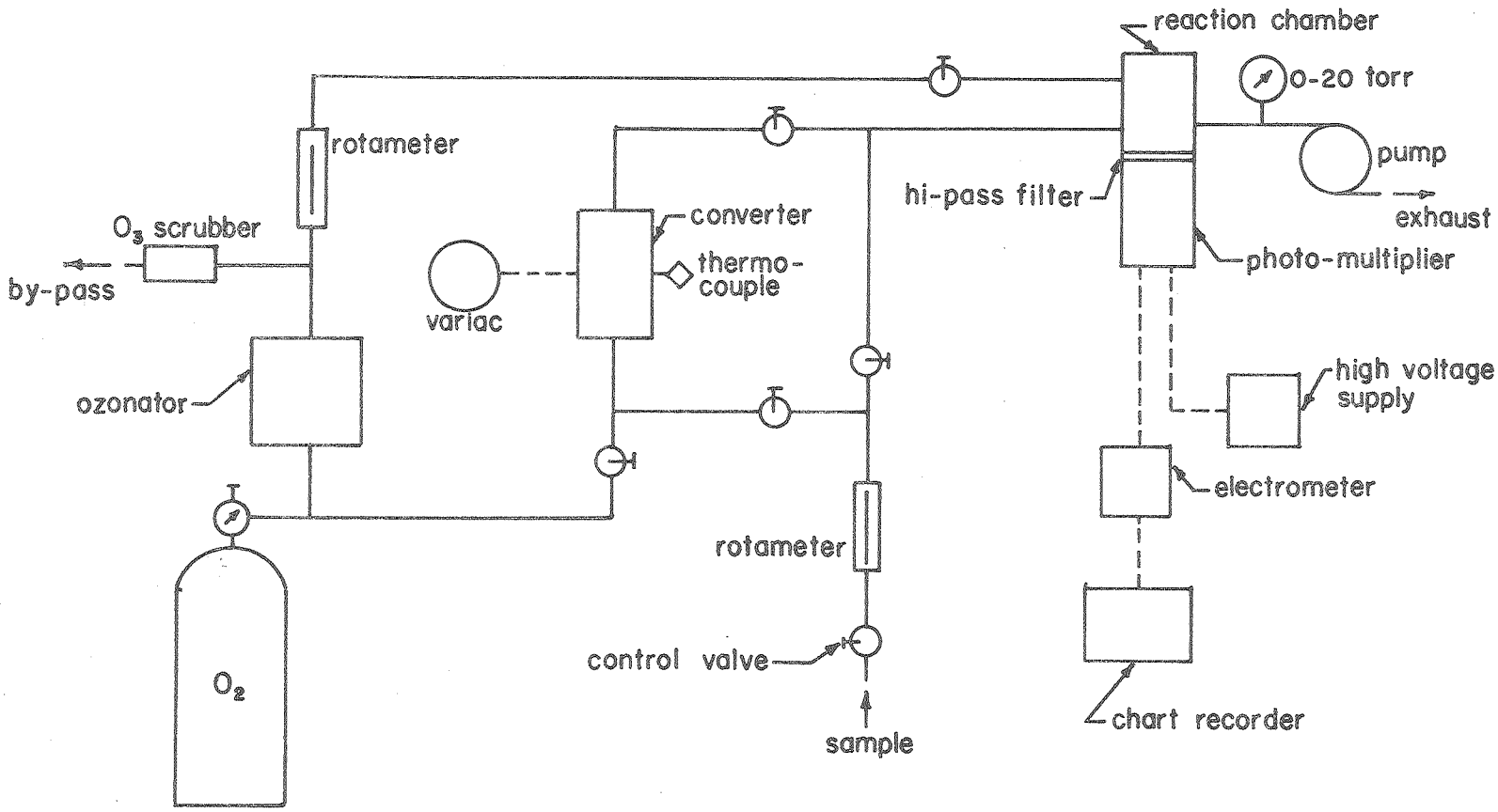

FIGURE III-7. Components of Chemiluminescent Analyzer

$$NO + O_3 \rightarrow NO_2^* + O_2$$
$$NO + O_3 \rightarrow NO_2 + O_2$$
$$NO_2^* \rightarrow NO_2 + h\nu$$
$$NO_2^* + M \rightarrow NO_2 + M$$

The fourth reaction is in competition with the radiation emitting step, so the reaction chamber pressure is minimized to reduce the collisional de-excitation.

The radiation which is emitted is sensed by a photomultiplier tube. Because the current in the tube is small, an electrometer is required to enhance the signal. The signal from the electrometer is recorded on a strip chart, and the ozone is supplied by an electic arc ozone generator.

In addition to NO, other nitrogen containing compounds are of interest because of their importance to air pollution; specifically NO_2, NH_3 and HCN. This group of compounds plus NO will be collectively called NX throughout this report. If these compounds can be converted to NO, then they too can be detected with the chemiluminescent analyzer. Such a converter has been investigated by Zolner (1972) and by Matthews, Smith, Brown and Sawyer (1975). To insure proper conversion even in the fuel rich zones of the furnace, pure oxygen is injected into the sample just before the converter. The converter temperature and other operating conditions are listed in Table III-3.

If the operating conditions are held constant, the output of the analyzer is directly proportional to the NO concentration and has a sensitivity of the order of 1 ppm. An interference problem does exist, though, if the sample gas contains a significantly different make-up than the calibration gas. Normally, calibration takes place with a small amount of NO in N_2. Combustion gases will contain widely varying

TABLE III-3. CHEMILUMINESCENT ANALYZER OPERATING CONDITIONS

Ozonater: .015 SCFM, 7.6 psig, 100 V, 2 cm (glass ball) on ozone flow meter.

Photomultiplier: 1400 V input, 1×10^{-6} a on electrometer output.

Stainless Steel Converter: 700° C, O_2 injection on.

Chamber Pressure:

Conditions	Torr
All flows off	.20
O_3 flow on	.65
O_3 and NO sample flow (5.0 cm)	1.50
O_3 and O_2 injection	1.80
O_3, O_2 injection and NX sample flow (1.15 cm)	2.60

concentrations of CO, CO_2, O_2 and H_2O in addition to N_2. Each of these has its own characteristic quenching rate when reacting with NO_2^*. Earlier workers (Allen, Billingsly and Shaw, 1974; Schefer, 1976) have found that, for example, a mixture containing 10% CO_2 will give an NO reading about 5% below the true concentration while 10% H_2O in the mixture will indicate a 15% low value of NO concentration. If the CO_2 and H_2O concentrations are known, then corrections can be made to the NO level measurements.

3. Sample Transferring Sections

The link between the probe and the analyzer is the sample transferring section. Some of the analysis requires a continuous transfer system and some a batch transfer system. The simplest system is a continuous one in use with the NO/NX composition measurements. It consists of a heated 3/16 inch teflon line connected to a particulate filter and pumped down with a vacuum pump to around .10 atm. The sample is extracted from this line with a tee conection, flow adjusting valve, and an unheated 1/8 inch teflon line pulled down to less than .004 atm by the chemiluminescent analyzer pump. The total distance along the line from the probe to the analyzer is about 5 m. The block diagram of this and the other sampling systems is shown in Figure III-8.

The transfer system for the infrared analyzers is also continuous. After being filtered, the gases pass through a heated teflon line to a single stage, dry ice cooled water trap. The pumps in the Beckman analyzers are insufficient to lower the line pressure below 3/4 atm so an additional bellows pump is used in series to keep line pressure around 1/2 atm. With the water removed, the line between the water trap and the analyzer does not need to be heated.

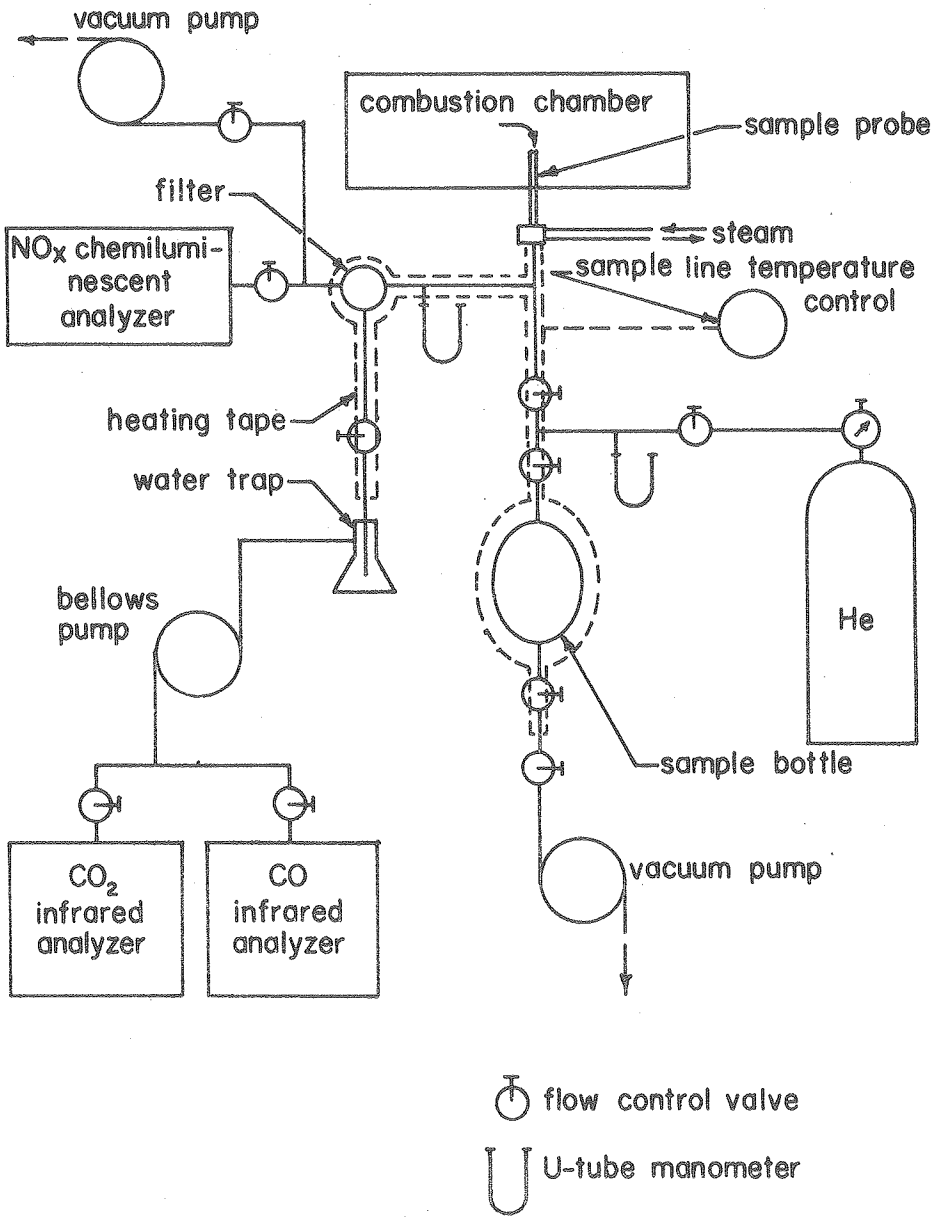

FIGURE III-8. Schematic of Sample Transfer Systems

The gas chromatograph is not located next to the furnace. This necessitates a batch sample technique. As shown in Figure III-8, the sample is pumped directly through a pyrex .25 ℓ sample bottle. The bottle and inlet line are heated to prevent condensation and are maintained at .10 atm. When the sample line and bottle have been sufficiently purged and replenished with a new sample (about 2 minutes), the outer valves on the bottle inlet and outlet are closed. Helium is added to the bottle until a pressure of .4 atm is obtained. The purpose of this is to decrease bottle leakage problems, and to provide enough sample for at least three chromatograms per sample bottle. The inner sample bottle stop-cocks can then be closed and the bottle transported to the gas chromatograph.

The procedure to inject a sample follows. With the bottle connected to the inlet of the gas chromatograph sampling valve (see Figure III-5) and the bottle stop-cocks closed, the sample valve is evacuated. Mercury, gravity fed, is allowed to flow into the other end of the sample bottle (heated to above the dew point) as this stop-cock is opened. When the pressure in the bottle reaches atmospheric, the mercury flow is halted. The sample line pump valve is then shut off right before the sample bottle outlet stop-cock is opened, allowing sample at 1 atm to enter the sampling valve. The sampling valve is then turned to put the sample into the carrier gas stream, and the separation begins.

C. Particulate Measurement

The problems involved with sampling particulates from the furnace are different from those of sampling gases. To minimize the effect on the particle paths, it is desirable to sample isokinetically. This is accomplished by adusting the flow rate in the probe until it matches the free stream velocity. As explained by Pagni (1973), too high of a

probe velocity will cause the stream lines to be deflected towards the probe center-line. The larger particles will not follow the streamlines as well as the smaller particles, thus biasing the sample size distribution towards the smaller diameters. If the probe flow is too slow, the streamlines are bent away from the probe centerline. The larger particles, again, do not follow the streamlines as well; but this time, their inertia is large enough to carry them into the probe resulting in a size distribution biased towards the larger diameters.

Figure III-9 shows the particulate sample probe as designed. The large bend in the probe, although undesirable because of impaction problems, is necessary because it is important to have the probe pointing as close to the upstream direction as possible. For typical flow conditions, it can be shown that this size of a bend will cause particles less than 12 μm in diameter to drift less than 1/10 the diameter of the probe tube. The probe is steam cooled to reduce further particulate oxidation while still preventing condensation of water and methanol. The diameter of the tip is changeable to permit isokinetic sampling under different furnace conditions.

For the particulate sampling system, a filter holder is attached directly to the probe as is shown in Figure III-9. The particulates are collected on a 4.76 cm Nucleopore filter with 1 μm holes. The filter captures the particles partly by impaction and partly with static charge build-up. A bellows pump pulls the flow through the filter and a water trap. Total flow is measured with a wet test meter, and time of flow with a stop-watch.

The filter papers are kept in a desciator both before and after collection of the particulates to remove residual water. An electronic

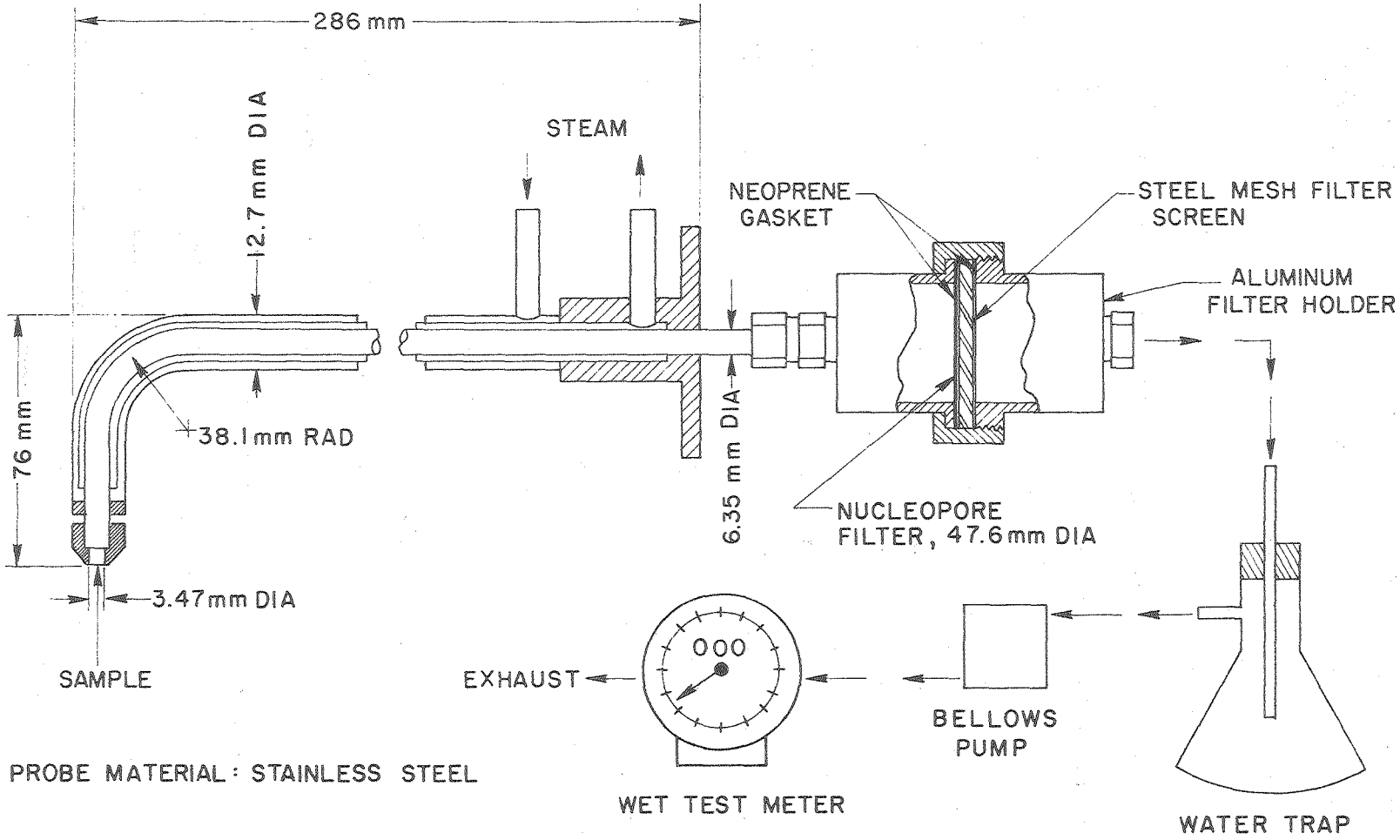

FIGURE III-9. Particulate Probe and Collection System

scale capable of 1 μg accuracy is used to measure tare and loaded weights. The total flow through the filters is varied so that between 1 and 10 μg of particulates will be collected. Tare weight of the Nucleopore filters is about 20 mg.

D. Radiation Measurement

The infrared radiation from the furnace is measured with a Perkin-Elmer model 98 single pass prism monochromator. A schematic in Figure III-10 shows the monochromator and associated equipment. The major components are the source (the furnace flame or a black-body furnace), external focusing table, monochromator, preamplifier, amplifier, and strip-chart recorder.

The external focusing table focuses the radiation emitted by the source onto the entrance slit of the monochromator. Radiation enters through two infrared transparent high temperature windows, passes through collimating aperatures, and strikes plane, front surfaced, aluminized mirrors (M1a and M1b). If a measurement is to be made at tube 2, plane mirror M1c is put in place; for tube 1 measurements, M1c is removed. The radiation reflects off of M1a, is redirected and partially focused by spherical mirror M2, reflected off of plane mirror M3, and is completely focused on the entrance slit, S1, by spherical mirror M4. The chopper motor is used to mechanically interupt the beam 13 times per second.

Inside the monochromator, the radiation is collimated by a two-dimensional parabolic mirror, M5. The parallel light is directed toward a sodium chloride 60° prism, through which it passes and is refracted. It is bounced off a Littrow mount mirror, M6, and immediately passes back through the prism for increased dispersion. The collimating

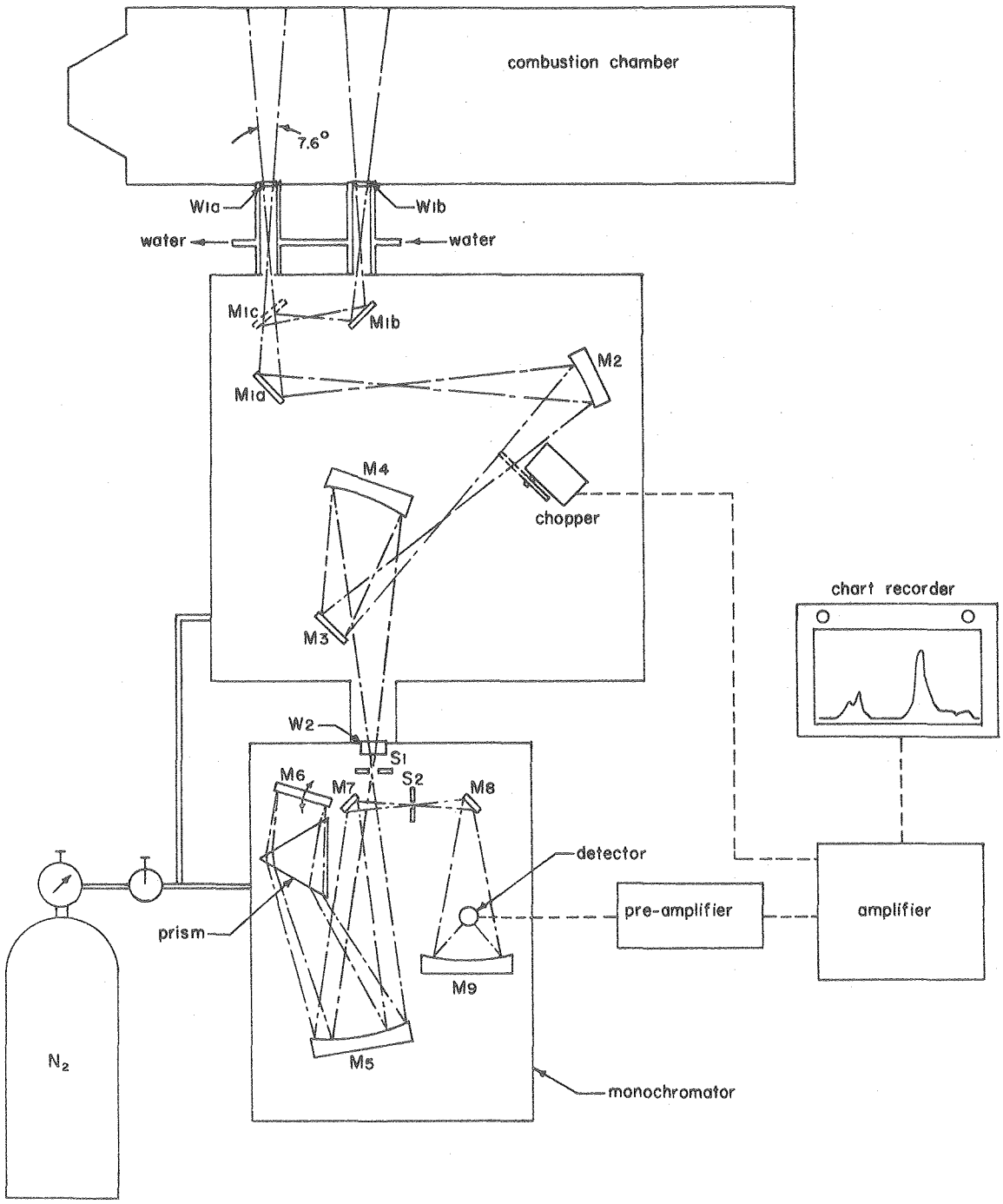

FIGURE III-10. Radiation Measurement Equipment

mirror is now used to focus the dispersed radiation on the exit slit, S2, after it is reflected off of plane mirror M7. Finally, the wavelength interval which emerges from S2 is focused on the detector by plane mirror M8 and ellipsoid mirror M9. Different wavelength intervals can be detected by rotating an indexed wheel which drives the Littrow mirror, thereby focusing a different portion of the spectrum on the exit slit. The index wheel is rotated at a constant speed by a synchronous gear motor.

The detector is a high response thermocouple attached to a blackened gold leaf target, .2 by 2 mm, all in an evacuated chamber with a potassium bromide window. Seventy-five percent of DC response is obtained at 13 Hz modulation.

The electical signal leaving the detector is a 13 Hz signal due to the source intensity plus a low level DC signal due to noise and spurious radiation which has not passed through the chopper. The preamplifier is phase sensitive and only amplifies the 13 Hz source signal. A standard amplifier increases the signal from the preamplifier so that it can be fed to a strip-chart recorder.

Because of the multitude of reflecting and absorbing media through which the radiation beam must pass, it is incorrect to interpret the signal from the detector as an absolute measure of intensity. A source of known intensity is required to calibrate response as a function of wavelength. This is accomplished using an Infrared Industries model 463 blackbody radiation source equipped with temperature controller model 101B. The blackbody is placed directly in front of either tube 1 or tube 2 so that the radiation paths are identical during the calibration and the experiment.

If any of the mirrors internal to the monochromator, the prism, or the detector are moved, it is necessary to recalibrate the Littrow mirror

index wheel against known wavelength sources. This is done by placing a thin film of polystrene in front of the blackbody source. Figure III-11 shows the output of the monochromator during calibration. Additional calibration information is provided in Grosshandler (1976).

The operating conditions of the monochromator and peripheral equipment are listed in Table III-4.

TABLE III-4
OPERATING CONDITIONS FOR INFRARED RADIATION MEASUREMENTS

Blackbody Source: 990 dial setting (1000° C), maximum opening.

Monochromator: .2 mm slit width, 1930 to 1450 drum number scan at 44.44 number/min, NaCl prism and slit window, dry nitrogen purge, 13 Hz chopper motor on.

Amplifier: coarse gain on 12, fine gain on 10, time response on 2, balance selector on output, test microwatts on 0, battery on.

Recorder: 2 in/min, 10 mv to 100 mv scale.

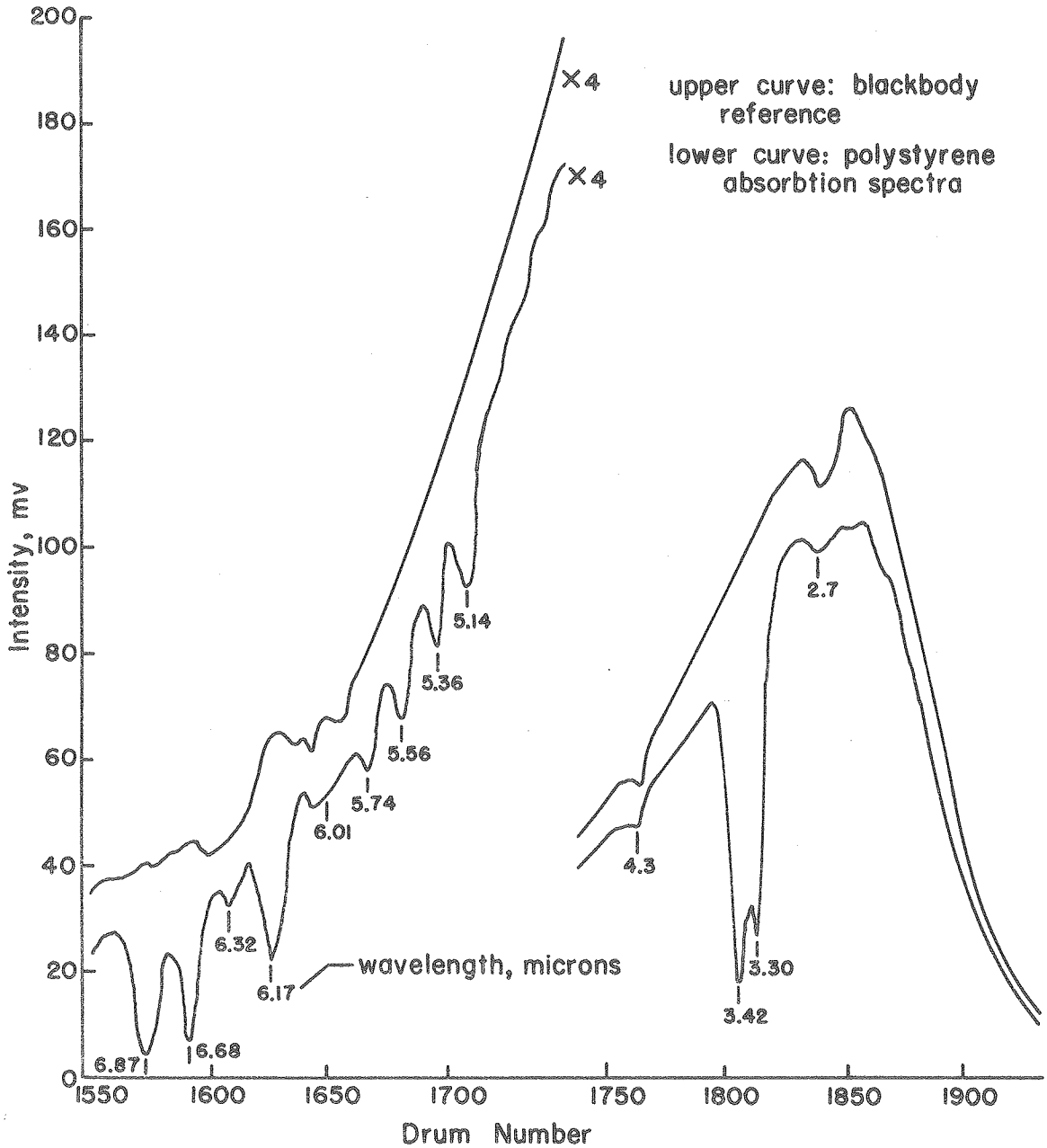

FIGURE III-11. Output of Monochromator Detector With and Without Polystyrene Film in Front of Window

IV. STRUCTURE OF THE FURNACE FLAMES

The structure of the furnace flame is described in this chapter. Representative data are presented for both the pure methanol and the methanol/coal flames.

A. Methanol as the Fuel

1. Temperature

The temperature structure was determined by measurements with a thermocouple as described in the previous chapter. Data were taken through each of the twelve access ports located every 7.1 cm along the furnace axis. About twenty data points were taken at each port, the distance between points being dictated by the temperature gradients encountered.

This information , uncorrected for thermocouple radiation losses, is shown on the temperature map in Figure IV-1. The radial distance is expanded by a factor of two to improve readability. The most striking feature is the asymmetry about the centerline. This could be due to a misalignment of the primary air and fuel jet relative to the centerline which results in an uneven distribution of fuel. However, another explanation is that the asymmetry is due to buoyant forces. This would be the obvious explanation if the temperature map were of a vertical slice through the furnace centerline. But, since it is a horizontal slice, the effect of buoyancy is more subtle.

For non-swirling hot jets, the Archimedes number, Ar, is a non-

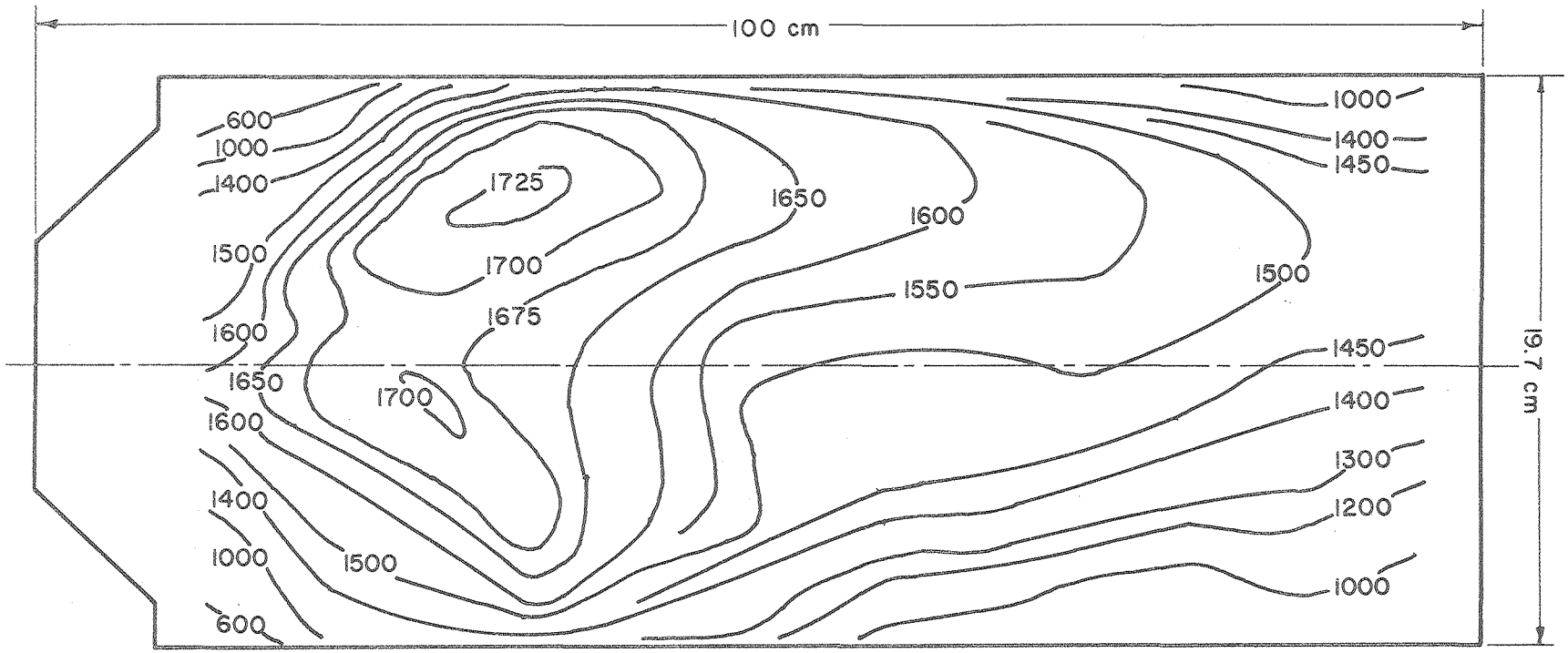

FIGURE IV-1.

Temperature (K) Distribution in Methanol Furnace (uncorrected)

dimensional parameter used to characterize the effect of buoyancy (Beér and Chigier, p 208)

$$Ar = \frac{dg\Delta T}{u^2 T_g}$$

where d is the diameter of the secondary air duct, g is the gravitational acceleration, u is the velocity of the secondary air, and ΔT is the difference between the cold air temperature and the combustion gas temperature, T_g. For the model furnace, $Ar \simeq .01$, which is just at the lower limit where buoyancy becomes significant. Buoyant forces tend to set up toroidal circulations perpendicular to the main flow in addition to bending the axis of the jet upward. If the flow is originally swirling, the toroidal circulations will add to the tangential velocity on one side and subtract from the velocity on the other, which in turn could cause an asymmetry in the mixing and general flame structure.

The maximum temperature obtained is a little over 1725 K as compared to a stoichiometric equilibrium adiabatic temperature of 2152 K. If the thermocouple is corrected for radiation loss, the measured temperature is still over 250 K below the theoretical maximum. This is due to heat loss to the water-cooled walls and the fact that the eddys are not necessarily made up of an instantaneously burning stoichiometric mixture.

Figure IV-2 shows radial temperature profiles at four different axial locations: 12.7 cm, 26.9 cm, 58.4 cm, and 86.9 cm from the nozzle inlet. The squares with the solid lines through them are the measured temperatures. The dotted lines are the estimated temperatures when radiation corrections are applied. In Figure a), which is the location closest to the furnace entrance, the combustion products have not yet penetrated the outer portion of the furnace, nor have they completely penetrated the fuel rich core. The radiation corrections are small near the walls because the temperatures are

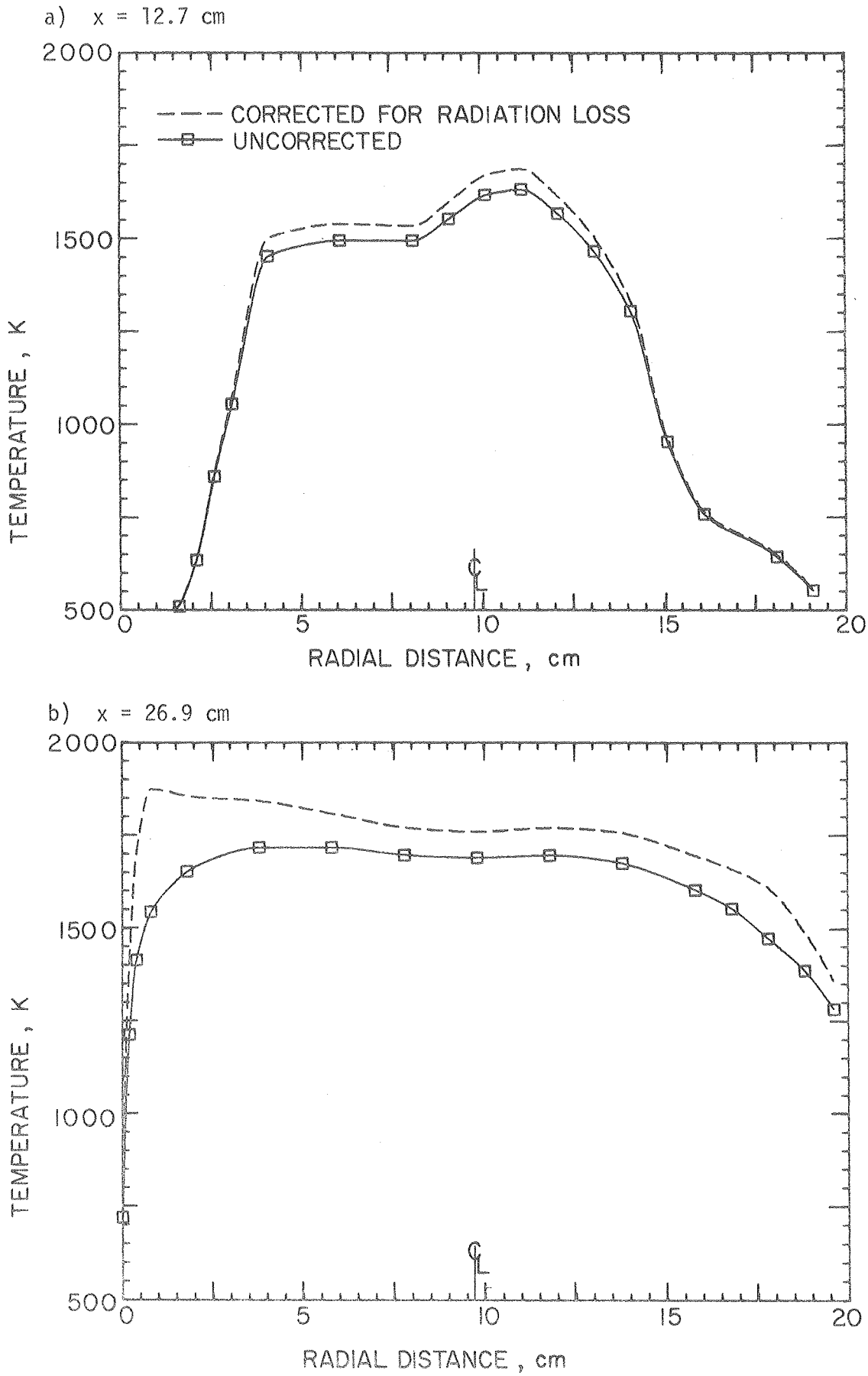

FIGURE IV-2. Temperature Profiles in Methanol Furnace

c) x = 58.4 cm

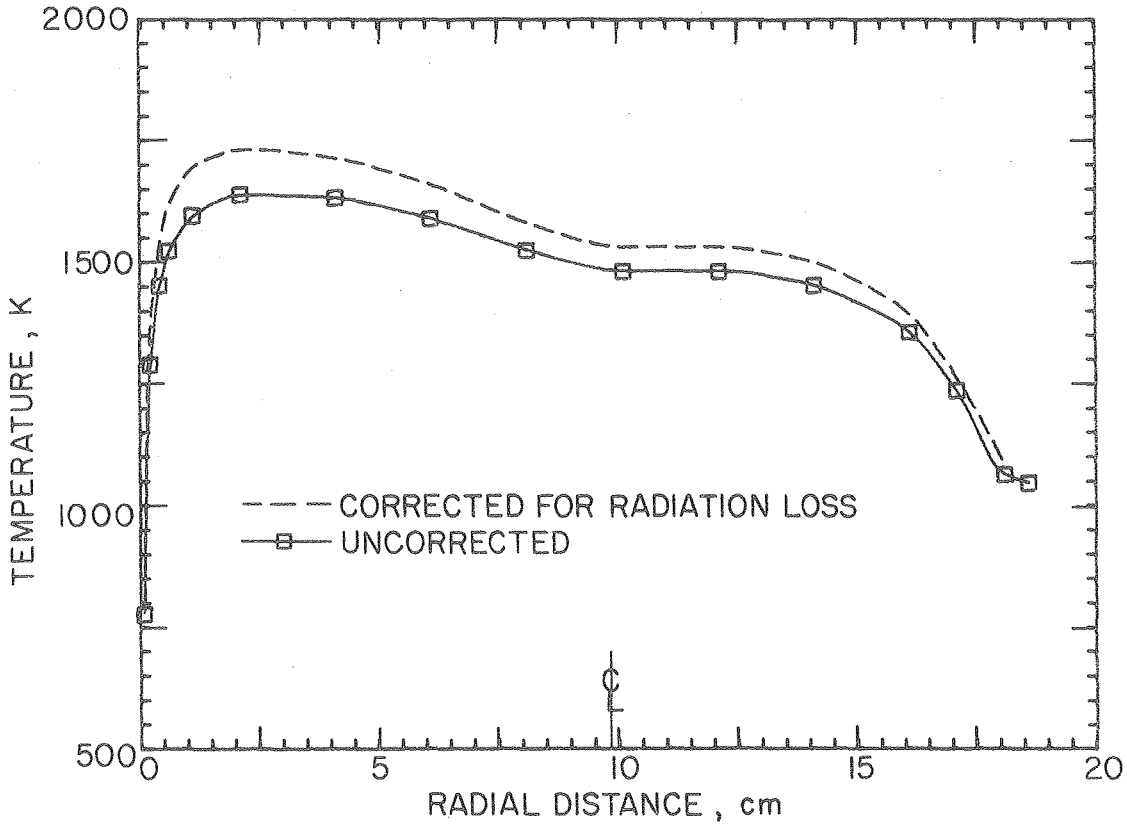

d) x = 86.9 cm

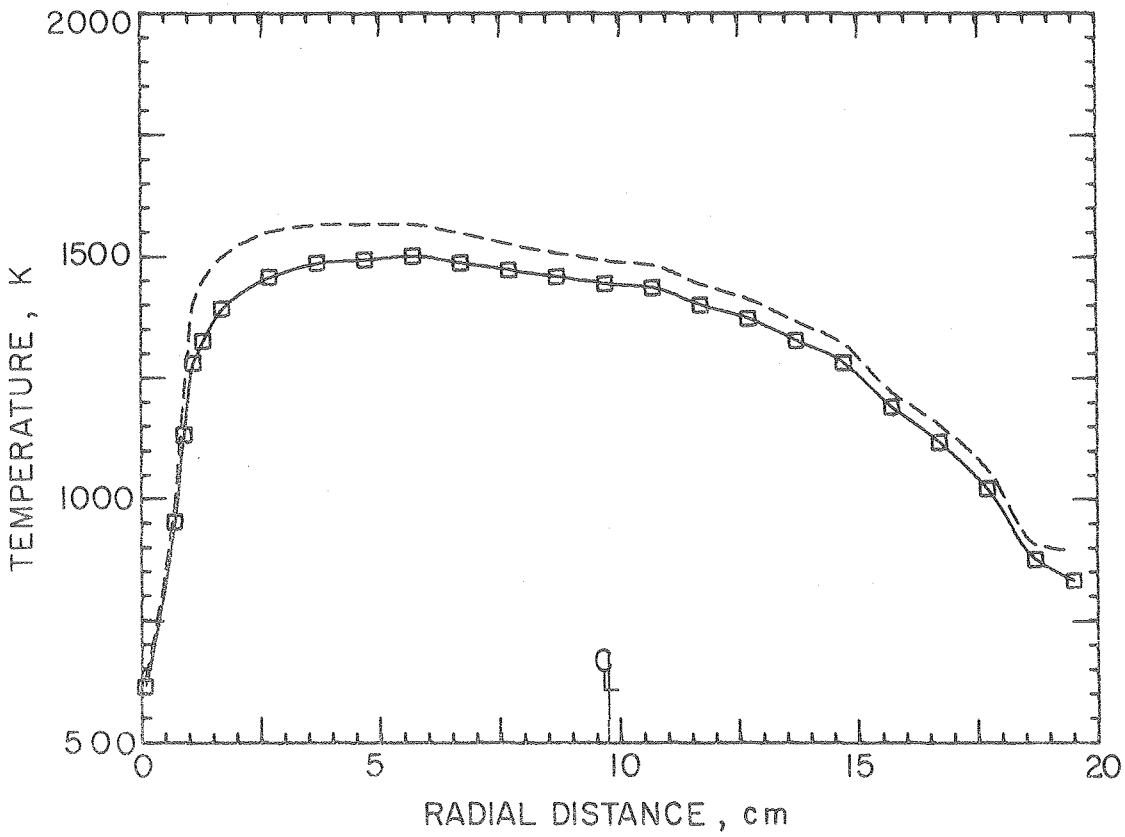

FIGURE IV-2. (continued)

low. In the center of the furnace, the corrections are small because the velocity, and thus, the Nusselt number, is large. By 14.7 cm further down stream, Figure b), the combustion temperatures have diffused across the entire diameter except for a cold boundary layer near the wall. The temperature corrections near the wall become quite large because the temperature is high and the velocity is low. The cooling effect of the wall becomes increasingly more apparent in Figures c) and d) as the gases approach the outlet of the furnace. The asymmetry noticed on the temperature map is visible in all of these plots.

2. Chemical composition

The stoichiometric equation of methanol reacting with air is

$$CH_3OH + 1.5\ (O_2 + 3.76\ N_2) = CO_2 + 2H_2O + 5.64\ N_2$$

To get a more realistic estimate of which products to expect in the furnace, the NASA equilibrium program, CEC-71 (Gordon and McBride, 1971), was run for two different equivalence ratios: $\Phi = 1.0$ and $\Phi = .9$. The stoichiometric case yields the composition which would be expected in the flame front while the lean equivalence ratio yields a composition expected from intimately mixing all of the incoming air and fuel before reacting. The calculated compositions are listed in Table IV-1.

Other than nitrogen, the predominant species is water. Figure IV-3 is a map of the measured water concentration, in volume percent, along a horizontal plane through the furnace centerline. The equilibrium value is obtained very quickly near the center of the furnace. The maximum level, greater than 24%, is more than that predicted by equilibrium. This is partly due to residual water which enters with the air (about .3%) and partly to the accuracy of the measurement itself, which is only good to 1%.

TABLE IV-1
ADIABATIC EQUILIBRIUM CONDITIONS FOR

$$CH_3OH(L)+\frac{1.5}{\Phi}(AIR)$$

P=1 ATM T_I=298 K

MOLE FRACTION OF:	Φ=1.0	Φ=0.9
N_2	.6410	.6581
H_2O	.2253	.2039
CO_2	.1077	.1018
A	.0077	.0079
CO	.0073	.0012
O_2	.0039	.0218
H_2	.0030	.0005
NO	.0015	.0026
OH	.0022	.0020
O	.0001	.0001
H	.0002	.0000
TEMPERATURE, K	2152	2037

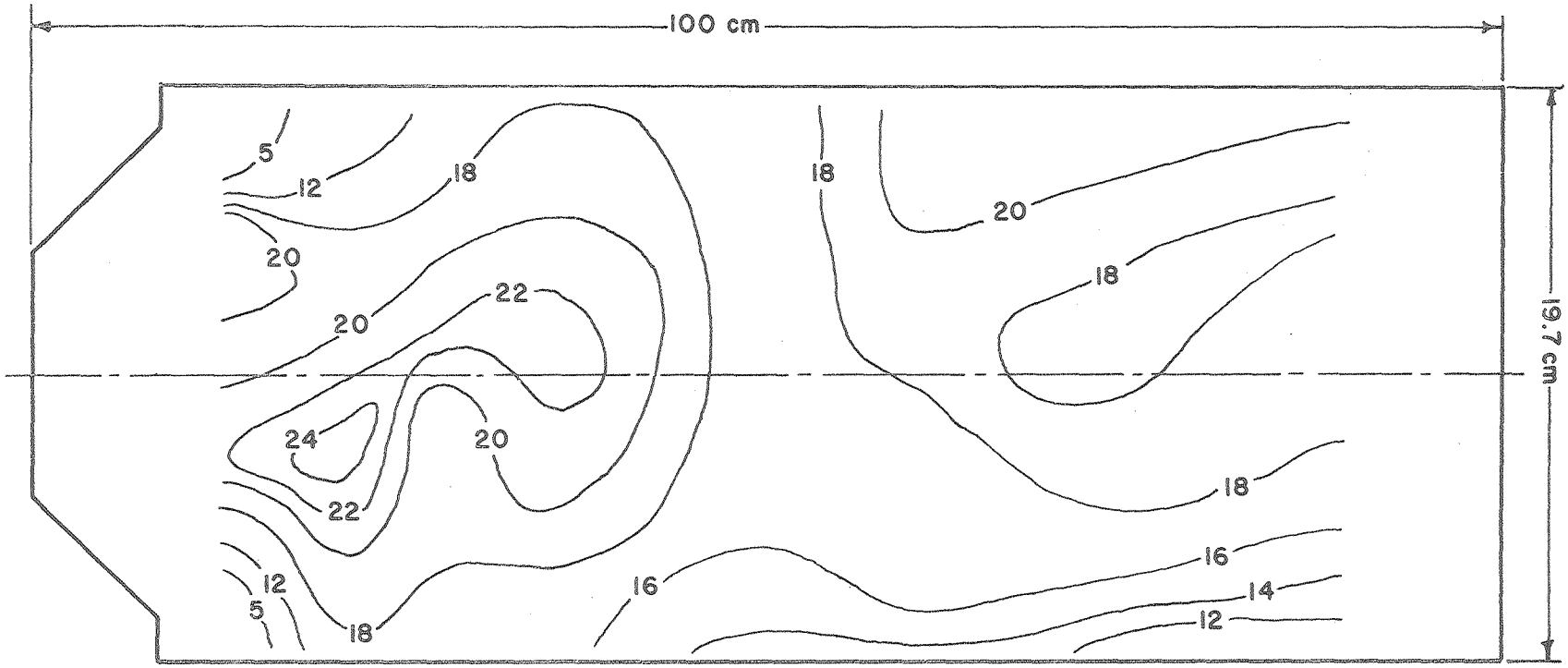

FIGURE IV-3. Distribution of H_2O Concentration (%, vol.) in Methanol Furnace

The carbon monoxide concentration, shown in Figure IV-4, is high near the entrance of the furnace. This is as expected. Values go from 8% deep within the fuel jet to less than .1% in the secondary air stream and near the exit.

Unlike carbon monoxide, carbon dioxide peaks later in the furnace. It reaches equilibrium in some regions, as can be seen in Figure IV-5.

Radial plots of composition are given in Figures IV-6a through IV-6e Incoming concentrations of methanol are as high as 50% in the primary stream, but within the first 12.7 cm of the furnace the maximum drops to less than .3% as shown in Figure IV-6a. By the second measuring port, 19.8 cm downstream from the nozzle, the fuel is down to around 100 ppm. The fuel level remains below about 50 ppm throughout the rest of the furnace, and by 72.6 cm it has dropped below the detectable limit of 1 ppm.

The graphs showing H_2O, CO_2, and CO at four different axial locations are complimentary to the composition maps already discussed. Notice that by 26.9 cm, the species have diffused across the furnace and sharp gradients no longer exist. The build up of CO_2 at the expense of CO can be seen in Figures IV-6c and d.

The dotted lines shown only in graphs d and e are estimates of the oxygen concentrations. Because the nitrogen and oxygen elute from the gas chromatograph at the same time (see Figure III-6), only their sum can be determined exactly. For fuels with no oxygen in the molecule, it can be assumed that the ratio of nitrogen to oxygen atoms is constant throughout the flame, and thus, knowing the total $N_2 + O_2$ concentration is sufficient to determine both the N_2 and O_2 concentrations separately. For the methanol flame, the O atom to N atom ratio is .85 in the primary stream and .27 in the secondary air stream. As the two streams mix, the ratio approaches

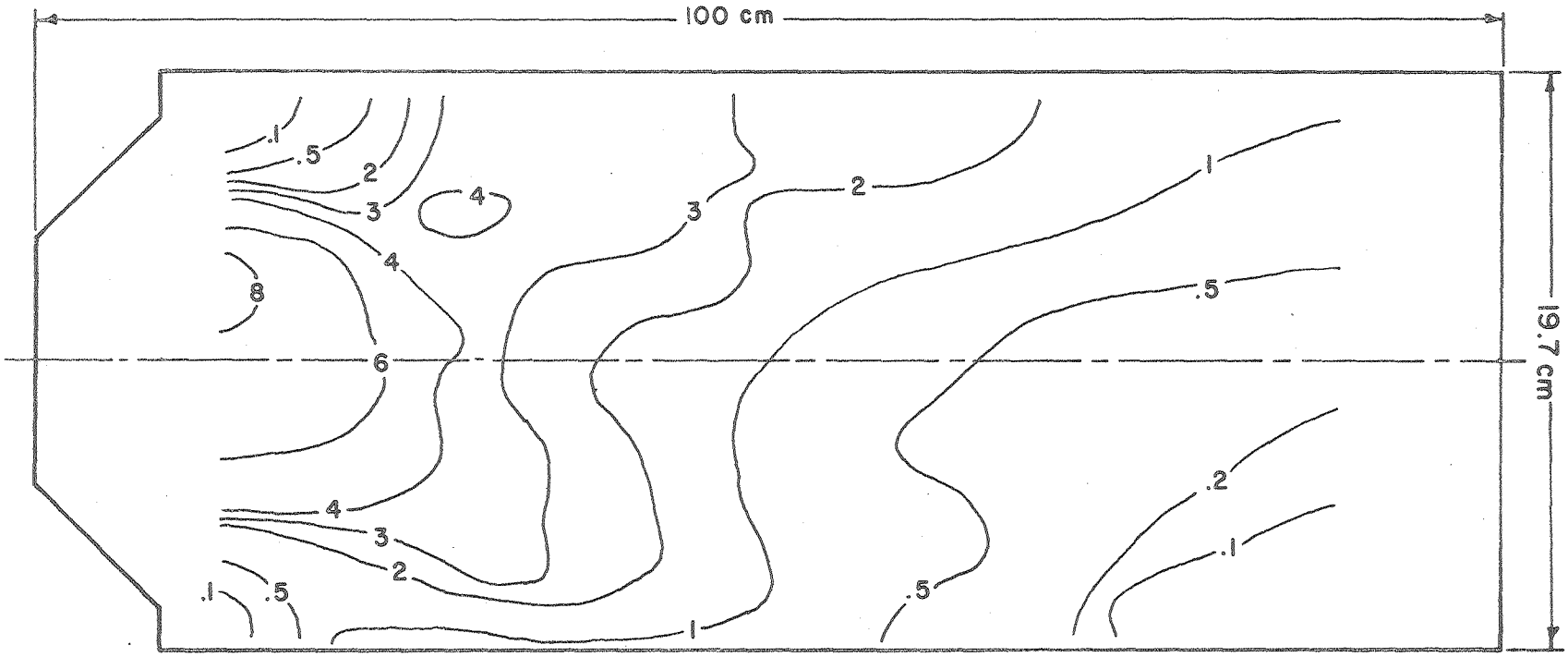

FIGURE IV-4. Distribution of CO concentration (%, vol.) in Methanol Furnace

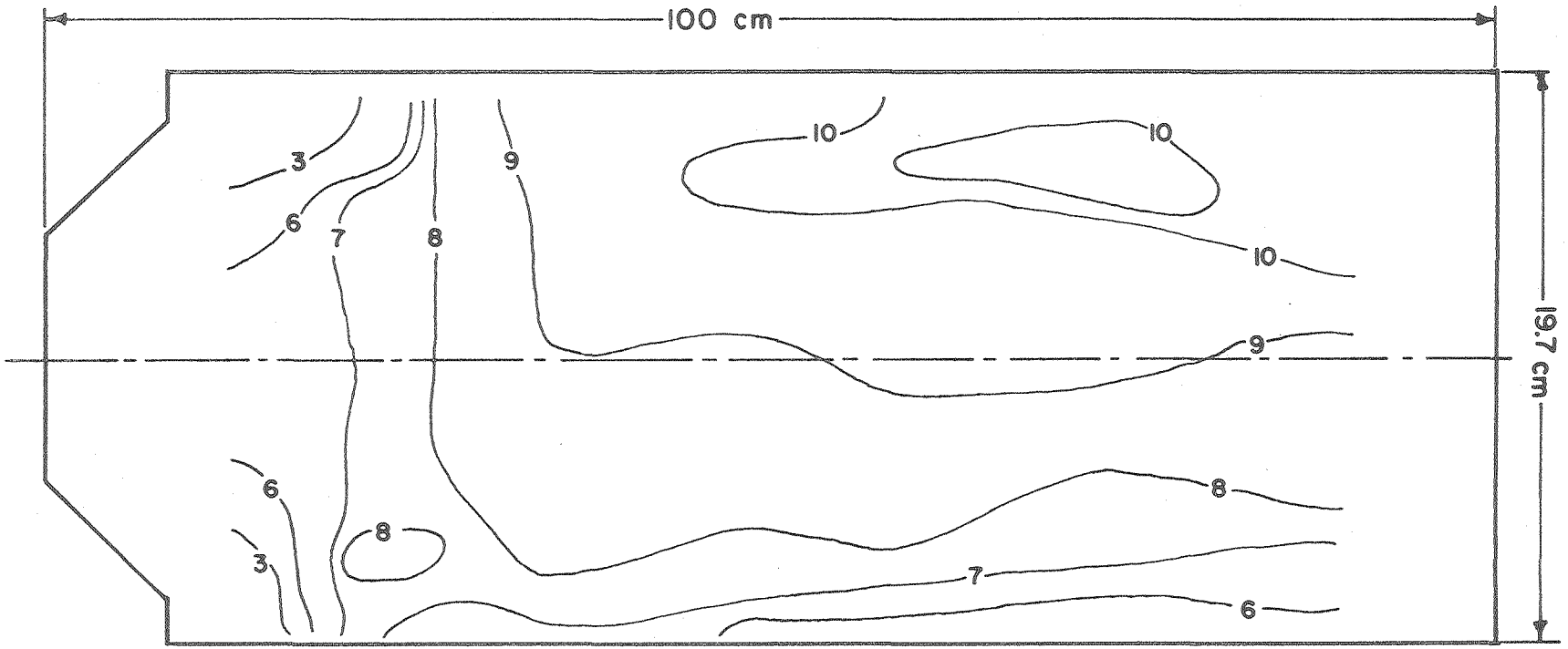

FIGURE IV-5. Distribution of CO_2 Concentration (%, vol.) in Methanol Furnace

0 0 0 4 7 0 0 5 5 3

a) CH_3OH Profiles

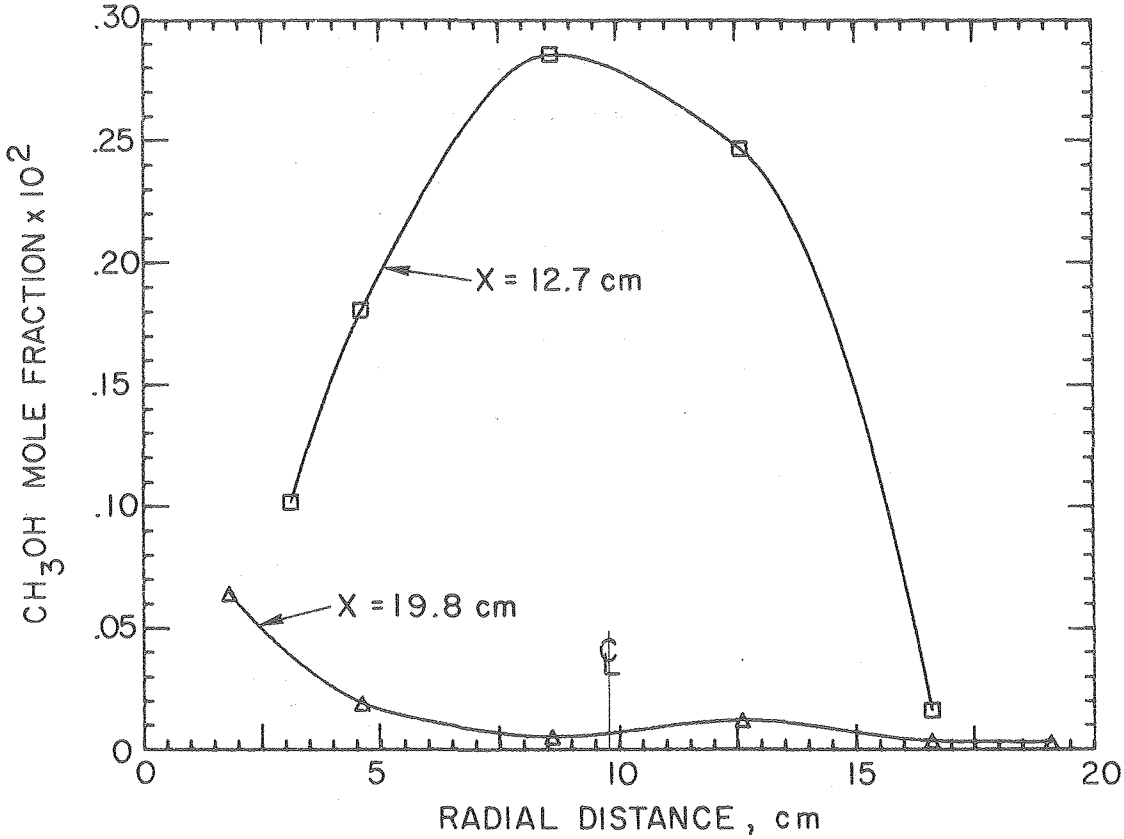

b) H_2O, CO_2, and CO Profiles at x = 12.7 cm

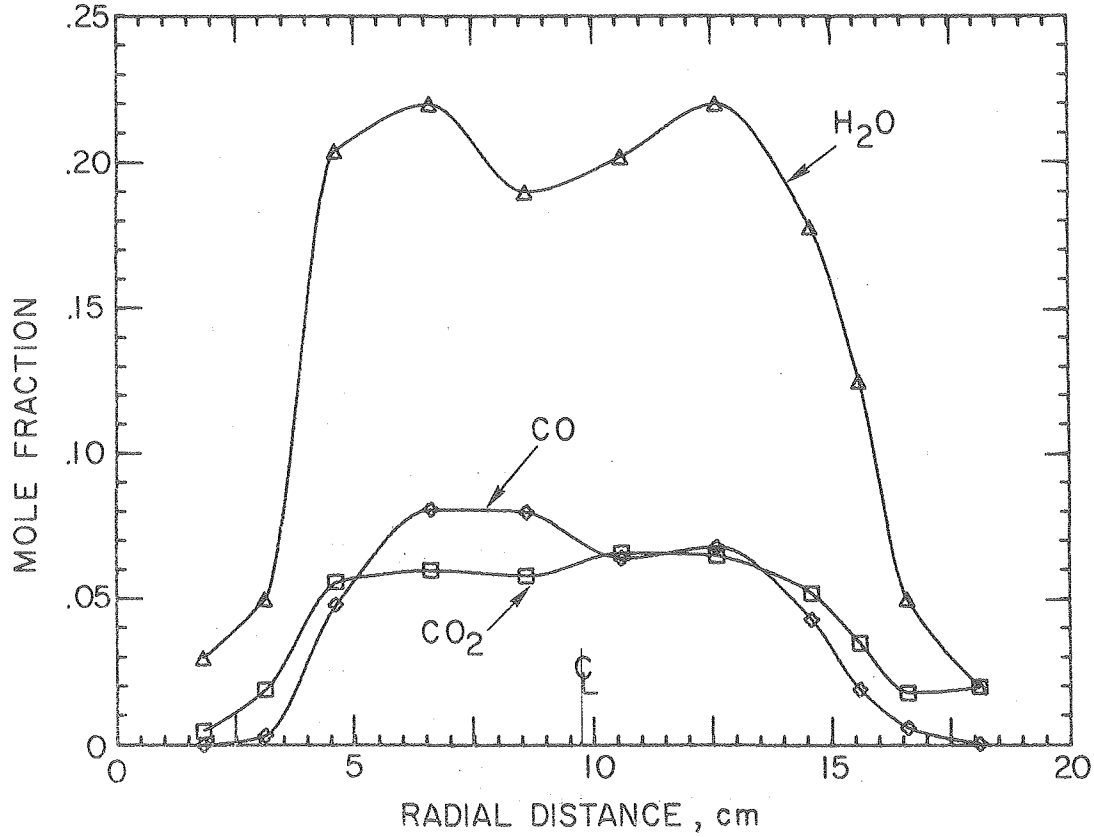

FIGURE IV-6. Chemical Composition of Methanol Furnace

c) H_2O, CO_2, and CO Profiles at x = 26.9 cm

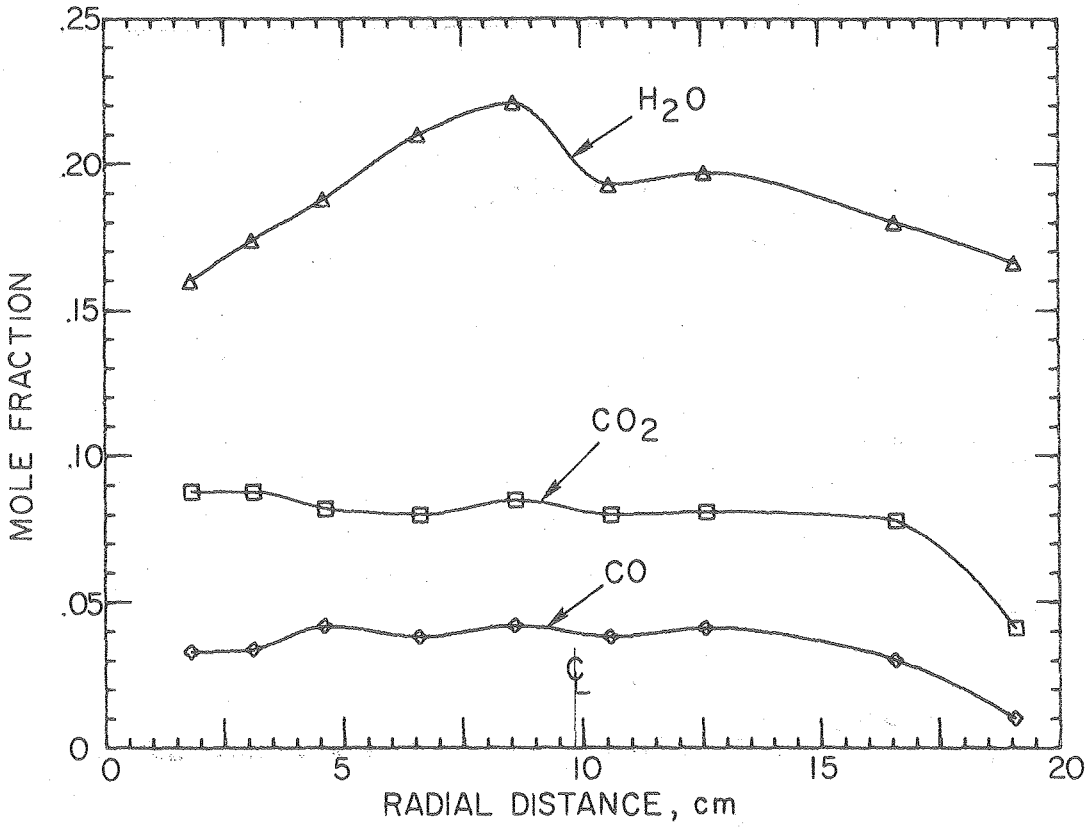

d) H_2O, CO_2, CO, and O_2 Profiles at x = 58.4 cm

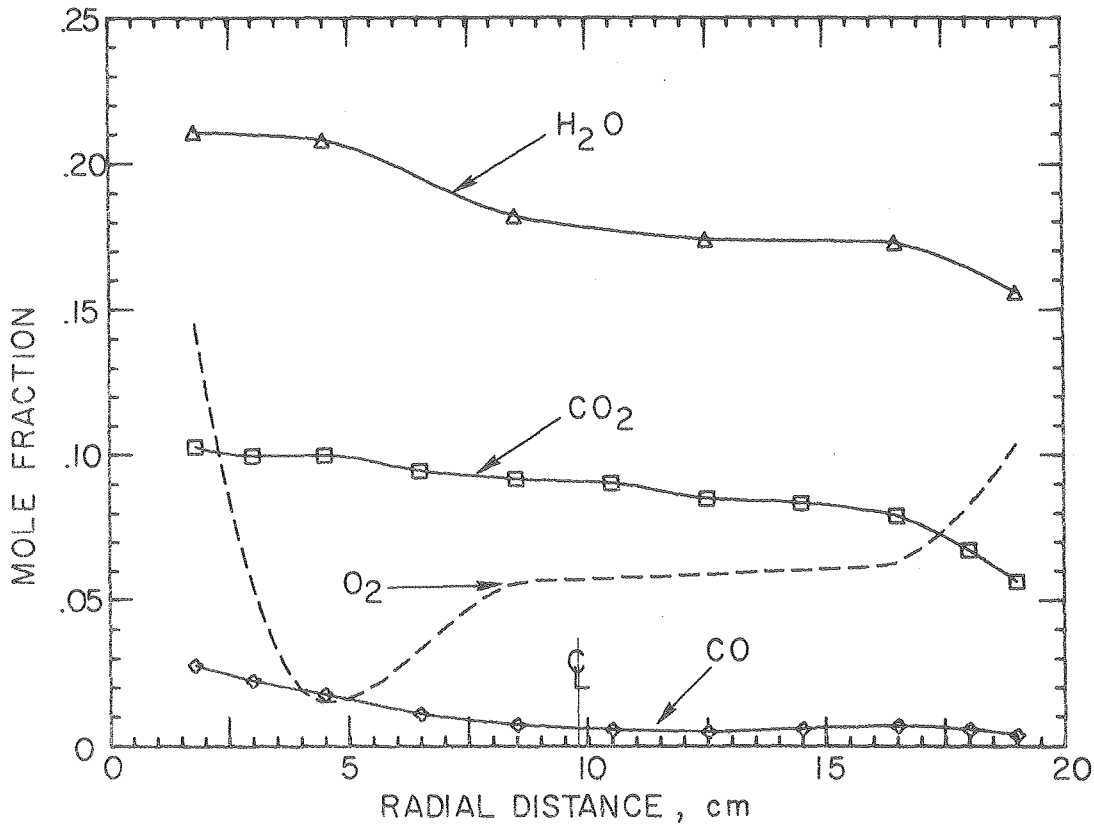

FIGURE IV-6. (continued)

e) H_2O, CO_2, CO, and O_2 Profiles at x = 86.9 cm

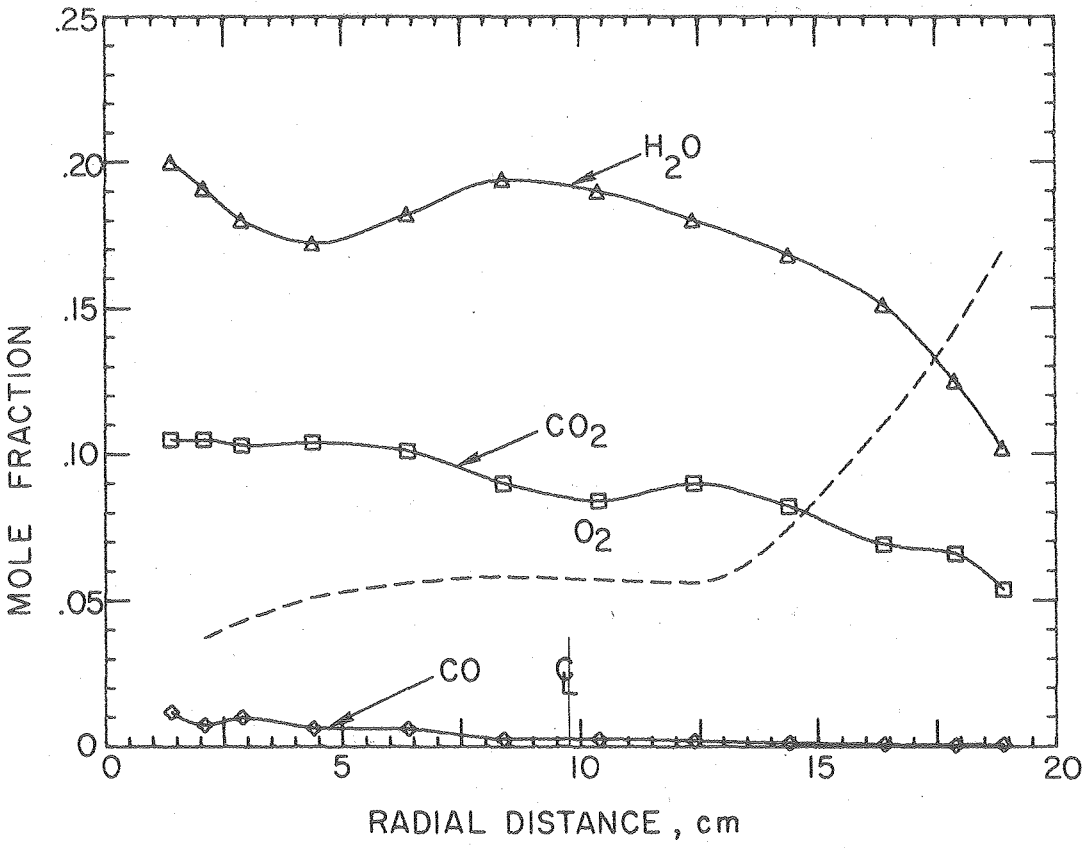

FIGURE IV-6. (continued)

an overall average of .35. It is assumed that the mixing is sufficient by a distance of 58.4 cm downstream to use the .35 ratio. The dotted lines are derived on this basis.

Small concentrations of propane, 26 ppm and less, were detected early in furnace near the cold walls. Its presence is, undoubtably, due to residual propane from the ignition system which diffuses into the secondary air stream.

An effort was made to measure formaldehyde levels in the furnace with chromatographic techniques. The column used is capable of separating methanol/water/formaldehyde mixtures but the thermal conductivity detector is not sensitive enough to measure the low levels encountered (less than 100 ppm). The ruthenium converter/FID set-up allows detection of formaldehyde down in the 10 ppm range under ideal conditions, but the presence of CO_2 creates a resolution problem with the chromatogram. As a result, HCHO was detected only once at a level of less than 75 ppm (the lower detection limit under the experimental conditions) at a location 12.7 cm downstream and close to the centerline.

The nitric oxide and total NX distributions are shown in Figures IV-7 and IV-8. There are two important things to notice about these maps. First, the nitric oxide levels are low both in the high temperature regions and at the exit of the furnace, especially when compared to the equilibrium level of NO which is about 2000 ppm. This is in agreement with the trend mentioned by Lerner (1973) for a full scale boiler.

Second, the NO makes up less than 2/3 of the total NX concentration. Recently, other experimenters have observed similar results (Schefer, 1976). This is more evident on the radial plots of Figure IV-9. For an axial distance equal to 26.9 cm and greater, most of the remaining NX is probably NO_2.

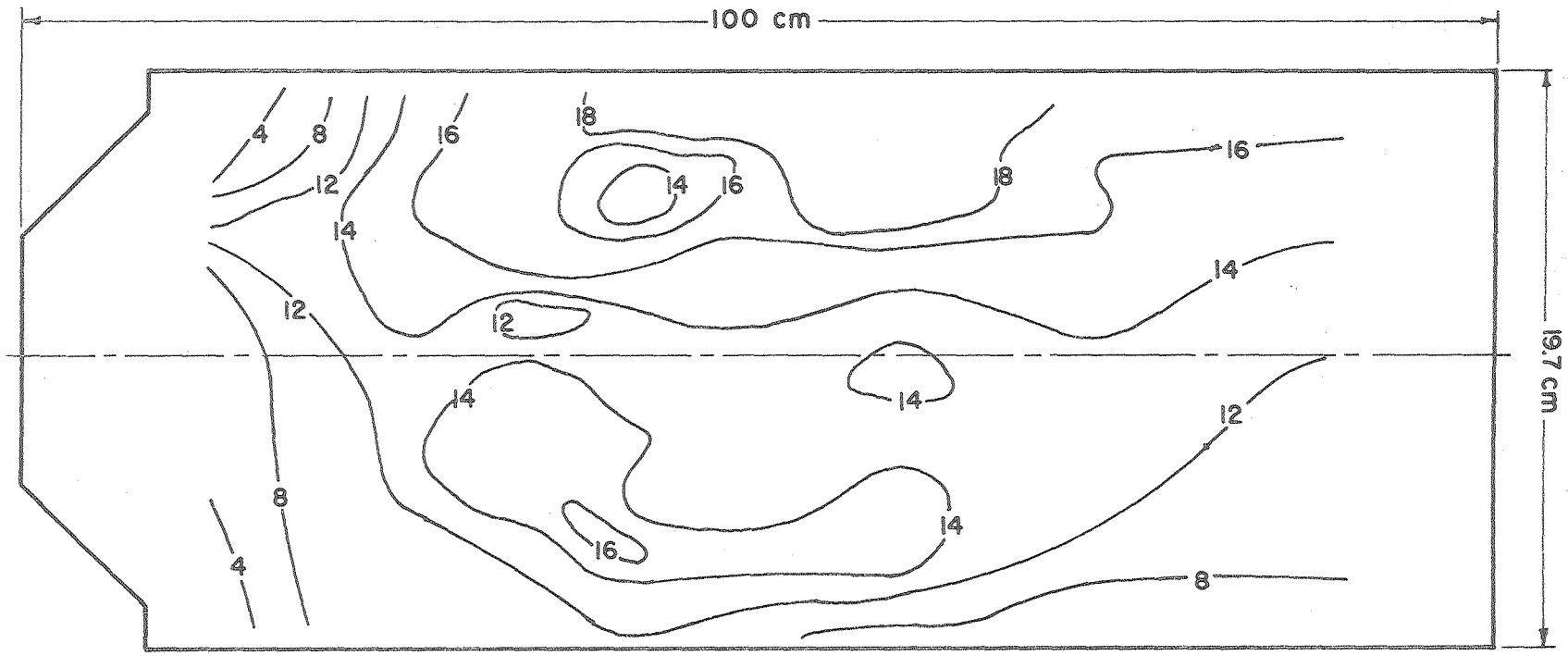

FIGURE IV-7. Distribution of NO Concentration(ppm, vol.) in Methanol Furnace

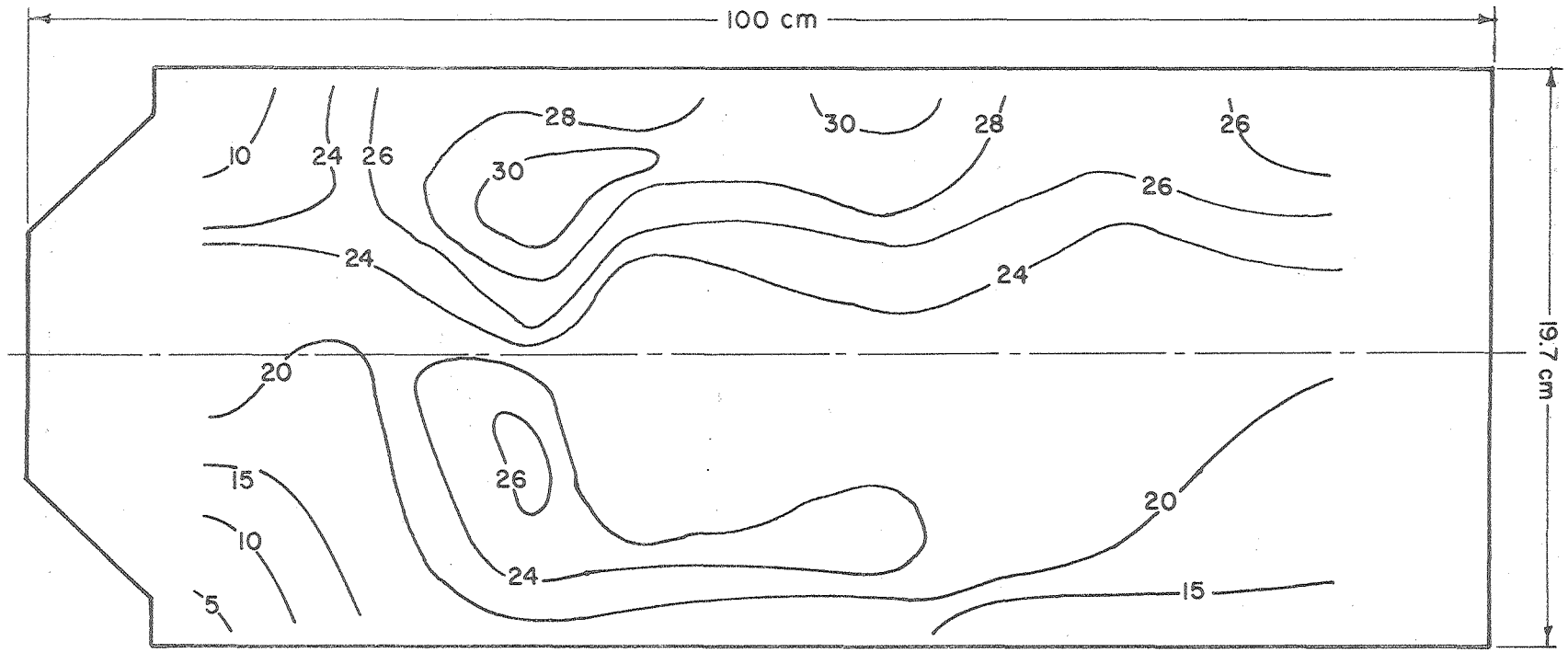

FIGURE IV-8. Distribution of NX Concentration (ppm, vol.) in Methanol Furnace

a) x = 12.7 cm

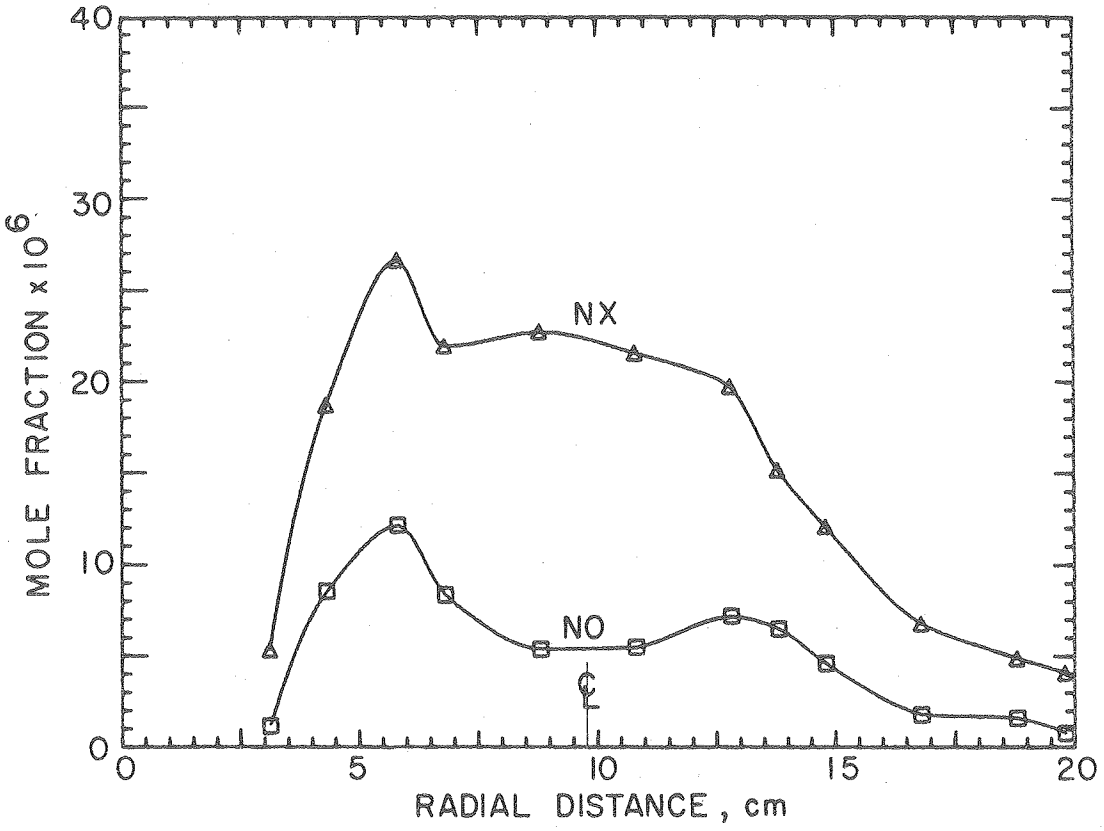

b) x = 26.9 cm

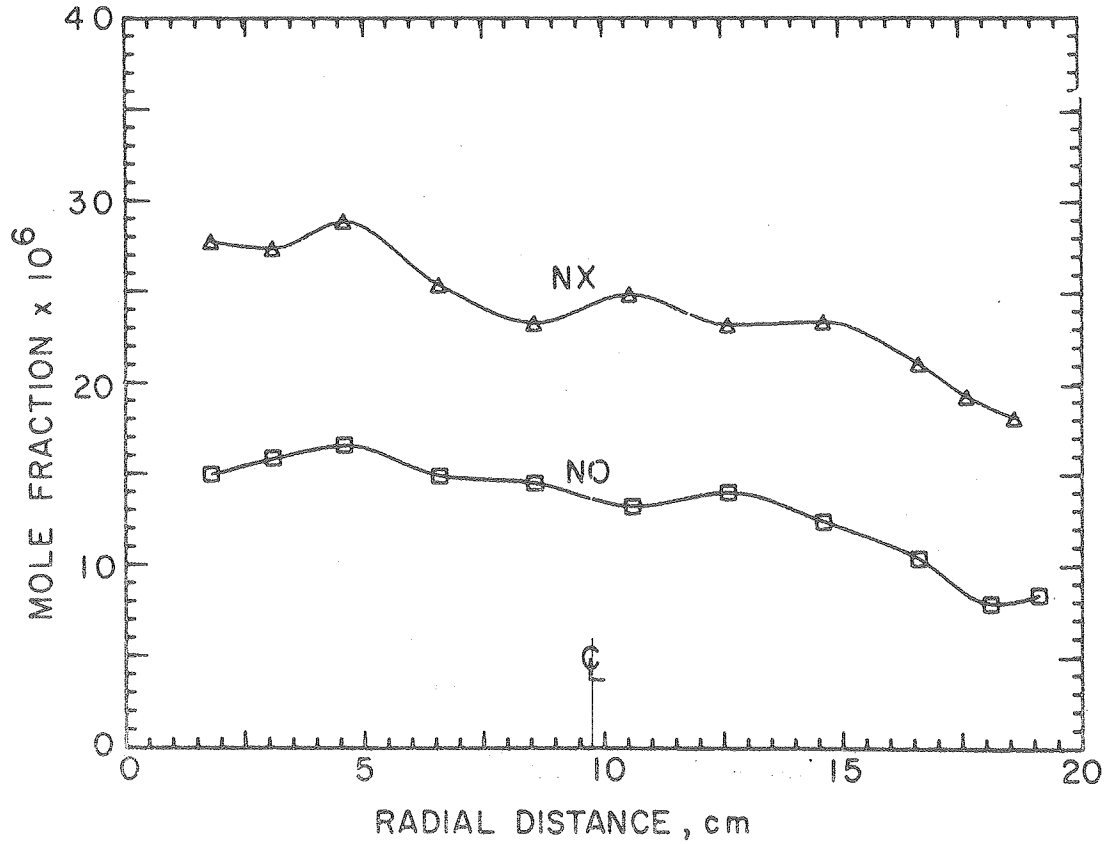

FIGURE IV-9. Profiles of NO and NX in Methanol Furnace

c) x = 58.4 cm

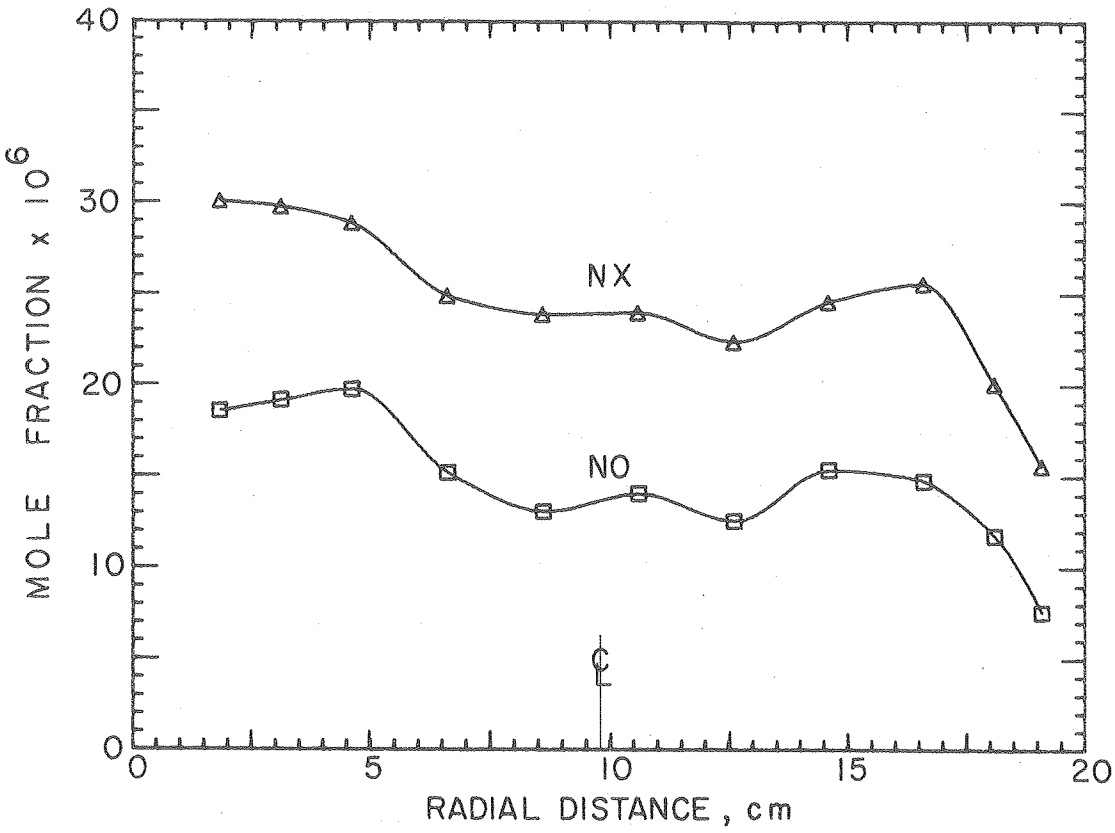

d) x = 86.9 cm

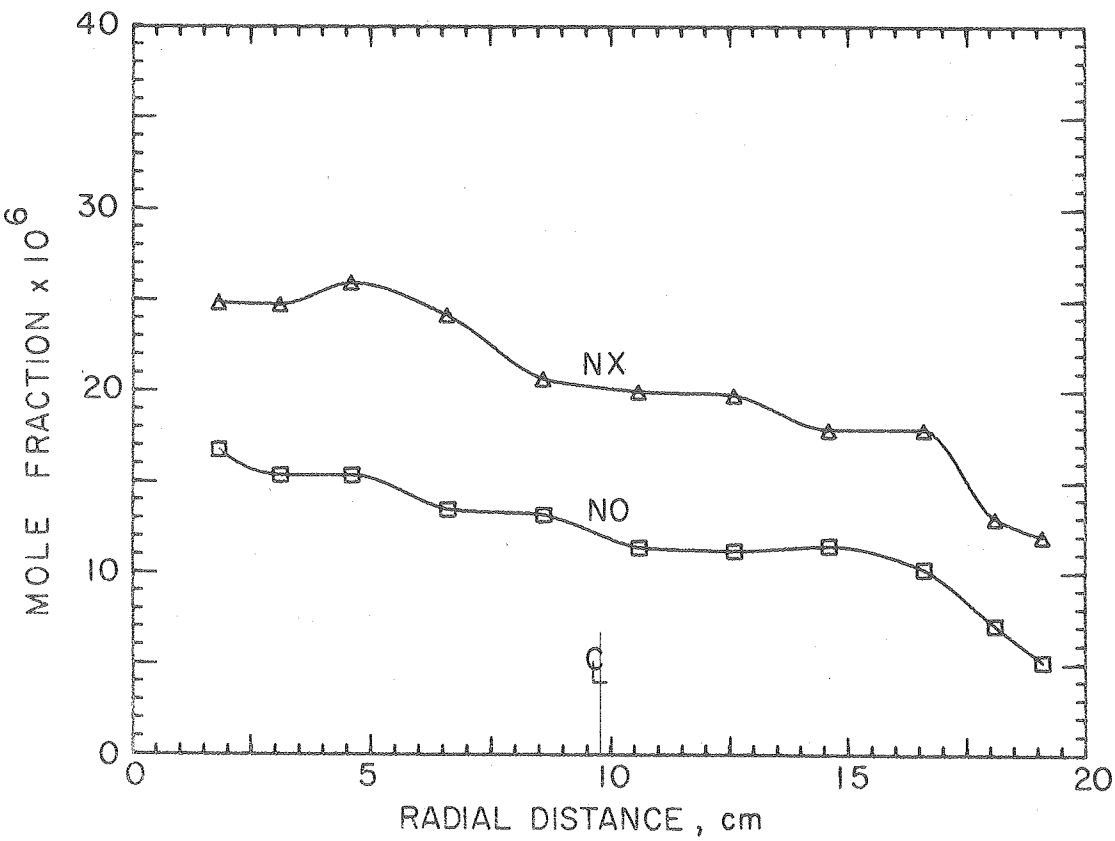

FIGURE IV-9. (continued)

Closer to the inlet, Figure IV-9a, the NX is about three times the NO concentration. In a fuel rich region such as this, the difference is less likely due to NO_2 and more likely due to HCN and NH_3.

3. Comparison of structure with theoretical predictions

From the stand-point of analytical modeling, if reasonable agreement between proposed model and experiment is desired, the furnace should be axisymmetric and the flow such that the governing equations are parabolic in nature, i.e. without recirculation. In addition, the flow should be of single phase and the oxidation kinetics of the fuel well-known. Unfortunately, except for the axisymmetric shape of the furnace, these conditions are not met.

The program of Gosman, Pun, Runchal, Spalding, and Wolfstein (1969) for recirculating flows was used to predict the shape and length of the flame zone. Application of the program to the present experiment should have been straight forward, but, as is often the case when using someone else's complicated program, problems were encountered. Because of time and money, many approximations and short-cuts have been made, and as a result, the predicted structure does not mimic the experimental structure successfully.

The first problem considered is one of geometry. The program is written entirely in cylindrical coordinates with boundaries either parallel or perpendicualr to the axis. The conical quarl in the furnace entrance has to be approximated as a series of step expansions, and requires considerable modification to subroutines BOUNCT, FDEQCT, ADF and MAIN as well as to the output formats. These steps become sources of numerical instability becuase the grid is not small enough to model the fluid mechanics at these locations properly.

The grid size is the second problem. The program is written with a maximum grid of 21 by 21. This is expanded to 25 by 25 but still does not

cover the furnace sufficiently. The grid used is shown in Figure IV-10. Since the main interest in the study is the combustion and not the heat transfer to the wall, the grid is densest where the chemical reaction is expected to occur and coarsest near the wall. Unfortunately, the errors which occur near the wall make their presence felt throughout the furnace.

The kinetics of methanol oxidation presented the next problem. Based upon the experiences of others (Schefer, 1976; Altenkirk, 1975) it was decided that modeling the kinetics of anything but the simplest fuel/oxidizer system was a several years project in itself. Additionally, little work has been done on the detailed kinetics of high temperature methanol oxidation and no global rate equations have been derived. For these reasons, the approach used by Gosman, et al., was adopted; that is, an infinitely fast reaction of fuel plus oxidizer going to products wherever the equivalence ratio reaches a value of one.

The proper way to model the incoming fuel spray and primary air stream is not obvious. To handle the liquid phase, an additional set of mass, momentum, and energy differential equations should be solved. Instead, it is assumed that the fuel is vaporized before entering the furnace and that half of the primary air has reacted with the fuel to equilibrium. Another aproximation is that the primary air and fuel stream enter parallel to the axis. In reality, the spray enters with a conical shape, thus increasing lateral mixing and forcing the flame to spread more rapidly.

The velocity profiles are assumed flat in both primary and secondary streams, and the diameter of the primary jet is increased to attain the correct momentum.

The treatment of turbulent transport properties is another difficult area. As a gross aproximation, the effective turbulent viscosity is

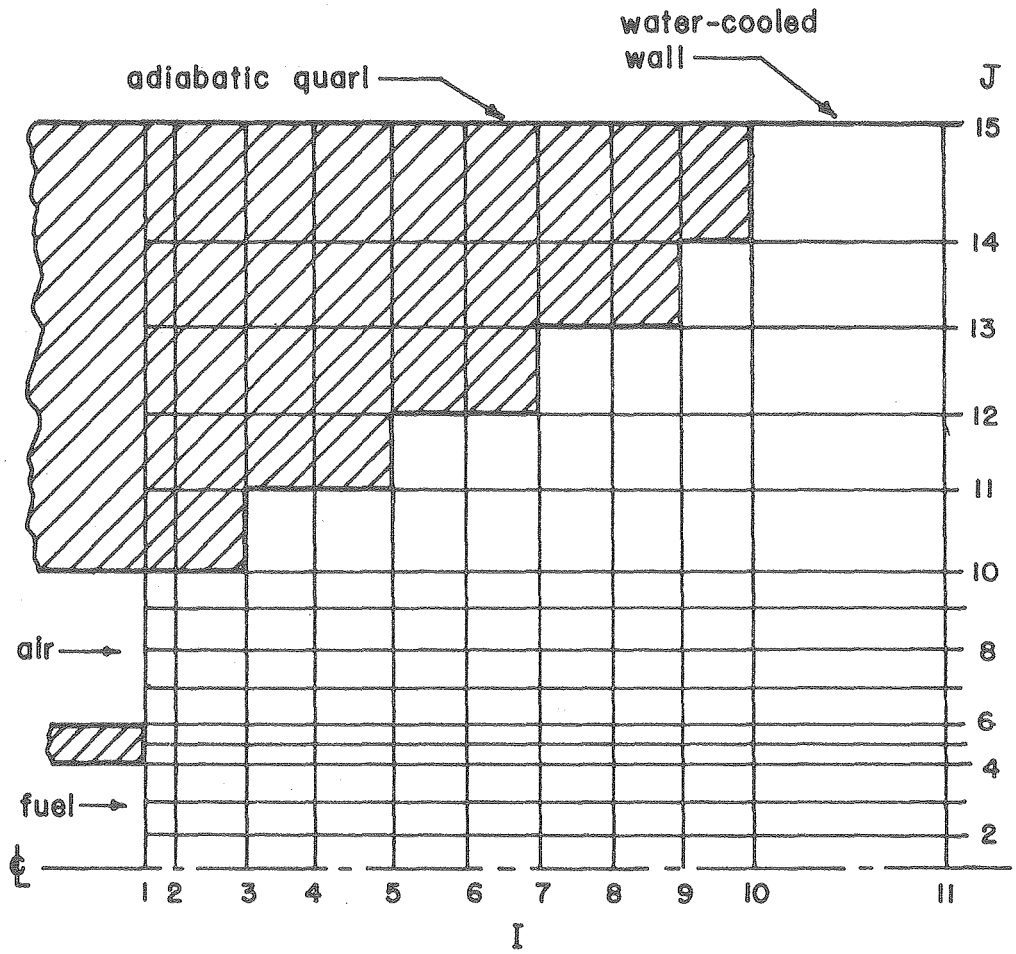

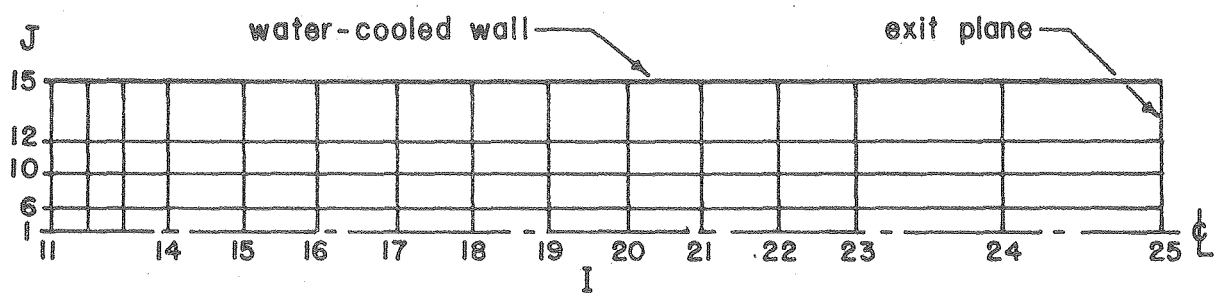

FIGURE IV-10. Grid System Used for Computer Simulation of Methanol Furnace

computed as suggested by Gosman, et al.

$$\mu_{eff} = K \left[\frac{D^2 \rho^2}{W} (\dot{m}_f V_f^2 + \dot{m}_o V_o^2) \right]^{1/3}$$

where K is a constant, D and W are the chamber diameter and length, $\dot{m}$ is the mass flow rate in the fuel or oxidizer stream, and V is the inlet velocity for the fuel or oxidizer stream. ρ is the local density. An obvious limitation to this approximation is the inability to predict a decrease in effective viscosity as one approaches the walls of the furnace. The Schmidt and Prandtl numbers are set equal to one so that the turbulent diffusion of species and temperature are controlled by the same expression.

A summary of the input parameters is given in Table IV-2.

TABLE IV-2
INPUT PARAMETERS FOR NUMERICAL MODEL OF METHANOL FURNACE

Chemical Reaction:
Fuel (.923 CH_3OH + .077 CO_2 + .154 H_2O + .868 N_2) +
Oxidizer (1.384 O_2 + 5.206 N_2) =
Product (1.00 CO_2 + 2.00 H_2O + 6.07 N_2)

Air/Fuel Weight Ratio (STC): 3.167

Enthalpy of Combustion (HC): 3763 Btu/lb primary
Primary Enthalpy (HP): 4187 Btu/lb primary
Secondary Enthalpy (HS): 155 Btu/lb Primary

Primary Inlet Velocity (VINP): 116.5 ft/sec
Secondary Inlet Velocity (VINS): 19.89 ft/sec
Primary Inlet Swirl Velocity (VTP): 51.3 ft/sec
Secondary Inlet Swirl Velocity (VTS): 15.54 ft/sec

Boundary Conditions:
Adiabatic expansion section
Constant temperature (672° R) cylindrical walls
Zero gradients at exit and centerline

Reference Viscosity: 2×10^{-5} lb_m/sec-ft

After debugging the program, it was allowed to run through 200 iterations (at a cost of $14 on the CDC 7600 computer). Convergence was obtained everywhere except for the stream function near the protruding steps of the expansion section.

The calculated axial and tangential velocity profiles are plotted in Figure IV-11. The axial velocity starts out peaked at 13.2 cm and gradually flattens out. The Reynolds number based upon the exit diameter and total mass flow is about 8000 and the furnace is less than five diameters long, so the velocity profile should not be expected to be near fully developed. No velocity data was taken, though, so the accuracy of the calculation remains untested. From Figure IV-11b, the early dissipation of the swirl is visible. By the exit of the furnace it has almost completely disappeared. The Nusselt number used in the thermocouple corrections is based on these velocity profiles.

The calculated temperatures are compared with the corrected experimental measurements in Figure IV-12. The over-predicted temperature early in the flame is due to the thin flame approximation. The rapid drop in temperature in the outer half of the furnace is not noticed in the measured values. Three factors contribute to this. First, the grid becomes very coarse in this region, so the boundary layer is artificially thickened. Second, the turbulent transport properties are not correctly modeled. And, third, the computer model does not account for the radial component of the fuel jet in the conical spray.

Figure IV-13 shows the final numerical calculation. It compares the predicted CO_2 mole fraction and the experimental CO_2 mole fraction. Once again, agreement is not satisfactory. The over-prediction near the wall is caused by the constraint that the three grid points nearest the wall

a) Axial Velocity

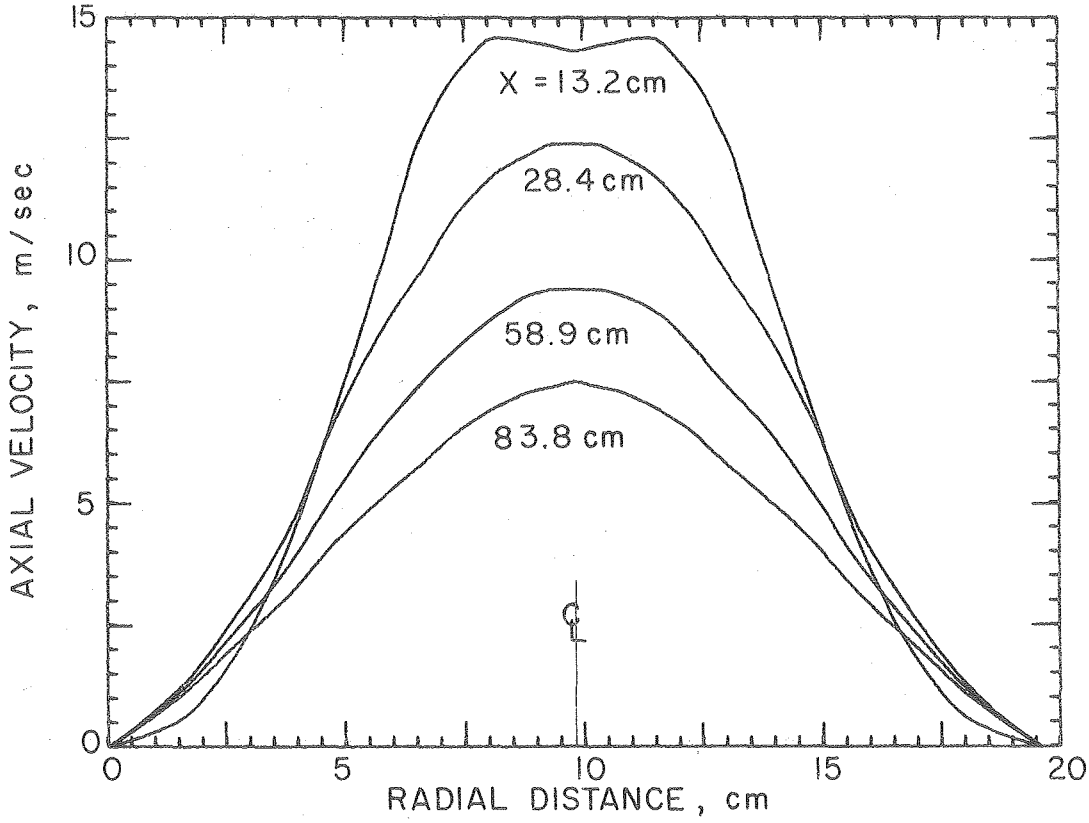

b) Absolute Value of Tangential Velocity

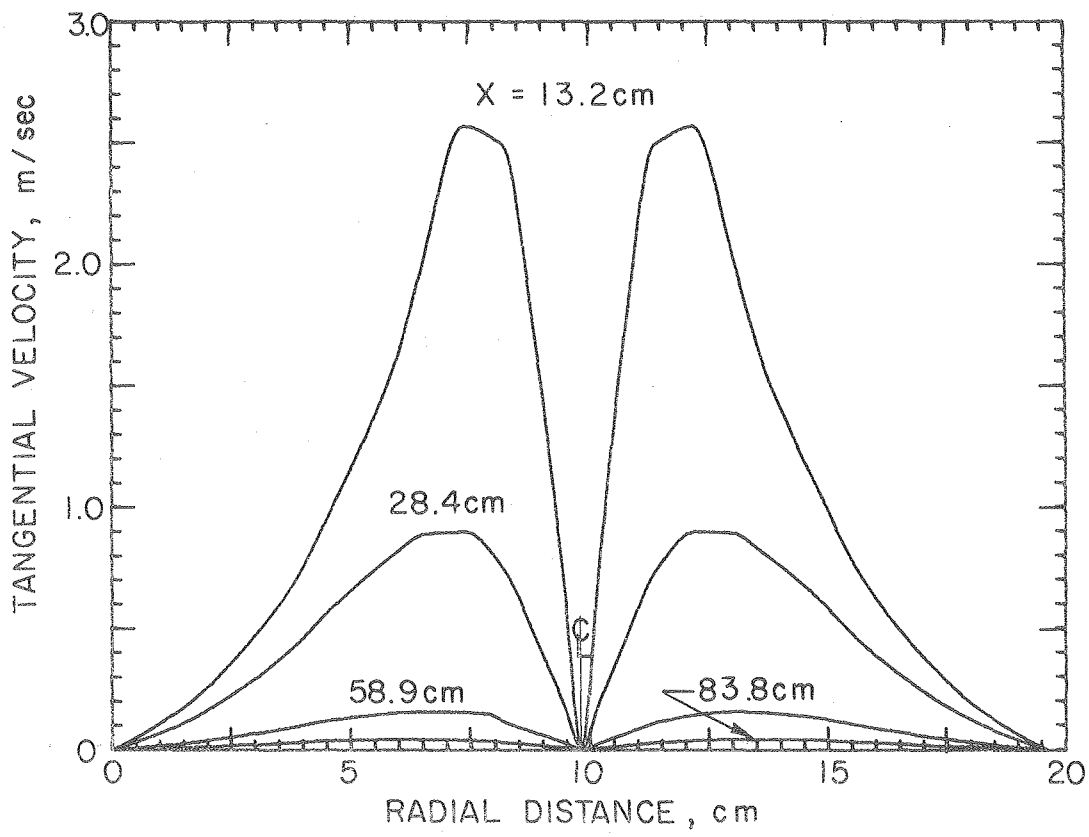

FIGURE IV-11. Computer Predicted Velocity Profiles in Methanol Furnace

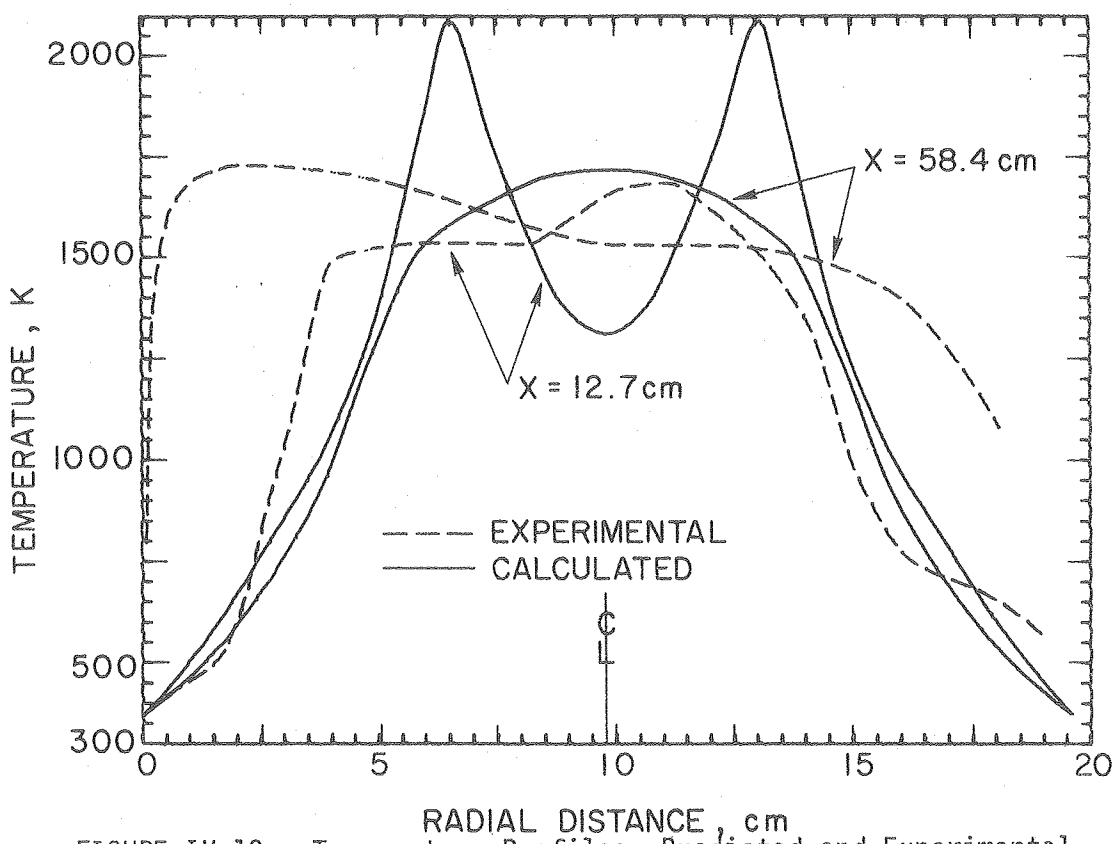

FIGURE IV-12. Temperature Profiles: Predicted and Experimental

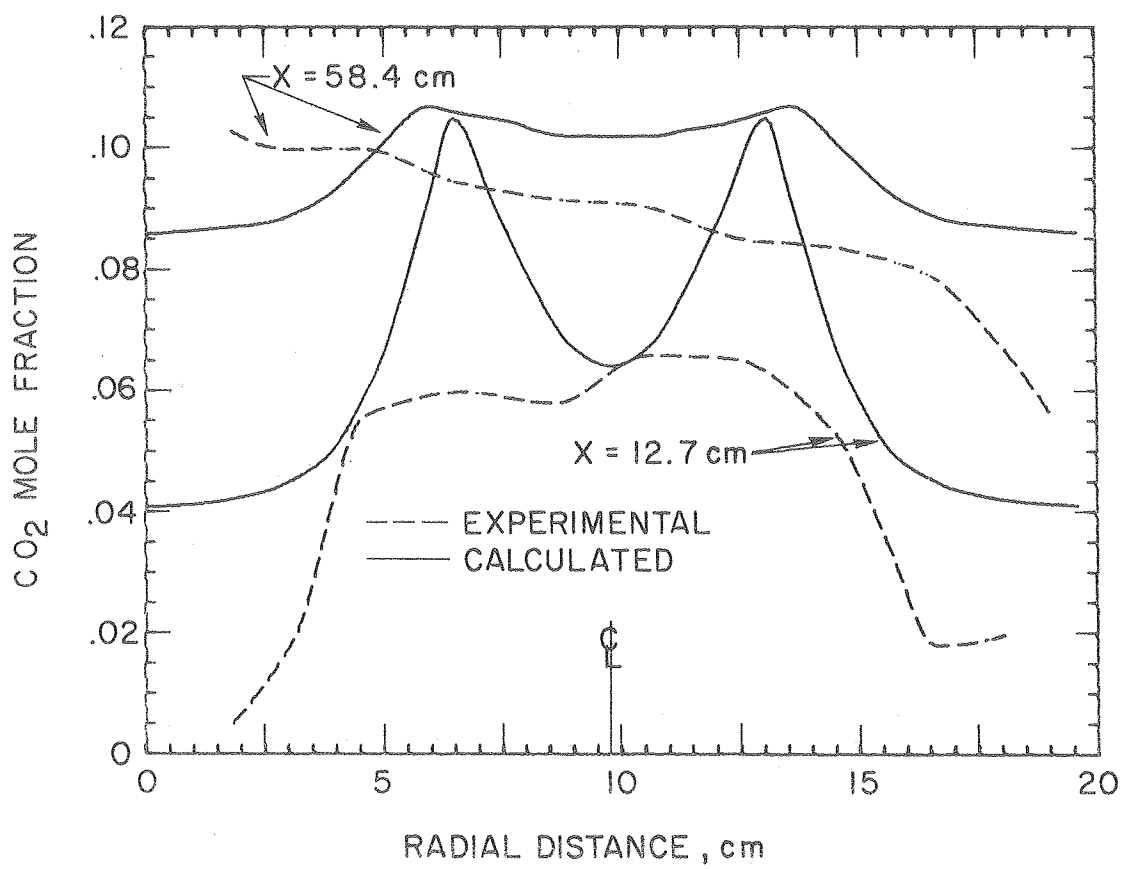

FIGURE IV-13. CO_2 Concentration Profiles: Predicted and Experimental

have a parabolic curve-fit. The coarse grid means that this effect is extended well outside the region of applicability.

B. Methanol/Coal Slurry as the Fuel

A slurry containing 5.3% by weight coal in methanol was burned at the same heat release rate as was the pure methanol flame. Fuel delivery problems discussed in Chapter II required replacing the original fuel nozzle with one of larger diameter. The result is a flame slightly longer and thinner. The difficultly in keeping the operating conditions constant throughout an experimental run made repeatability less satisfactory than for pure methanol.

1. Temperature composition

The temperature structure for the methanol/coal flame is shown in Figure IV-14. The squares are the radiation corrected temperatures and the dotted lines are the corresponding temperatures for the pure methanol flame. The effect of the larger diameter nozzle is evident at an axial position of 26.9 cm. The drop in temperature on the right side of the furnace is due to a decrease in mixing of the fuel jet with the secondary air. This is caused by larger diameter drops associated with the lower fuel pressure (2×10^5 N/m^2 as opposed to 5.4×10^5 N/m^2 for the smaller nozzle) and to a narrower spray cone angle which results from a decrease in fuel jet momentum. By a distance of 58.4 cm, the effect of the nozzle has diminished, and finally near the exit of the furnace, the difference in temperature profiles is minimal.

One is tempted to say that the flattening of the profiles in the Figures b) and c) and the large decrease in temperature in plot a) is due to the increased radiation of the coal particles. Particle radiation does account for some of the difference between profiles but since the thermocouple temperature measurements are only accurate to plus or minus

a) x = 26.9 cm

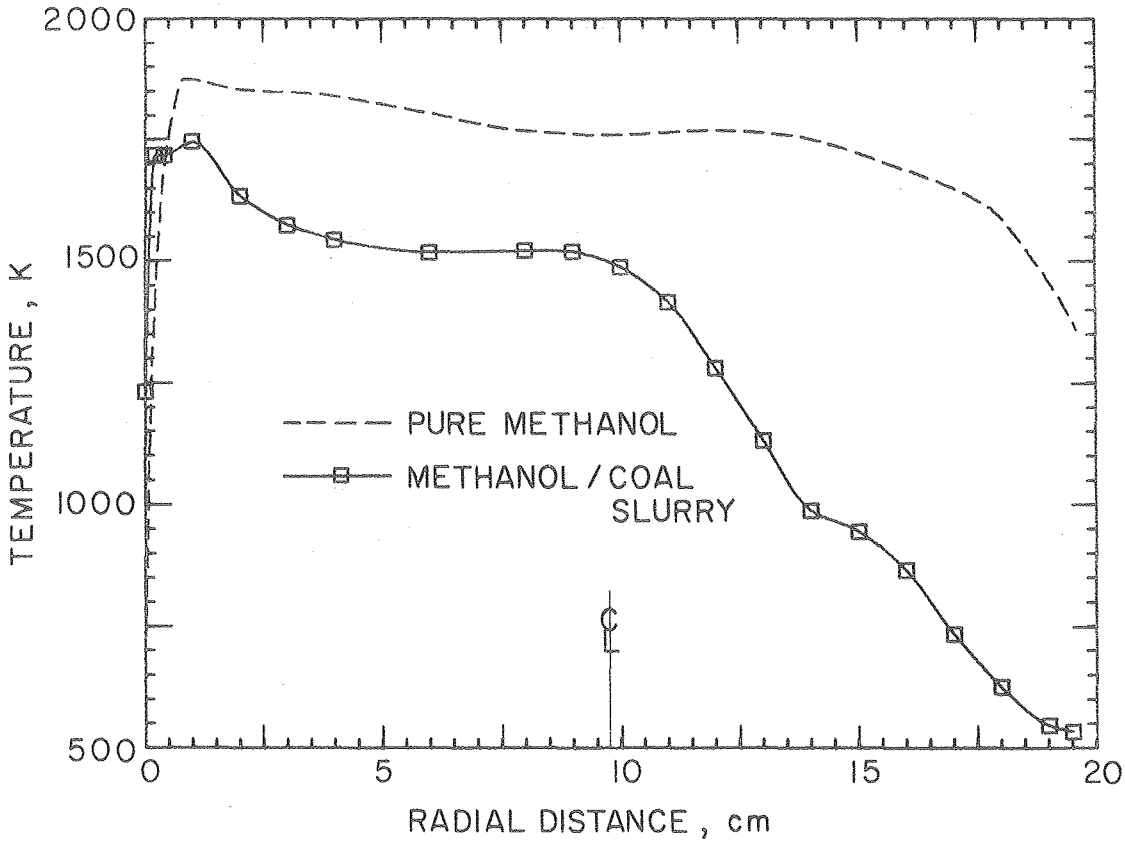

b) x = 58.4 cm

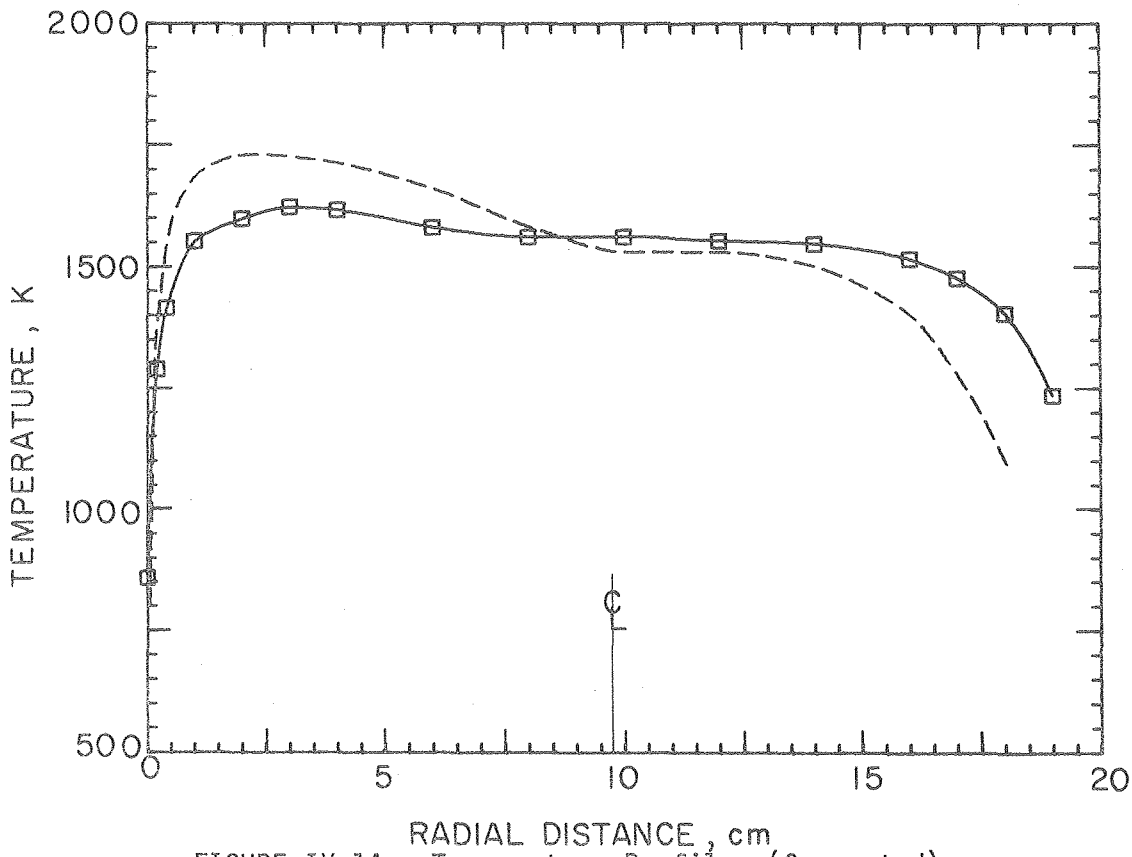

FIGURE IV-14. Temperature Profiles (Corrected) Comparing Slurry to Pure Methanol

c) x = 86.9 cm

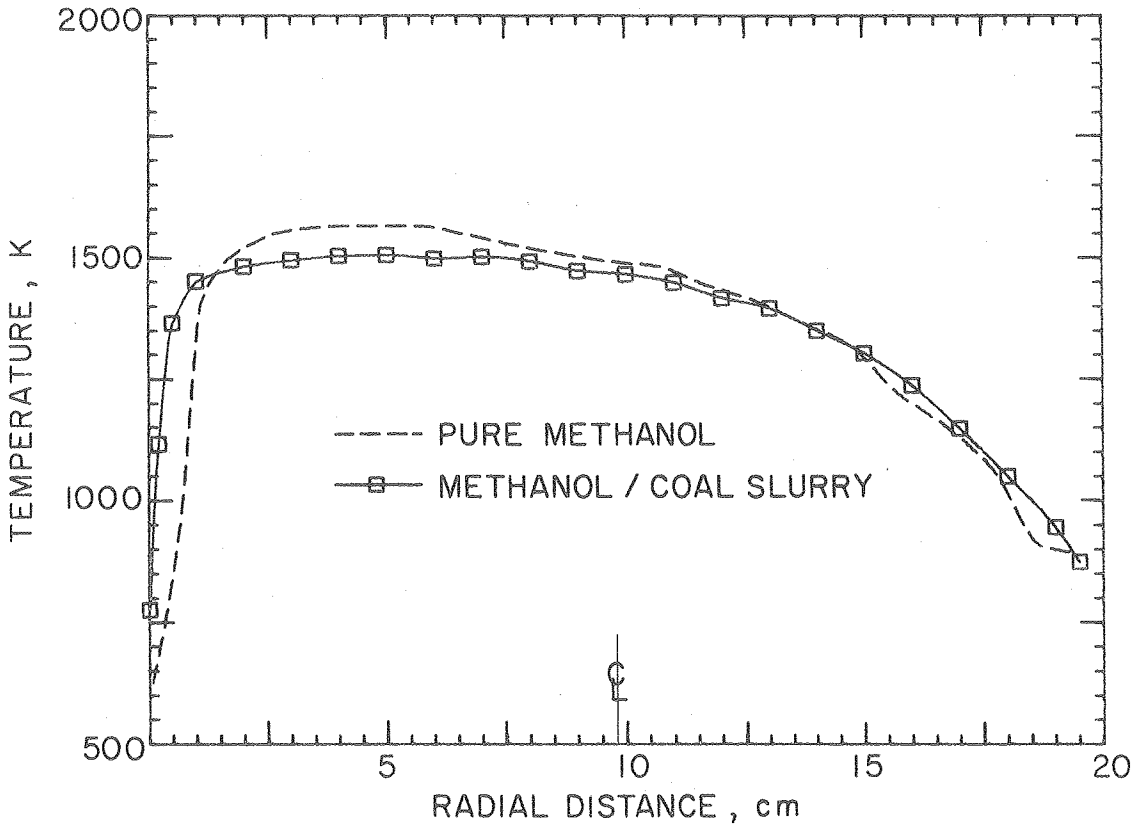

FIGURE IV-14. (continued)

about 20 K and since the nozzle variation may have a significant effect, a quantitative determination of particle effect is not possible.

2. Chemical composition

CO_2, NO, NX, and particulate levels were measured in the methanol/coal flame. Figure IV-15 contains plots of the CO_2 levels for the two flame conditions, the squares being the data for the slurry and the dotted lines the corresponding curves for the pure methanol. The former points are corrected for water concentration by assuming the water and carbon dioxide are in a two-to-one ratio. The difference is not striking. The gross effect seen in the temperature profile at an axial distance of 26.9 cm is not manifested in the carbon dioxide concentration profile.

The effect of small amounts of coal in the fuel is most noticeable on the nitric oxide concentration. Optimistically, one might reason that the NO levels should decrease with small amounts of coal because of increased radiation heat transfer from the flame zone and the accompanying decrease in temperature. However, inspection of Figure IV-16 shows that the optimism is not warranted. The NO measurements are indicated with squares and are at levels five to ten times that of the pure methanol flame. The NX levels also increase, but the NO percentage of the total NX is higher than before. The dotted lines on the curves are the NX levels for the pure methanol flame and are included for reference.

The reason for the marked increase in nitric oxide is the nitrogen which is bound in the fuel. The coal contains 1.5% nitrogen by weight which translates to about 200 ppm by volume if it is all converted to NO. The difference between the total NX in the two flames at the exit centerline is about 90 ppm and ranges between 40 ppm and 100 ppm throughout the remainder of the furnace. A conversion efficiency of the fuel nitrogen of

a) x = 26.9 cm

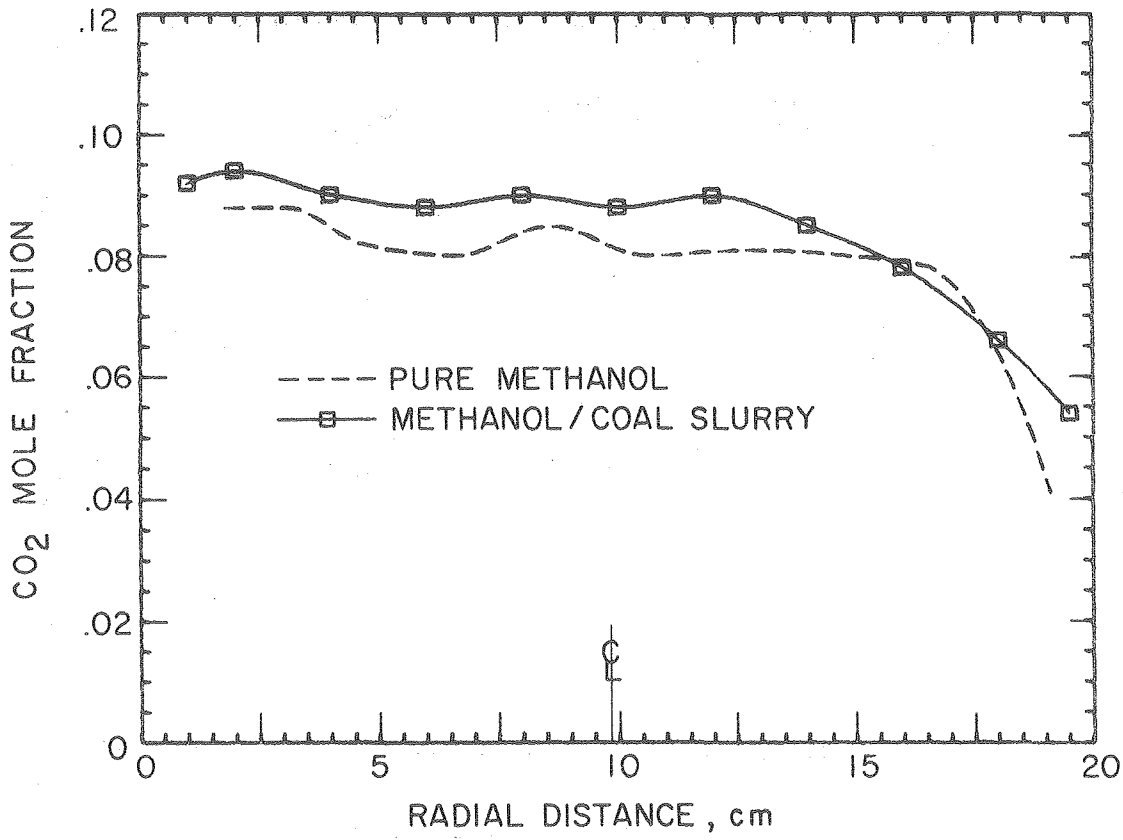

b) x = 58.4 cm

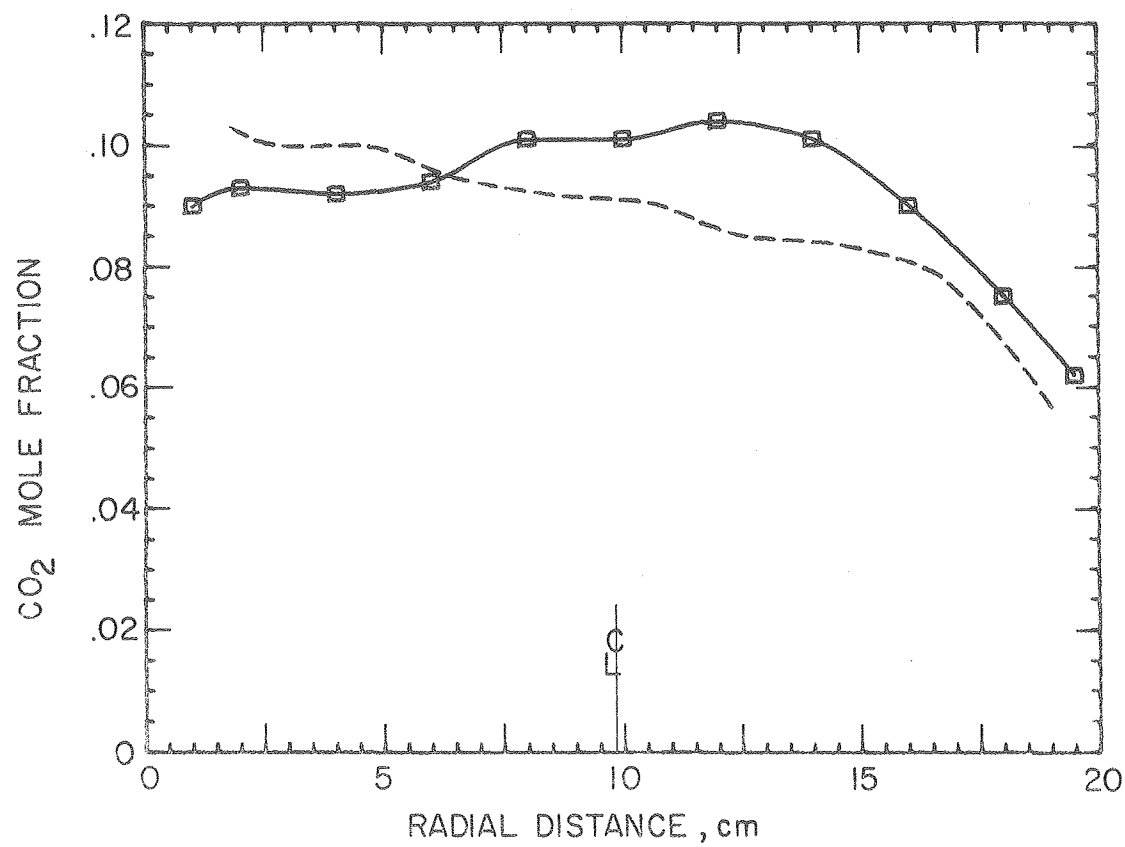

FIGURE IV-15. CO_2 Concentration Profiles Comparing Slurry to Pure Methanol

c) x = 86.9 cm

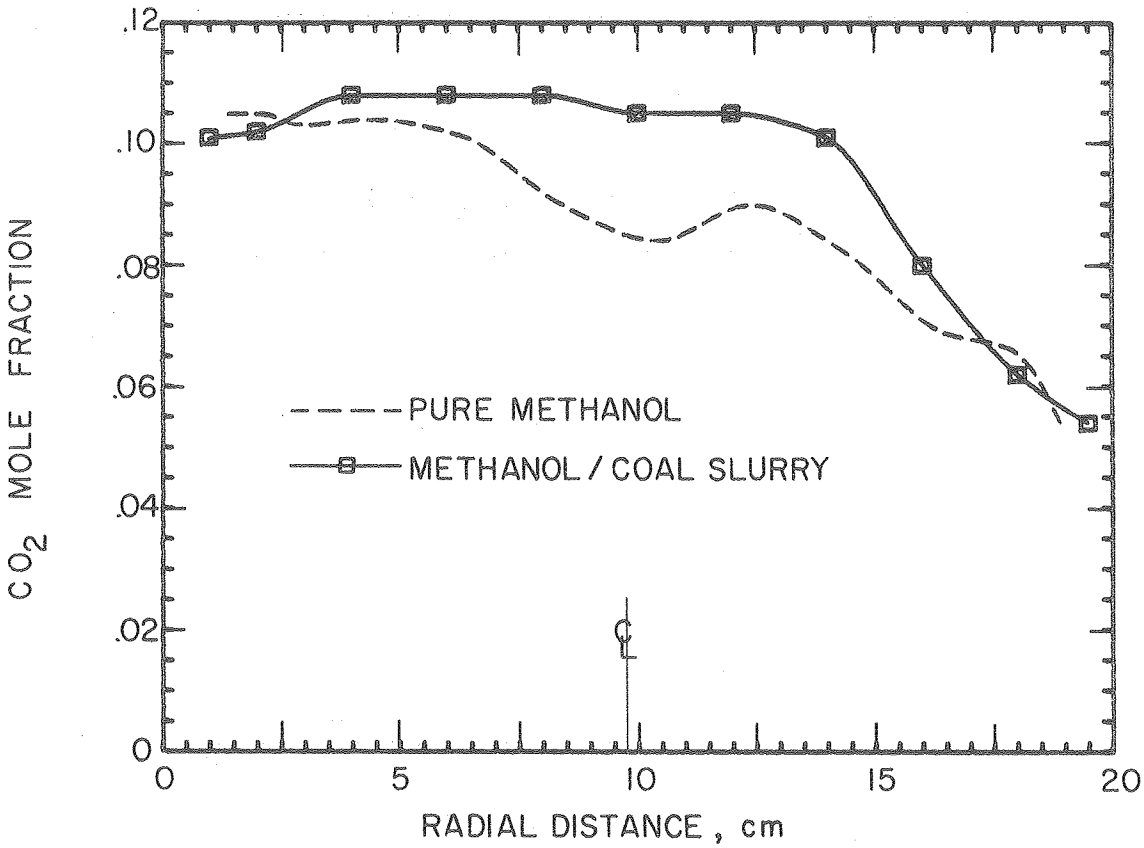

FIGURE IV-15. (continued)

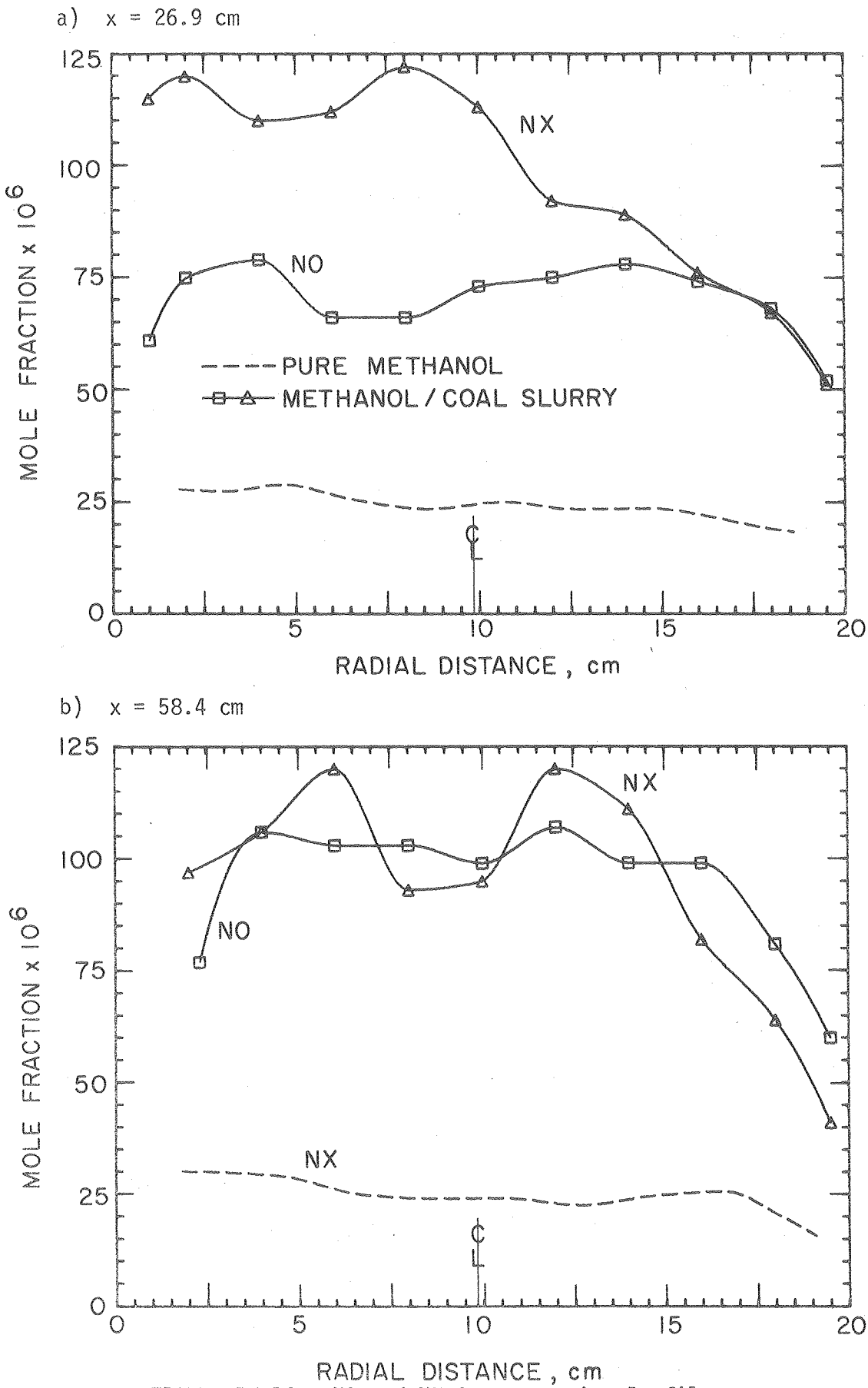

FIGURE IV-16. NO and NX Concentration Profiles With Slurry as Fuel

about 40% on the average is low according to other workers studying fuel nitrogen compounds in overall lean systems (Turner, Andrews and Siegmund, 1972).

In Figure IV-16b the total NX dips below the NO curve. This is an indication of the difficulty of obtaining the NX data for the methanol/coal slurry flame and is due to unavoidable variations in both the furnace and chemiluminescent operating conditions. For this reason, the NX data should not be taken quantitatively. On the other hand, the NO mode of the analyzer is much more stable, and as a result, the data should be reliable to 10% or so.

The particulate levels were measured for both flame conditions. Levels of the order of .001 g/m^3 were found in the pure methanol flame, while in the methanol/coal flame the levels were between .08 and .28 g/m^3. As a comparison, the incoming pulverized coal level is about 1.5 g/m^3 on the average, corrected to 1500 K. Figure IV-17 shows the variation of particulate concentration with axial and radial position. Except for a few points, the total particulate levels decrease with axial position. The abnormally high concentrations found near the wall at 86.9 cm are due to particulates which build-up on the wall and are then scrubbed off. It should be noted that the volume used in calculating the concentration is based upon the local density; this means that a soot cloud will decrease in concentration due to temperature increase even without a reduction in total soot mass.

Photographs taken with a light microscope at a magnification of 450x show the history of typical particles. In Figure IV-18 two categories of particles can be seen. The large spherical black ones are the unreacted coal particles. The very small particles are likely fly ash or soot particles which have agglomerated. The number of large particles decreases with increasing axial position as the coal is burned. The total number of small particles and the amount of agglomeration increases with axial position.

c) x = 86.9 cm

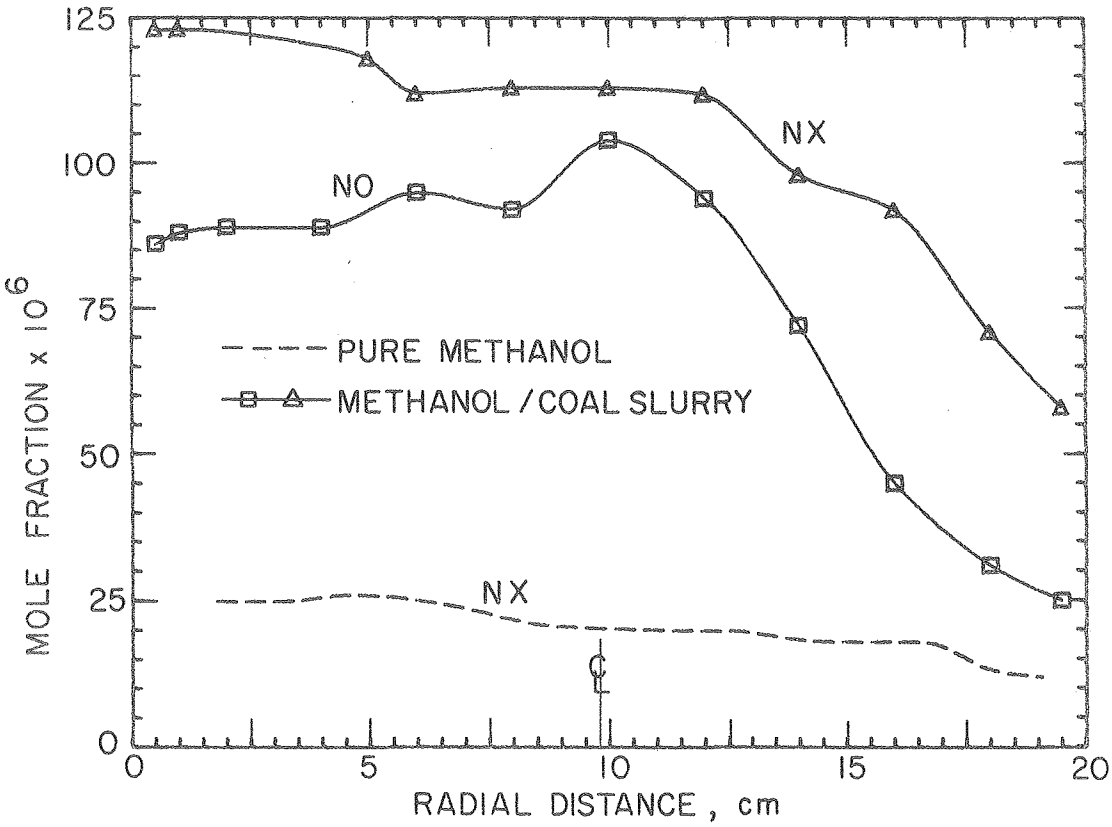

FIGURE IV-16. (continued)

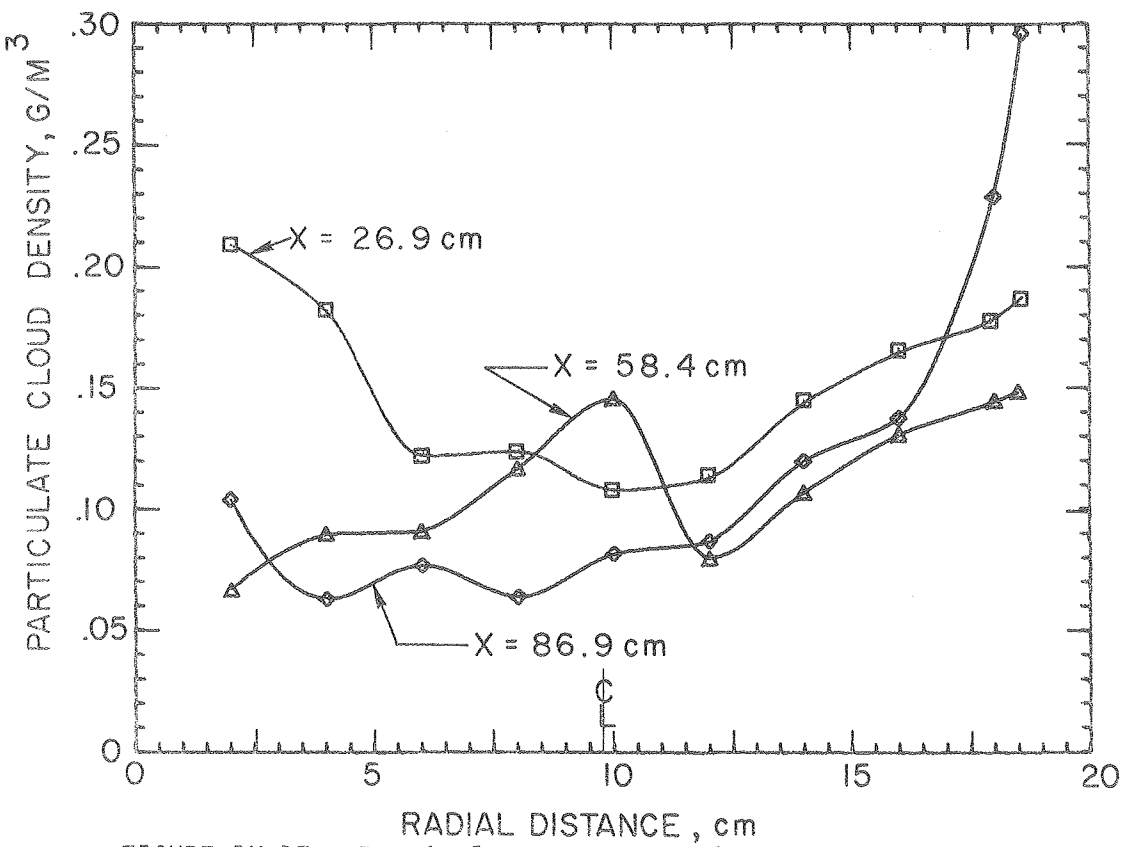

FIGURE IV-17. Particulate Concentration Profiles With Slurry as Fuel

a) x = 26.9 cm, y = 14.0 cm

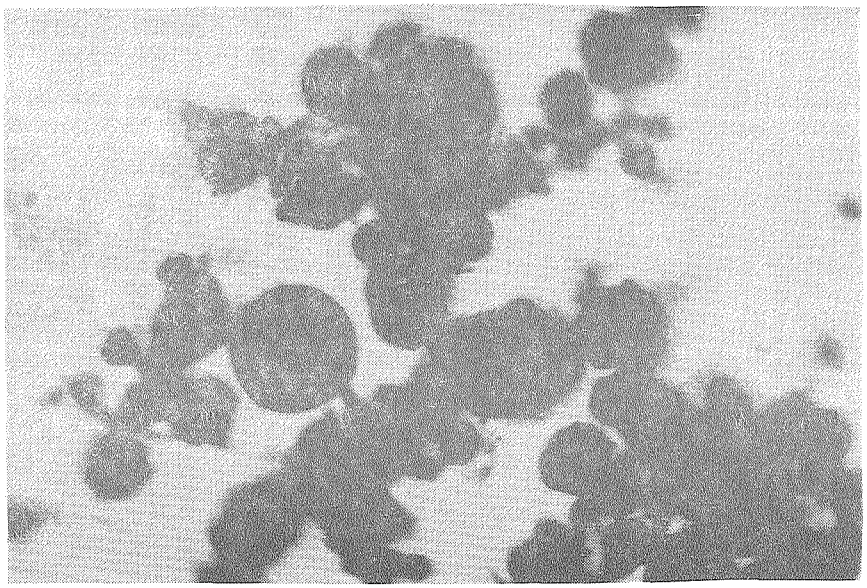

0 50 μm

b) x = 58.4 cm, y = 12.0 cm

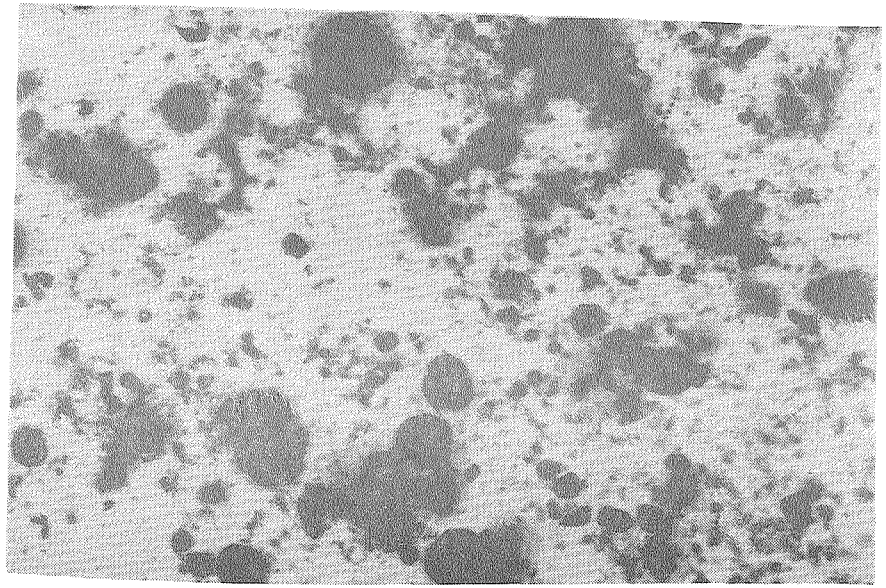

c) x = 86.9 cm, y = 12.0 cm

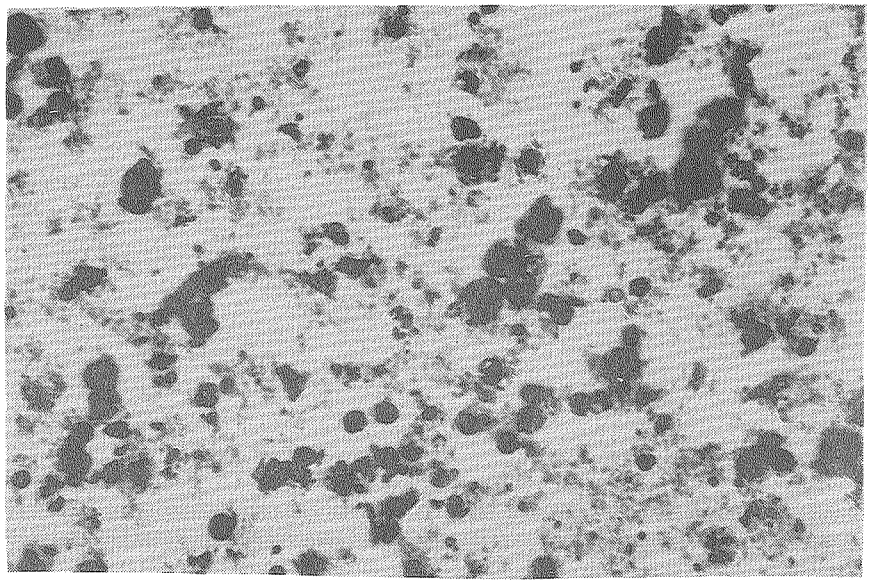

FIGURE IV-18. Particulates collected at Axial Position, x, and Radial Position, y, in a Methanol/5.3% Coal Flame (Magnification 450x)

V. MODELING OF RADIATION FROM FURNACE FLAMES

Physical processes occurring in realistic flame systems are inherently complex and interrelated. By necessity, modeling of such processes is often gross and artificial. But even the simplest model must be based on sound physical priciples. This chapter is intended to review the basic physical principles of infrared radiation and existing models for gaseous radiation. The model used in the present study is developed from this information (Grosshandler, 1976).

A. Fundamentals of Radiation

There is no attempt here to detail all the basics of infrared radiation theory. Interested readers are refered to books by Siegel and Howell (1972) and Hottel and Sarofim (1967) for complete treatment of the theory and applications of radiative transfer. C.L. Tien (1968) gives a comprehensive review of the radiative properties of gases in general; while Ludwig, Malkmus, Reardon and Thomson (1973) discuss predictive procedures for radiation from combustion gases in particular. An easily readable text by Barrow (1962) titled Molecular Spectroscopy gives a more detailed description of the chemical processes involved in radiation.

1. Radiation from surfaces

A fundamental equation in radiation transfer relating the total energy emitted by a blackbody to the fourth power of temperature was postulated by Stefan based upon experimental evidence in 1879 and later derived by

Boltzmann based upon thermodynamics. An attempt to explain the variation of intensity with wavelength of emitted energy from classical mechanics was unsuccessful by Rayleigh and Jeans around the turn of the century. Wien was able to develop a semiempirical law which predicted the spectral variation of intensity fairly successfully but it was not until Planck's introduction of the quantized nature of energy that the proper form of the energy distribution was established. (Tien and Lienhard, 1971, Chapter 4). The spectral intensity of radiation from a blackbody, $I_{\lambda b}$, as a function of temperature, T, and wavelength, λ, is given as

$$I_{\lambda b} = \frac{2\ C_1}{\lambda^5\ [\exp(C_2/\lambda T) - 1]}$$

where C_1 and C_2 are the first and second radiation constants defined in terms of Planck's constant, the speed of light, and Boltzmann's constant.

The value of λ which yields the maximum intensity can be found by differentiating $I_{\lambda b}$. This results in Wien's displacement law

$$\lambda_{max} = \frac{2898\ \mu m - K}{T}$$

No real object radiates exactly as a blackbody but as some fraction which is dependent upon both temperature and wavelength. This fraction is the emissivity of the object, ε_λ. In addition to temperature and wavelength, the emissivity can vary with the direction relative to the radiating surface. If an object is diffuse, there is no directional variation.

For an opaque object, radiation can interact two different ways with the surface. It can be absorbed or reflected. The fraction absorbed, α_λ, plus the fraction reflected, ρ_λ, must equal one. For a diffuse system in radiative equilibrium, α_λ equals ε_λ, so

$$\varepsilon_\lambda = 1 - \rho_\lambda$$

All materials have different reflectivities, the value of which can be

estimated by application of Maxwell's equations describing the interaction between electric and magnetic fields. From this theory, it can be shown that (Siegel and Howell, 1972, Chapter 4)

$$\rho'_{\lambda\,||} = \frac{(n_2 \cos\beta - n_1 \cos\chi)^2 + (\kappa_2 \cos\beta - \kappa_1 \cos\chi)^2}{(n_2 \cos\beta + n_1 \cos\chi)^2 + (\kappa_2 \cos\beta + \kappa_1 \cos\chi)^2}$$

$$\rho'_{\lambda\,\perp} = \frac{(n_2 \cos\chi - n_1 \cos\beta)^2 + (\kappa_2 \cos\chi - \kappa_1 \cos\beta)^2}{(n_2 \cos\chi + n_1 \cos\beta)^2 + (\kappa_2 \cos\chi + \kappa_1 \cos\beta)^2}$$

The prime on the reflectivities indicates that the value is direction dependent. (Electromagnetic theory can only predict specular properties; that is, it assumes that the angle of reflection is equal to the angle of incidence). The subscripts $||$ and $\perp$ indicate that the incident light is polarized either parallel or perpendicular to the incident plane. χ is the angle of refraction and is related to the incident angle, β, by

$$\frac{\sin\chi}{\sin\beta} = \left| \frac{n_1 - i\kappa_1}{n_2 - i\kappa_2} \right|$$

where $n - i\kappa$ is the complex refractive index of either the medium through which the wave is traveling (subscript 1) or the surface off which it is reflecting (subscript 2).

For unpolarized light,

$$\rho'_\lambda = \frac{\rho'_{\lambda\,||} + \rho'_{\lambda\,\perp}}{2}$$

To determine the hemispherical reflectivity, it is necessary to integrate ρ'_λ over all incident angles.

2. Radiation from particles

A beam of radiation traveling through a particle cloud can be absorbed and scattered. The importance of each of these phenomena is a strong function of the particle size, the optical properties, and

the angle of scatter relative to the incident beam.

These properties are embodied in the efficiency factor, X, and the phase function, Φ, of the particles. The efficiency factor is defined as the effective particle size for scatter or absorption relative to the geometrical cross section, A. The phase function accounts for radiation scattered preferentially into certain angles. An isotropic scatterer has a phase function equal to one.

For particles which are not too closely spaced (distance between centers > 3r), the effect of the individual particles can be summed over all particle sizes to determine the total extinction coefficient, K. K is made up of an absorption and scatter term, K_a and K_s.

$$K_a = \int_0^\infty N(r)\ A(r)\ X_a(r)\ dr$$

$$K_s = \int_0^\infty N(r)\ A(r)\ X_s(r)\ dr$$

where N(r) is the size distribution function for the particle cloud per unit volume.

In, principle, the efficiency factor can be determined by solution of Maxwell's equations for any particle size and shape. This was done by Mie for spherical particles and the results are summarized by Hottel and Sarofim (1967). For many engineering applications, it is useful to look at the limiting cases of these results.

One limit is obtained when the particle size is large compared to the wavelength of the radiation. The efficiency factors for scatter and absorption of a particle are just that of a large surface.

$$X_s = \rho_{\lambda_h}, \quad X_a = \varepsilon_{\lambda_h}$$

The h signifies that the hemispherical reflectivity is involved. The above relations are valid for both diffuse and specular reflectors. The phase functions differ for these two cases.

$$\Phi_s = \rho_{\lambda s} \left(\frac{\pi-\theta}{2}\right) / \rho_{\lambda h}$$

$$\Phi_d = \frac{8}{3\pi} (\sin\theta - \theta \cos\theta)$$

Since the reflectivity and absorptivity are independent of particle size, the total extinction coefficient for the cloud is

$$K = K_a + K_s = (\varepsilon_{\lambda h} + \rho_{\lambda h}) \tilde{A}$$

$\tilde{A}$ is the total projected area of the cloud per unit volume of cloud.

$$\tilde{A} = \int_0^\infty N(r)\, A(r)\, dr$$

The small particle limit is reached when the particle radius is much less than the wavelength. Rayleigh was the first to derive an expression for the scattering efficiency factor of a small non-absorbing particle with unpolarized incident radiation.

$$X_s = \frac{8}{3} \left(\frac{2\pi r}{\lambda}\right)^4 \left(\frac{n^2 - 1}{n^2 + 2}\right)^2$$

From the asymptotic solution to the Mie theory, allowing for absorption, the results are

$$X_s = \frac{8}{3} \left(\frac{2\pi r}{\lambda}\right)^4 \left|\frac{(n - i\kappa)^2 - 1}{(n - i\kappa)^2 + 2}\right|^2$$

$$X_a = 24 \left(\frac{2\pi r}{\lambda}\right) \frac{n\kappa}{(n^2-\kappa^2+2)^2 + 4n^2\kappa^2}$$

For the entire cloud, the respective scatter and absorption coefficients are

$$K_s = 24 \frac{\pi^3}{\lambda^4} \left| \frac{(n-i\kappa)^2 - 1}{(n-i\kappa)^2 + 2} \right|^2 \int_0^\infty N(r)\ V^2(r)\ dr$$

$$K_a = 36 \frac{\pi}{\lambda} \frac{n\kappa}{(n^2-\kappa^2+2)^2 + 4n^2\kappa^2} \int_0^\infty N(r)\ V(r)\ dr$$

The integral in the absorption coeffiecient is the particle volume per unit volume of cloud, $\tilde{V}$.

The phase function in the small particle limit is again independent of particle size and is expressed as

$$\Phi = \frac{3}{4} (1 + \cos^2\theta)$$

3. Radiation from gases

For the purpose of heat transfer calcultations, the scattering of radiation by gas molecules can be neglected relative to the absorption and emission process. The significant difference between gas absorption and absorption by a cloud of particles is the strong dependence upon wavelength of the gas absorption. The banded type structure of gaseous radiation is a result of the discrete energy levels at which the gas molecules exist.

Figure V-1 is a diagram showing the different energy levels of a diatomic gas molecule and three different types of energy transitions possible. The transition between two rotational energy levels within the same vibrational and electronic state involves the smallest change in energy, and since the energy is inversely related to the wavelength, involves the longest wavelength. The electronic transitions cause large changes in energy resulting in light being emitted or absorbed in the visible or ultra-violet. The rotational transitions involving two vibrational levels within one electronic state emit or absorb radiation

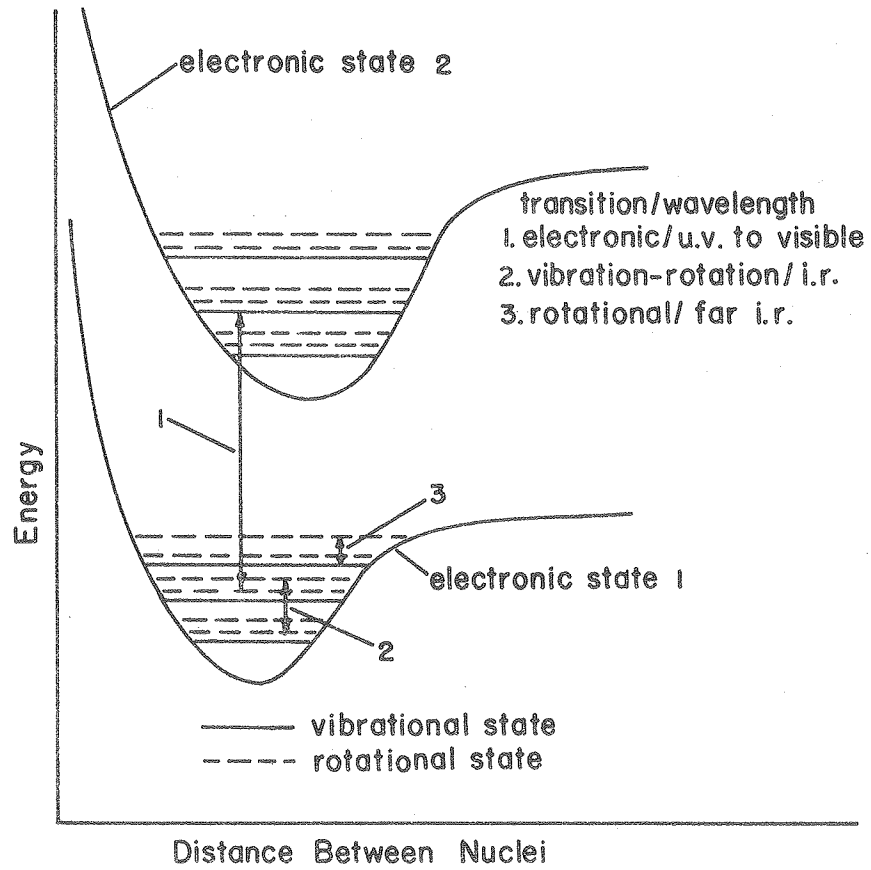

FIGURE V-1. Energy Transitions for a Diatomic Gas

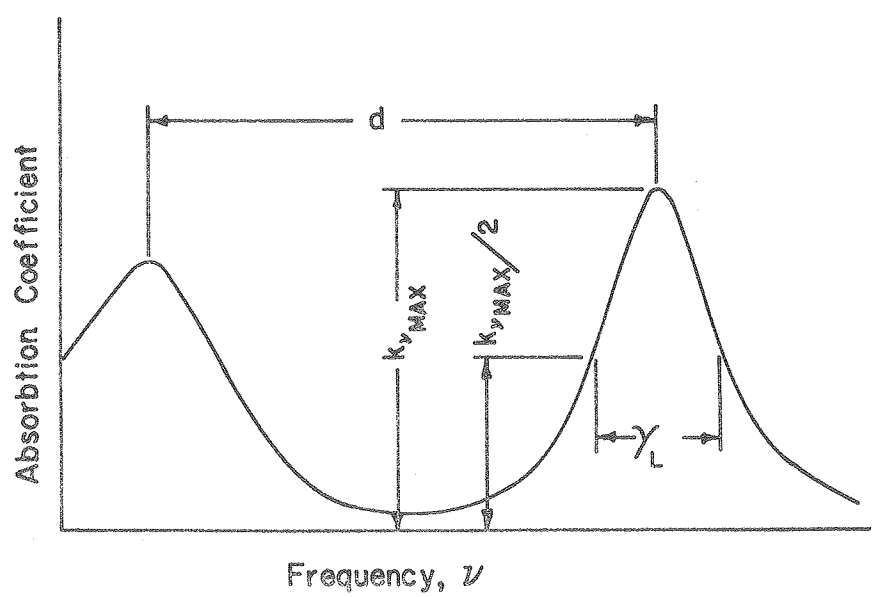

FIGURE V-2. Definition of Lorentz Profile Line Parameters

in the infrared. It is these last transitions that are of importance to thermal radiation.

In addition to a change in energy level, the other ingredient required for radiation is a change in dipole moment of the molecule. A dipole moment occurs if there is a net distribution of electrical charge which exists either permanently or instananeously within the molecule. The dipole moment can change during any of the transitions mentioned.

A monatomic gas cannot be infrared active since there is no vibrational or rotational structure, but it does exhibit an electronic spectra. Homonuclear diatomics such as N_2, O_2, and H_2 have no net dipole moment and so do not emit or absorb infrared energy either. Examples of gas molecules important in combustion systems which do radiate in the infrared are CO, OH, NO, H_2O, CO_2, NO_2 and CH_4.

The allowed energy levels for a rotating linear molecule (in ergs) can be determined from the Schrödinger equation to be (Barrow, 1962, p. 50)

$$e = hcBJ\ (J+1) \quad , J = 0, 1, 2...$$

$$B \equiv \frac{h}{8\pi^2 Ic}$$

The moment of inertia of the molecule about an axis perpendicular to molecular axis is I and the rotational quantum number is given by J. For a rigid rotator, I is a constant, and the frequency (sec^{-1}) for a transition of $\Delta J = \pm 1$ can be found by subtracting one energy level from the other.

$$\nu = \frac{\Delta e}{h} = 2cB\ (J+1)$$

This shows that the spectral lines for a rigid rotator are evenly spaced in frequency.

The quantum mechanical solution of a harmonic oscillator approximates a vibrating diatomic molecule well at low energy levels and is given by (Barrow, 1962, p. 37)

$$e = (\upsilon + \frac{1}{2}) \frac{h}{2\pi}\sqrt{\frac{k'}{\mu}} \quad \upsilon = 0, 1, 2...$$

where k' is the "spring constant" of the bond, μ is the reduced mass, and υ is the vibrational quantum level. The frequency of transition is

$$\nu_o = \frac{\Delta e}{h} = \frac{1}{2\pi}\sqrt{\frac{k'}{\mu}}$$

For real molecules which are neither rigid rotators or harmonic oscillators, the energy levels can be determined by a power series expansion in $J(J + 1)$ and $(\upsilon + 1/2)$ to get the following relation for the total rotational and vibrational energy:

$$e(\upsilon, J) = \nu_e(\upsilon + 1/2) - \nu_e x_e (\upsilon + 1/2)^2 + \nu_e y_e (\upsilon + 1/2)^3$$
$$+ \nu_e z_e (\upsilon + 1/2)^4 + hcB_e J(J + 1) - \alpha_e(\upsilon + 1/2) J(J + 1)$$
$$- D_e J^2 (J + 1)^2 + ...$$

ν_e is the value of the frequency if the vibration were harmonic and $D_e x_e$, $D_e y_e$, $\nu_e z_e$, α_e and D_e are constants. Selection rules which determine which transitions are allowable indicate that $\Delta J = \pm 1$, $\Delta\upsilon = \pm 1$, so that the frequency of transitions can be determined once the molecular constants are known. Data for many diatomics can be found in Herzberg (1950).

The likelihood of any particular transition taking place is a function of the number of molecules which are in the initial energy state. The Boltzmann distribution for the number of molecules in state i is

$$N_i = g_i N_o \exp [-(e_i - e_o)/k_o t]$$

where N_o is the number in the ground state, g_i is the degeneracy of the initial state ($g_i = 2J + 1$ for rotational energy levels), k_o is Boltzmann's constant, e_i and e_o are the initial and

ground energy levels, respectively and T is temperature. For a typical molecule at room temperature, less than 1% of all the molecules are in a vibrational state greater than $\upsilon = 0$; while a significant number of molecules can be in a rotational level as high as J = 40.

The transition frequencies for various vibrational and rotational levels are not precisely discrete quantities. The spectral lines are broadened by various physical processes. Application of Heisenberg's uncertainty principle to the energy levels involved results in natural line broadening. At any but the lowest pressures and temperatures, this effect is not a significant broadener when compared to other methods. In engineering applications, collision broadening is important and results in a line shaped with a Lorentz profile, i.e., the pressure absorption coefficient for the line is given as

$$k_\nu = \frac{S}{\pi} \frac{\gamma_L}{(\nu_o - \nu)^2 + \gamma_L{}^2}$$

$$S \equiv \int_0^\infty k_\nu d_\nu$$

where S is the integrated line strength or intensity, γ_L is the half-width of the collision broadened line, and ν_o is the line center frequency. These are defined in Figure V-2. Doppler broadening becomes predominent at higher temperatures and lower pressures and yields a line pressure absorption coeficient shaped like

$$k_\nu = \frac{S}{\gamma_D} \left(\frac{\ln 2}{\pi}\right)^{1/2} \exp\left[\frac{-(\nu_o - \nu)^2 \ln 2}{\gamma_D{}^2}\right]$$

where γ_D is the Doppler broadened line half-width. The collision and Doppler line half-widths vary with temperature, pressure, and ν_o.

$$\gamma_L \propto \left(\frac{P}{T}\right)^{1/2} \qquad \gamma_D \propto T^{1/2}\, \nu_o$$

The energy emitted from a uniform gas path of length ℓ can be written as

$$I_\nu = \int_0^\infty I_{b\nu} \left[1 - \exp\left(-K_\nu \ell\right)\right] d\nu$$

where $K_\nu = k_\nu P_i$, and P_i is the partial pressure of the absorbing gas. But since the line is very narrow, the blackbody intensity can be removed from the integral and approximated as a constant evaluated at the line center. The remaining integral is called the effective line width, W.

$$W \equiv \int_0^\infty \left[1 - \exp\left(-K_\nu \ell\right)\right] d\nu$$

This integral can be easily evaluated for the two limiting cases of optical depth ($K_\nu \ell$). For large $K_\nu \ell$ (strong line limit) and a Lorentz line profile

$$W \simeq 2\gamma_L^{1/2} \left(S\ell\right)^{1/2}$$

while for small $K_\nu \ell$ (weak line limit)

$$W \simeq S\ell$$

The general solution for W with a Doppler profile is a series of the form

$$W = S\ell \sum_{n=0}^{\infty} \left[\frac{S\ell}{\gamma_D}\left(\frac{\ln 2}{\pi}\right)^{1/2}\right]^n \Big/ \left[(n+1)!\ (n+1)^{1/2}\right]$$

All of the rotational transitions which occur for one particular vibrational transition are said to make up a band. The absorption of a band is a function of the individual line intensity and the spacing between lines. For any but the simplest band at low pressures and temperatures, a line by line summation of intensity is tedious, if not unrealistic. As an example, the details of a diatomic vibration-rotation bond will be presented based upon Malkmus and Thomson (1961). Using their notation, ω is the wave number ($\omega = \nu/c$, cm^{-1}). The frequency of transition

for an anharmonic non-rigid rotator can be written in terms of w.

$$\omega = \omega_\upsilon + B_e\,[J'(J'+1) - J(J+1)]$$

$$-\alpha_e\,[(\upsilon + 3/2)\,J(J+1) - (\upsilon + 1/2)\,J(J+1)],$$

where

$$\omega_\upsilon = \omega_e - 2(\upsilon+1)\,\omega_e x_e + [3(\upsilon+1)^2 + 1/4]\,\omega_e y_e + [4(\upsilon+1)^3 + (\upsilon+1)]\,\omega_e z_e$$

Substitute $m = J + 1$ for the R-branch ($\Delta J = +1$) and $m = -J$ for the P-branch ($\Delta J = -1$) to get a quadratic equation in m.

$$\omega(m) = \omega_\upsilon + 2B_e m - \alpha_e\,[m(m+1) + 2(\upsilon + 1/2)\,m]$$

or

$$m(\omega) = \frac{B_e - \alpha_e(\upsilon+1) \mp \sqrt{[B_e - \alpha_e(\upsilon+1)]^2 - \alpha_e(\omega - \omega_\nu)}}{\alpha_e}$$

For non-overlapping bands, the total band intensity, $\alpha_\upsilon^{\upsilon+1}$, can be found by summing the individual line intensities

$$\alpha_\upsilon^{\upsilon+1} = \sum_{J,\ J \mp 1} S_{\upsilon,J}^{\upsilon+1,\ J\mp 1}$$

An expression for the individual line intensities can then be written based upon Penner (1954)

$$S_{\upsilon,J}^{\upsilon+1,\ J\mp 1} = \alpha_\upsilon^{\upsilon+1}\, B_e \frac{hc}{k_o T} \frac{\omega}{\bar{\omega}_\upsilon^{\upsilon+1}}\, m^{+} \exp\left[-\frac{hc}{k_o T}\frac{[B_e - \alpha_e(\upsilon+1)]}{\alpha_e}\right.$$

$$\left. \times \left\{2[B_e - \alpha_e(\upsilon+1)]\, m^{\mp} - \left[1 + \frac{\alpha_{e/2}}{B_e - \alpha_e(\upsilon+1)}\right](\omega - \omega_\upsilon)\right\}\right]$$

$$\times\ (1 + Cm^{\mp})\left[1 - \exp\left(-\omega\frac{hc}{k_o T}\right)\right]$$

The term C is the ratio of the zeroth to the first order term in the expansion of the electric dipole moment, and

$$\bar{\omega}_\upsilon^{\upsilon+1} = \omega_\upsilon\left[1 - \exp\left(-\omega_\upsilon \frac{hc}{k_o T}\right)\right]$$

The + or - sign corresponds to the P or R branches of the band.

The total band intensity is usually determined at one temperature. To account for variations with temperature, use

$$\alpha_{\upsilon}^{\upsilon+1}(T) = \alpha_{\upsilon}^{\upsilon+1}(T_o)\,\frac{\overline{\omega}_o'(T)\;\omega_{\upsilon}^{\upsilon+1}(T)}{\overline{\omega}_o'(T_o)\,\overline{\omega}_{\upsilon}^{\upsilon+1}(T_o)}\;\exp\left[(\omega_{\upsilon} - \omega_o)\,\frac{hc}{k_o}\left(\frac{1}{T_o} - \frac{1}{T}\right)\right]$$

The average line spacing, $d_{\upsilon}(w)$, can be written as

$$d_{\upsilon}(\omega) = 2\sqrt{[B_e - \alpha_e(\upsilon + 1)]^2 - \alpha_e(\omega - \omega_{\upsilon})}$$

4. The equation of transfer

Let radiation of spectral intensity I_{λ} be incident upon a differential volume at a position ℓ. The intensity of the radiation leaving the volume at $\ell + d\ell$ will depend upon the absorption, emission and scattering within the volume (see Figure V-3). The reduction in intensity due to absorption is $I_{\lambda}(\ell)K_a d\ell$. The increase due to emission is $I_{b\lambda}K_a d\ell$. Similarly, the intensity scattered out of the volume is $I_{\lambda}(\ell)K_s d\ell$. To account for radiation scattered into the volume which adds to the intensity, integrate over all solid angles and allow for preferential scattering.

$$I_{\text{scattered in}}\; d\ell = \frac{K_s}{4\pi}\, d\ell \int_{\Omega_i} I_{\lambda}(\ell, \Omega_i)\;\Phi(\Omega, \Omega_i)\, d\,\Omega_i$$

where Ω is the solid angle. Performing an energy balance on the volume results in

$$I_{\lambda}(\ell + d\ell) = I_{\lambda}(\ell) - I_{\lambda}(\ell)K_a d\ell + I_{b\lambda}(\ell)K_a d\ell$$
$$- K_s I_{\lambda}(\ell)d\ell + \frac{K_s}{4\pi}\int_{\Omega_i} I_{\lambda}(\ell, \Omega_i)\;\Phi(\Omega, \Omega_i)\, d\,\Omega_i$$

Rearranging,

$$\frac{dI_{\lambda}}{d\ell} = -\,(K_a + K_s)\;I_{\lambda} + K_a I_{b\lambda} + \frac{K_s}{4\pi}\int_{\Omega_i} I_{\lambda}(\Omega_i)\;\Phi(\Omega, \Omega_i)\, d\,\Omega_i$$

This equation can be integrated after multiplying by the transmittance $\tau_\lambda \equiv \exp\left[-\int (K_a + K_s)\, d\ell\right]$.

$$I_\lambda = I_{\lambda o}\tau_\lambda(o, \ell) + \int_o^\ell \left[K_a I_{b\lambda} + \frac{K_s}{4\pi}\int I_\lambda \Phi d\Omega\right] \tau_\lambda(\ell', \ell) d\ell'$$

This is the general and complete form of the integrated equation of transfer. Formulation of the parameters K_a, K_s, and Φ were discussed in previous sections so, at least in theory, I_λ can be determined along the path from 0 to ℓ.

For realistic engineering computations, the complete equation is rarely solved. A great simplification occurs if scattering is unimportant relative to absorption. For a gaseous system, this is always the case. When particles are present, if the diameter is in the Rayleigh scattering limit, the scattering coefficient relative to the absorption coefficient is proportional to the particle diameter over the wavelength, the whole quantity cubed. Since, in this limit, d/λ is already much less than one, the scattering is negligible relative to the absorption.

In the large particle limit $(K_s/K_a) = (\rho/\varepsilon)$. For coal and soot particles, which are of interest in furnace radiation, the emissivity is at least four times the reflectivity. Neglecting K_s should be, therefore, a reasonable assumption.

For medium size particles, it is not as obvious that scatter is less important than absorption, but for simplicity, this is also assumed for the furnace radiation problem. With these assumptions made, the final form of the integrated equation of transfer is

$$I_\lambda = I_{\lambda o}\tau_\lambda(o, \ell) + \int_o^\ell I_{\lambda b}(\ell') \frac{\partial}{\partial \ell'}\tau_\lambda(\ell', \ell) d\ell'$$

B. Calculation of Radiation Properties

1. Particle radiation

To evaluate the effect of particles on the intensity of the furnace flame, the information which is required is the complex index of refraction and the size frequency distribution of the particles.

Foster and Howarth (1968) have determined the indices of refraction for various carbons and coals. Their specimen number 2 is close to the coal used in the furnace. In the range of interest, between a wavelength of one and six microns, $n \simeq 1.6$ and $\kappa \simeq .3$. From Dalzell and Sarofim (1969), the optical properties of propane soot are $n \simeq 2.4$ and $\kappa \simeq 1.4$. If it is assumed that the coal particle radiation is much more important than the soot radiation, then the data of Foster and Howarth is appropriate.

Using the relations in section A-1., the directional reflectivity can be found, and an estimate of the coal particle emissivity can be made.

$$\varepsilon_{coal} \simeq .88$$

Many frequency distribution functions are of the form

$$F_o(r)\, dr = a_o\, r^{b_o}\, e^{-c_o r}\, dr$$

To approximate $F_o(r)$, data from Milne, Greene and Beachey (1974) for pulverized coal was fit to the above form with $b_o = 1$. Their size distribution should be representative of the coal used in this study since both were prepared by the Bureau of Mines using similar coal and grinding techniques. The result is $a_o = 1.722 \times 10^7$ and $c_o = 4150$ with r in cm.

Since the coal particles will decrease in radius as they pass through the flame, some technique must be used to allow for the change in size frequency distribution. The initial particle load per unit volume of inlet gas, $\tilde{W}_o(g/cm^3)$, is known. The value of $\tilde{W}$ at various locations throughout the furnace is measured. Steady-state studies of burning droplets show that

the surface area of the droplets decreases linearly with time. If it is assumed that the decrease in particle loading is a measure of the time that the coal has been in the flame zone, then it is proposed that

$$4\pi \int_0^\infty F(r)r^2dr = \frac{\tilde{W}}{\tilde{W}_o} 4\pi \int_0^\infty F_o(r)r^2dr$$

where $F_o(r)dr$ is the initial size frequency distribution. Inserting the value for $F_o(r)$, solve for $F(r)$ and get

$$F(r) = a_o r \exp\left[- c_o\left(\frac{\tilde{W}_o}{\tilde{W}} \frac{T_o}{T}\right)^{1/2}\right]$$

The temperature ratio in the exponent is required to allow for simple changes in density which will effect the value of the particle loading.

The absorption coefficient requires evaluation of $N(r)$, the size frequency distribution per unit volume. The volume of gas is determined by multiplying the total particle volume by the particle density and dividing by the particle load per unit volume, $\tilde{W}$.

$$N(r) = \frac{F(r)}{\frac{\rho_{coal}}{\tilde{W}} \int_0^\infty \frac{4}{3}\pi\, r^3F(r)dr}$$

Define $\tilde{V}$ and recall the definition of $\tilde{A}$ for spherical particles

$$\tilde{V}(r^*) \equiv \int_0^{r^*} N(r)V(r)dr = \frac{\tilde{W}}{\rho_{coal}} \frac{\int_0^{r^*} r^3F(r)dr}{\int_0^\infty r^3F(r)dr}$$

$$\tilde{A}(r^*) \equiv \int_{r^*}^\infty N(r)A(r)dr = \frac{3}{4} \frac{\tilde{W}}{\rho_{coal}} \frac{\int_{r^*}^\infty r^2F(r)dr}{\int_0^\infty r^3F(r)dr}$$

The absorption coefficient can be approximated in the small and large particle limit by

$$K_a = \frac{36}{\lambda} \frac{n\kappa}{(n^2 - \kappa^2 + 2)^2 + 4n^2\kappa^2} \tilde{V}(r^*) + \varepsilon_{coal} \tilde{A}(r^*)$$

The meaning of r* is that value of radius such that the small and large particle limits predict the same value for K_a, which in this case is

$$\frac{2\pi r^*}{\lambda} = 1.2$$

$\tilde{A}$ and $\tilde{V}$ can be integrated exactly to

$$\tilde{V} = \frac{\tilde{W}}{\rho_{coal}} \left\{ 1 - e^{-cr^*} \left[\frac{(cr^*)^4}{24} + \frac{(cr^*)^3}{6} + \frac{(cr^*)^2}{2} + cr^* + 1 \right] \right\}$$

$$\tilde{A} = \frac{3}{16} \frac{\tilde{W}}{\rho_{coal}} \; c\, e^{-cr^*} \left[\frac{(cr^*)^3}{6} + \frac{(cr^*)^2}{2} + cr^* + 1 \right]$$

where $c \equiv c_o \left(\frac{\tilde{W}_o}{\tilde{W}} \frac{T_o}{T} \right)^{1/2}$

2. Gas radiation

To calculate the intensity of radiation from a gas cloud, three questions must be answered: what are the absorption properties of the individual lines of the different species, how can these be summed up over an entire band, and how can non-homogeneous effects be accounted for?

The gaseous species which are expected to be important in this study are listed in Table V. The fundamental transition of CO at 4.67 μm is much stronger than its first harmonic. For CO_2 the bending vibration which occurs at 15 μm is important at lower temperatures, but, because of the Planck distribution of energy, at typical flame temperatures the assymmetric stretching mode at 4.26 μm and the combination band at 2.7 μm are the only bands that need to be considered. The two bands around

TABLE V. VIBRATIONAL SPECTRA DATA

Molecule	Wavelength	Transition	Mode
CO	4.67 μm	v=1 to 0	Fundamental
	2.35 μm	v=2 to 0	1st Harmonic
CO_2	15.0 μm	01^10 to 00^00	Bend
	4.26 μm	00^01 to 00^00	Asymmetric Stretch
	2.70 μm	02^01 and 10^01 to 00^00	Combination Bend and Stretch
H_2O	6.27 μm	010 to 000	OH Bend
	2.70 μm	100 and 001 to 000	OH Symmetric and Asymmetric Stretch
	1.88 μm	011 to 000	Bend and Stretch
	1.38 μm	101 to 000	Symmetric and Asymmetric Stretch
CH_3OH	9.67 μm	v_4=1 to 0	C-O Stretch
	3.52 μm	v_2=1 to 0	C-H Stretch
	3.36 μm	v_5=1 to 0	C-H Bend
	2.72 μm	v_1=1 to 0	O-H Stretch

2.7 μm and at 6.27 μm are the largest contributors to the H_2O radiation. Some effect is also due to the 1.88 and 1.38 μm bands. The strongest methanol vibration occurs at 9.67 μm; however, the Planck distribution at flame temperatures biases the radiation towards the weaker 3.52 and 3.36 μm C-H stretching and bending. The 2.72 μm O-H stretching vibration is unimportant when compared to the contribution at that wavelength from CO_2 and H_2O.

In section A of this chapter, the absorption properties of individual lines of molecules such as these was discussed and an example of a diatomic molecule was given. This is applicable directly to the fundamental vibration of carbon monoxide. The assymmetric stretch mode of carbon dioxide can also be approximated as an equivalent diatomic oscillator. Details of this are given by Malkmus (J. Opt. Soc. Am., 1963). The 2.7 μm band of CO_2 cannot be approximated as a simple diatomic vibrator, though, since this band is the result of a combination of all the normal vibration modes. Malkmus (General Dynamics, 1963) discusses how the diatomic approximation can be extended with emipirical correlations to treat this band effectively. The absorption properties of water lines cannot be predicted in any tractable manner based upon the fundamental quantum and satistical mechanics, so it becomes more fruitful to use tabulated experimental results for the bands and not worry about the contribution from individual lines. For a non-linear six atom molecule like CH_3OH, no data are available for the absorption coefficients, and any approach to predict them from fundamental physics would be extremely cumbersome. Fortunately, in the furnace flame, large concentrations of methanol are confined to the cooler central core at the furnace entrance and do not contribute significantly to the total radiation. Therefore, methanol, along with trace species such as NO, NO_2 and HCHO, is neglected in the radiation calculations.

If there were no overlapping lines within an individual band the total absorption properties would simply be due to the single lines. In general, there is always overlap of lines due to neighboring rotational lines of the same branch, overlap of lines from the other branch, and overlap of lines from different vibration transitions (i.e. $\upsilon = 0 \rightarrow \upsilon = 1$, $\upsilon = 1 \rightarrow \upsilon = 2$). Depending on the molecule and band, different approximations are used to sum up the effect of all lines at a given wavelength.

One of the simplest techniques is the Elsasser model which assumes that the total absorption coefficient at any frequency is made up of contributions from lines which are evenly spaced and all of the same intensity and half-width. If a Lorentz line profile is used, the pressure absorption coefficient ($atm^{-1}cm^{-1}$) can be written as

$$k_\omega = \sum_{i=-\infty}^{\infty} \frac{S(\omega)}{\pi} \frac{\gamma_L(\omega)}{[\omega - id(\omega)]^2 + \gamma_L(\omega)}$$

where $\gamma_L(\omega)$ and $d(\omega)$ are the Lorentz line half-width and the line spacing, respectively. The series can be summed exactly to

$$k_\omega = \frac{S}{d} \frac{\sinh\left(\frac{2\pi\gamma_L}{d}\right)}{\cosh\left(\frac{2\pi\gamma_L}{d}\right) - \cos\left(\frac{2\pi\omega}{d}\right)}$$

The ω dependence of S, d, and γ_L has been dropped to simplify notation, but it is implied throughout the remainder of this discussion.

For a polyatomic molecule at higher temperatures, the approximations of the Elsasser model are not valid. Goody(1964) has devised a better model under these conditions which assumes that the lines are randomly spaced and of an exponential distribution in intensity. With the Lorentz line half-width assumed constant, the result is

$$k_\omega = \frac{S_E/d_E}{\left(1 + \frac{S_E P_i \ell}{4\gamma_L}\right)^{1/2}}$$

where the "E" subscript denotes average values over a small wave number interval and ℓ is the path length.

In addition to the above two models, there are ones which incorporate a Doppler line shape, ones which contain a combination of line shapes, and ones which combine elements of the random and evenly spaced line assumption. These are discussed in Goody (1964) and Ludwig, et al. (1973).

The optical depth is defined as

$$X \equiv \int_0^L k_w P_i d\ell$$

With this definition, the transmittance becomes $\tau = e^{-X}$. For the optically thin (or weak line) limit, both the Elsasser and Goody models become (for a homogeneous path)

$$\tau_{weak} \rightarrow \exp\left(-\frac{S}{d} P_i \ell\right)$$

The Elsasser and Goody strong line limits, also for a homogeneous path, become respectively

$$\tau_{Elsasser,\ strong} \rightarrow \mathrm{erfc}\left[\frac{(\pi\gamma_L P_i \ell S)^{1/2}}{d}\right]$$

$$\tau_{Goody,\ strong} \rightarrow \exp\left[-\frac{(\pi\gamma_L P_i \ell S)^{1/2}}{d}\right]$$

For vibrational bands such as the CO fundamental and the 2.7 and 4.26 μm bands of CO_2, some form of the diatomic rotating oscillator approximation can be used to determine the strengths of the individual lines of the P and R branches as discussed earlier. These can then be summed rigorously over both branches and all significant vibrational levels to

get the total pressure absorption coefficient or transmittance in any particular wave number interval. In the weak line limit, the result is

$$\overline{\tau}_{weak} = \exp\left[-\frac{\overline{S}}{d} P_i \ell\right]$$

where the bar indicates averages over a small wave number interval and

$$\frac{\overline{S}}{d} \equiv \sum_{\upsilon=0}^{\infty} \left(\frac{S_{\upsilon,\,J}^{\upsilon+1,\,J+1} + S_{\upsilon,\,J}^{\upsilon+1,\,J-1}}{d_\upsilon} \right)$$

The parameters in the above equation were defined for a diatomic oscillator earlier in the chapter. $(\overline{S/d})$ is termed the mean absorption coefficient since it becomes identical to k_ω in the weak limit. The strong line limit yields the following value for $\overline{\tau}$

$$\overline{\tau}_{strong} = \exp\left[-2\gamma_L P_i \ell \left(\overline{\frac{S}{d}}^{1/2}\right)\right]$$

with

$$\left(\overline{\frac{S}{d}}^{1/2}\right) = \sum_{\upsilon=0}^{\infty} \left[\frac{\left(S_{\upsilon,\,J}^{\upsilon+1,\,J+1}\right)^{1/2} + \left(S_{\upsilon,\,J}^{\upsilon+1,\,J-1}\right)^{1/2}}{d_\upsilon} \right]$$

$(\overline{S^{1/2}/d})$ is called the mean strong-line parameter.

If the optical path were homogeneous or in the optically thick or thin limits, the calculation of the radiant intensity would be straight forward once the spectroscopic parameters of the gas were known. In the furnace, the path is far from being homogeneous. To account for this, a technique called the Curtis-Godson approximation is used to calculate the optical depth of the gas. Basically, what this approximation does is replace the inhomogeneous path with an equivalent homogeneous path which results in the exact solution for both the weak and strong absorption limits.

$$X_{C-G} = \frac{X_{weak}}{\left(1 + \frac{X_{weak}}{4a}\right)^{1/2}}$$

where

$$X_{weak} \equiv \int_0^L \left(\frac{\bar{S}}{d}\right) P_i \, d\ell$$

$$a \equiv \frac{1}{X_{weak}} \int_0^L \frac{\gamma_L}{d} \left(\frac{\bar{S}}{d}\right) P_i \, d\ell$$

That is, X_{weak} is the total optical depth which would result if the path were optically thin between o and L; and a is the line thickness to spacing ratio averaged over the optically thin path. It can be easily shown that this approximation yields the same value for transmittance, as is given on the previous page, if the path is truly homogenous.

The Lorentz line-width, γ_L, is often tabulated for mixtures of the radiating gas with nitrogen at 273 K. To account for temperature and for different line broadening effects by molecules other than nitrogen, γ_L should be modified as follows:

$$\gamma_L = \sum_{j=1}^{n} \gamma_{L_j} \, P_j \left(\frac{273}{T}\right)^{\eta_j}$$

where m_j is the broadening parameter for species J interacting with the species of interest.

C. Computational Procedure for Integration of Equation of Transfer

With the optical properties of the combustion constituents calculated and the temperatures and partial pressures across the line of sight known, the spectral and total intensity can be determined by integration of the equation of transfer. With scattering neglected, the equation can be written

$$I_\lambda = I_{\lambda_L} \, \tau_\lambda(0,L) - \int_0^L I_{b_\lambda}(\ell) \, \frac{d\tau_\lambda(\ell)}{d\ell} \, d\ell$$

where $\tau_\lambda(\ell) = \exp\,[-\,\Sigma X_\lambda(\ell)]$. For the gaseous species, X_λ is the optical depth using the Curtis-Godson approximation between o and ℓ. For particulates,

$$X_\lambda = \int_o^\ell K_a d\ell'$$

If the intervals are taken sufficiently small, the integral can be put in the form of a sum. Also, since the walls of the furnace are cold, neglect the radiant intensity leaving the far wall at L.

$$I_\lambda \simeq \sum_{m=1}^{M} \left[I_{b_\lambda}(m) \left(\tau_{\lambda_m} - \tau_{\lambda_{m-1}} \right) \right]$$

M is the total number of intervals across the furnace. It is important that the distance intervals be small enough such that inhomogeneous effects are negligible across each individual interval.

To determine the total intensity at any given axial position along the furnace, the spectral intensity is numerically summed over the wavelength range of interest, usually between 1 and 8 μm.

$$I \simeq \sum_i I_{\lambda_i} (\lambda_{i+1} - \lambda_{i-1})/2$$

A program has been written to perform these computations. It has the capability of determining the radiant intensity, both spectral and total, from any inhomogeneous mixture of CO_2, H_2O, CO, soot, and coal. There are no requirements on temperature or concentration profiles as long as the distance intervals are chosen sufficiently small. If the coal particle concentration is too large, errors are introduced since particle scattering is not considered. Under the conditions of the furnace in the present study, neglecting scatter should be reasonable.

The program is divided into six subprograms, one function routine, and a section for block data. The main program has the name RADCALC. Its purpose is to read in data, determine the optical depth in each distance

and wavelength interval, integrate the equation of transfer, and print and punch the output. The calculational procedure follows closely the technique suggested by Ludwig, et al. (1973). For each wavelength and distance interval, j, the calculation starts after reading in partial pressure $P_{i,j}$, temperature T_j, and distance interval ℓ_j, by determining the pressure path length, $u_{i,j}$, and Lorentz line half-width, γ_{L_i}, for each gas component, i = 1 to n.

$$u_{i,j} = P_{i,j}\ell_j\left(\frac{273}{T}\right)$$

$$\gamma_{L_{i,j}} = \sum_{i=1}^{n} \gamma_{i,j_{273}} P_{i,j}\left(\frac{273}{T_j}\right)^{M_{i,j}}$$

The optical depth for the weak-line limit, X_{weak}, and the line width to spacing parameter, a, are then calculated for each of the M intervals.

$$X_{weak_i} = \sum_{j=1}^{M} \left(\frac{\overline{S}}{d}\right)_{i,j} u_{i,j}$$

$$a_i = \frac{1}{X_{weak_i}} \sum_{j=1}^{M} \gamma_{L_{i,j}} \left(\frac{\overline{1}}{d}\right)_{i,j} \left(\frac{\overline{S}}{d}\right)_{i,j} u_{i,j}$$

Here $(\overline{1/d})$ is the inverse of the line spacing and is related to the mean strong-line parameter by

$$(\overline{1/d}) = \frac{\left(\overline{S^{1/2}/d}\right)^2}{(\overline{S/d})}$$

Using the Curtis-Godson expression, the optical depths for each species are calculated as mentioned in section B. The total transmittance can then be calculated and, with the black-body intensity for the particular interval temperature, can be used to determine the spectral intensity. This is done for all wavelength intervals of interest and the results

then added to get the total intensity.

The values of $(\overline{S/d})$ and $(\overline{1/d})$ as a function of species temperature, partial pressure, and wavelength are calculated in the subroutines COEFCO2, COEFH2O, and COEFCO for CO_2, H_2O, and CO, respectively. The CO parameters are calculated rigorously from the anharmonic, non-rigid, rotator model of Malkmus and Thomson (1961). The parameters for the 4.3μm band of CO_2 are calculated from Malkmus (1962), while for the 2.7 μm band, the model of Malkmus (1963) is used. The parameters for all the bands of water are determined by interpolation of the data tabulated by Ludwig, et al. (1973), and which is included in BLOCK DATA. Provision is made for an additional species such as methanol or methane to be included if a suitable calculational procedure is found. This would then be inserted in subroutine COEFUEL.

The absorption coefficient and optical depth due to particulate radiation is calculated in subroutine POD. This routine contains the algebraic expressions discussed in section B.1 of this chapter.

The function routine, PLANCK, is called whenever the black-body intensity is to be calculated.

The output of the program includes the total intensity and a listing of the spectral intensity versus wavelength, along with all of the input composition and temperature profiles. The spectral intensity is also punched on cards so that it may be plotted by insertion into the program called PLTEMIS.

A complete listing of these and other programs, along with input instructions are to be found in Grosshandler (1976).

VI. RESULTS OF RADIATION MEASUREMENTS IN THE FURNACE

The visible radiation from the furnace burning methanol and a methanol/coal slurry can be seen in the photgraphs in Figure VI-1. The photographs were all taken with an electronic flash at 1/60 second, and the f-stop was not changed for the two furnace conditions. The pure methanol flame is almost invisible in photographs a) and b) but particulate radiation can be seen in c) and d) from the methanol/coal flame. A photograph of the methanol/coal flame without a flash is shown in Figure VI-2. The camera was set at 1/1000 second and focused on the center of the flame.

The visible radiation is not always a good indication of the infrared radiation. To measure the infrared radiation, the technique discussed in Chapter III was used. Selected results of these measurements are presented here. These are compared with calculated intensities from the program RADCALC and other more simplified models.

A. Methanol as the Fuel

The measured spectral intensity at four different axial locations is shown in Figure VI-3 through VI-6 as a function of wavelength. The most predominant feature of all four of the plots is the peak at 4.26 μm resulting from carbon dioxide. Of almost equal importance is the double humped band centered around 2.7 μm. This is due to both the water and CO_2 in the combustion gas. Smaller water peaks occur at 1.38 and 1.88 μm.

a) Methanol as the Fuel

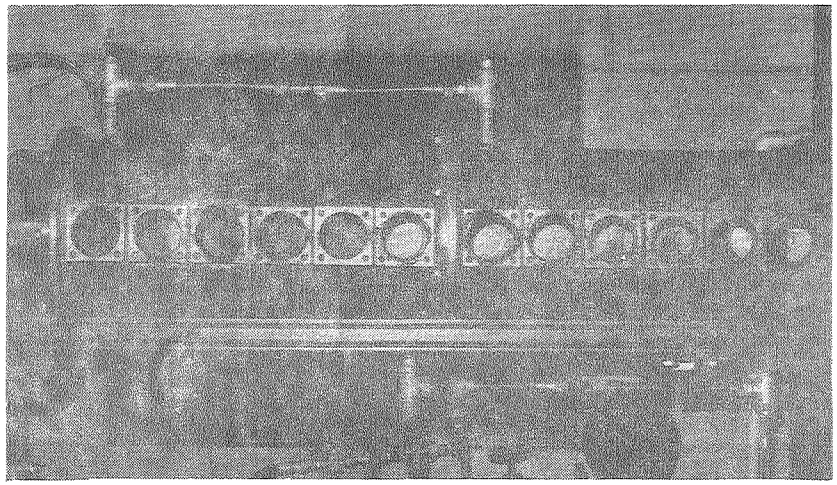

c) Methanol/Coal Slurry as the Fuel

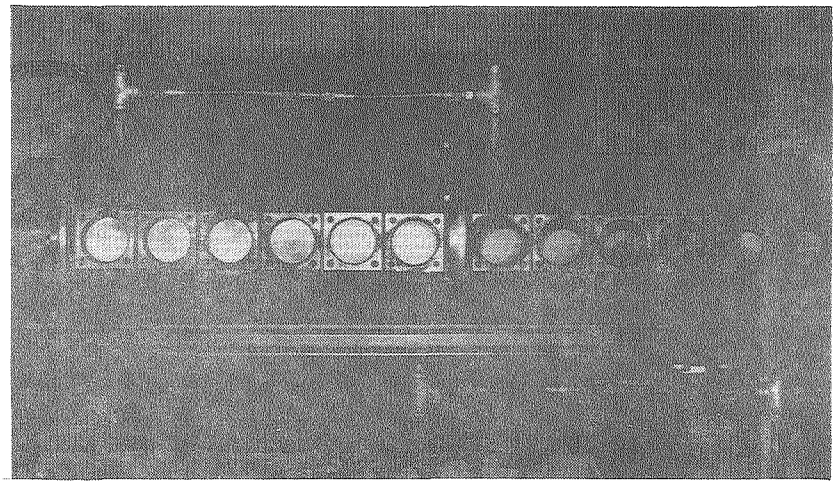

b) First Three Ports, Methanol

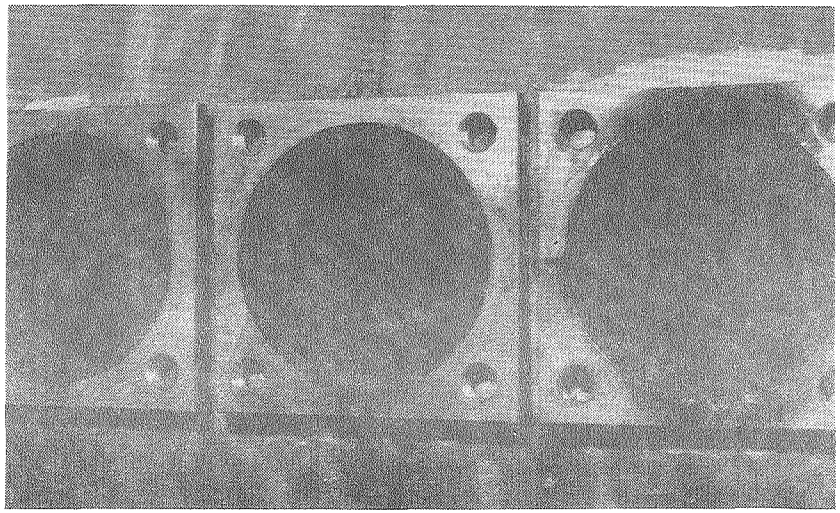

d) First Three Ports, Methanol/Coal Slurry

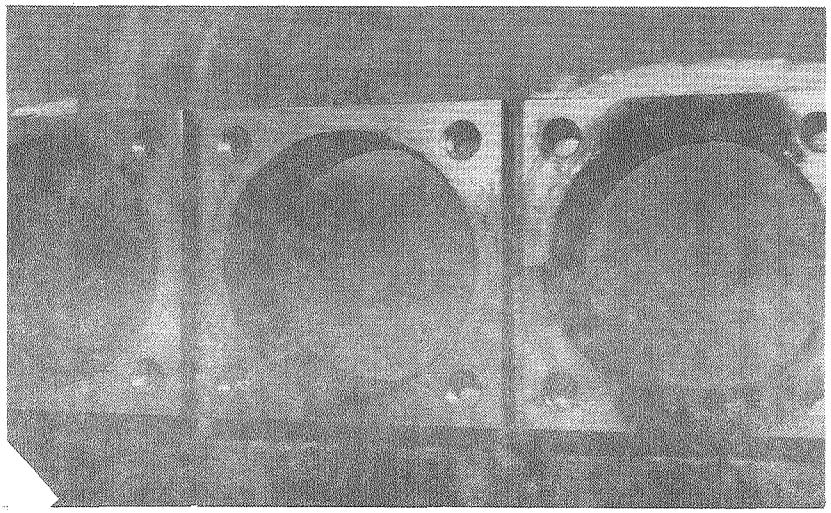

FIGURE VI-1. Visible Radiation from Experimental Furnace

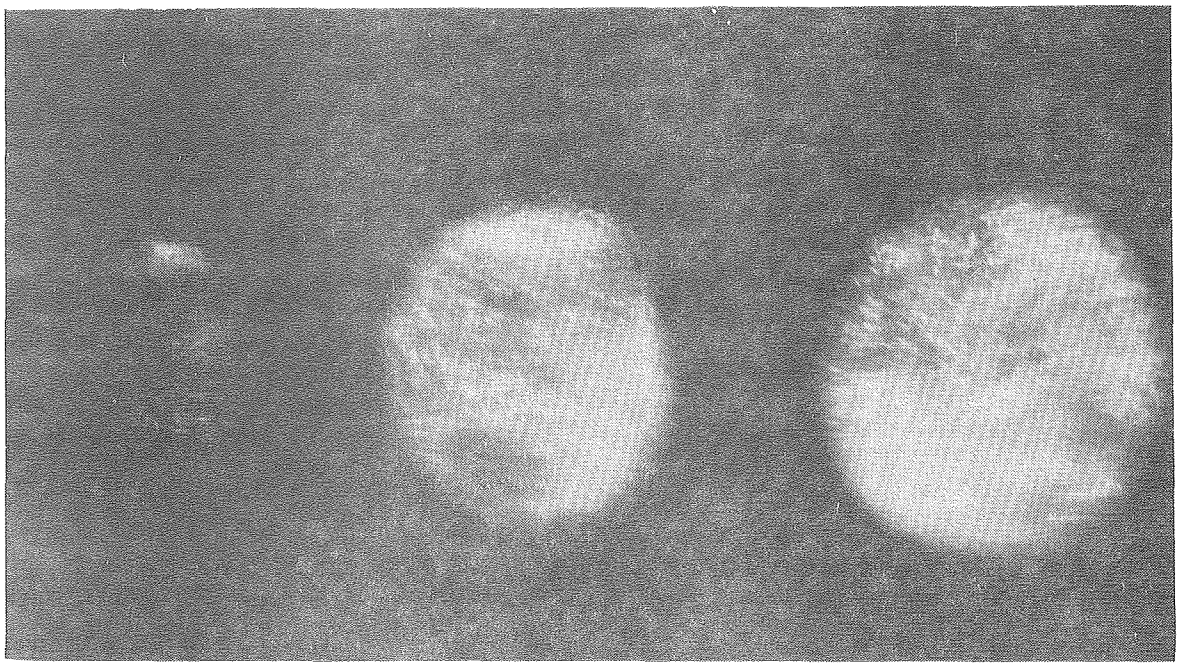

FIGURE VI-2. Visible Particulate Radiation from First Three Ports of Furnace Burning Methanol/Coal Slurry (1/1000 sec)

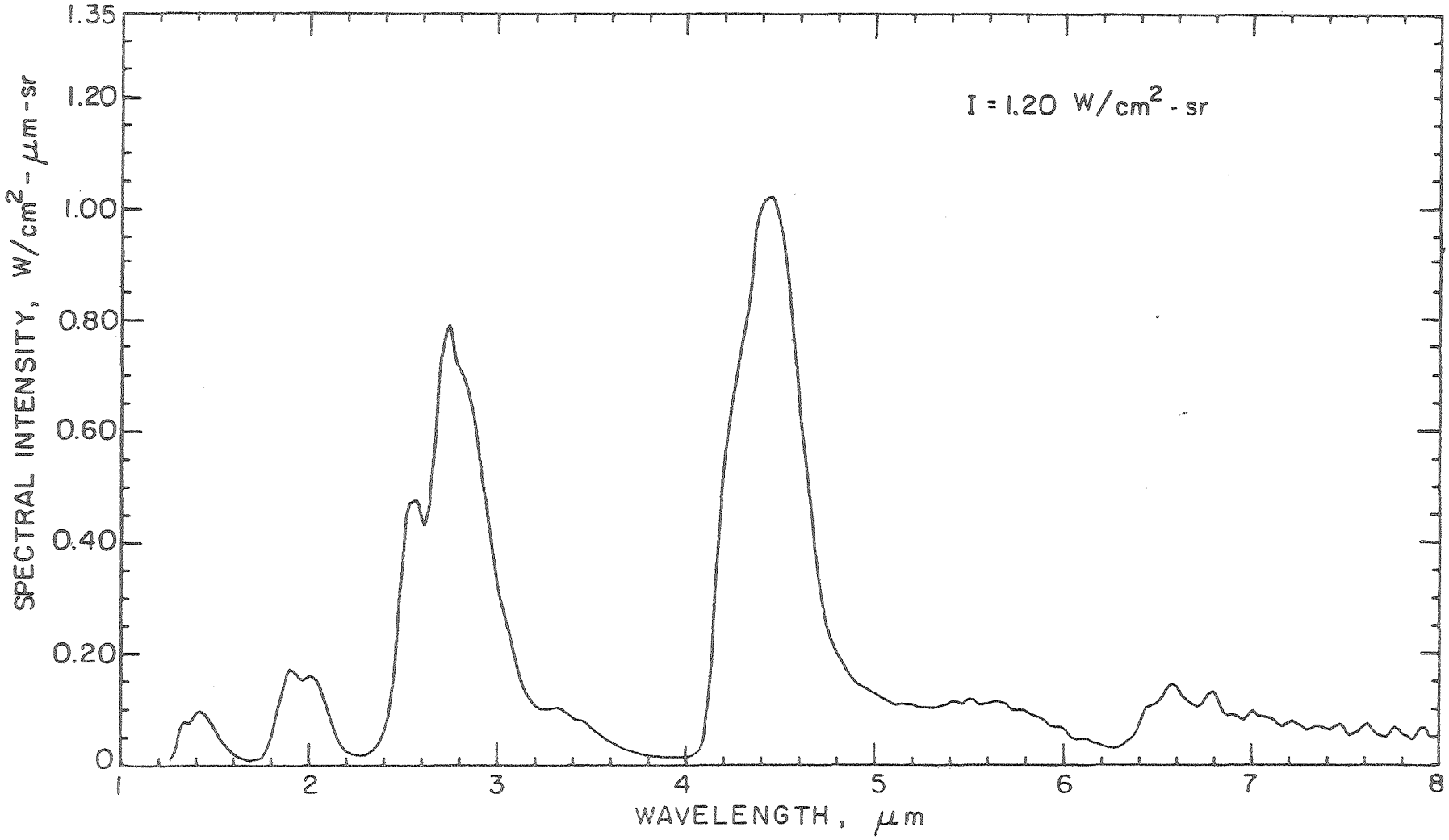

FIGURE VI-3. Measured Spectral Intensity (x = 12.7 cm)

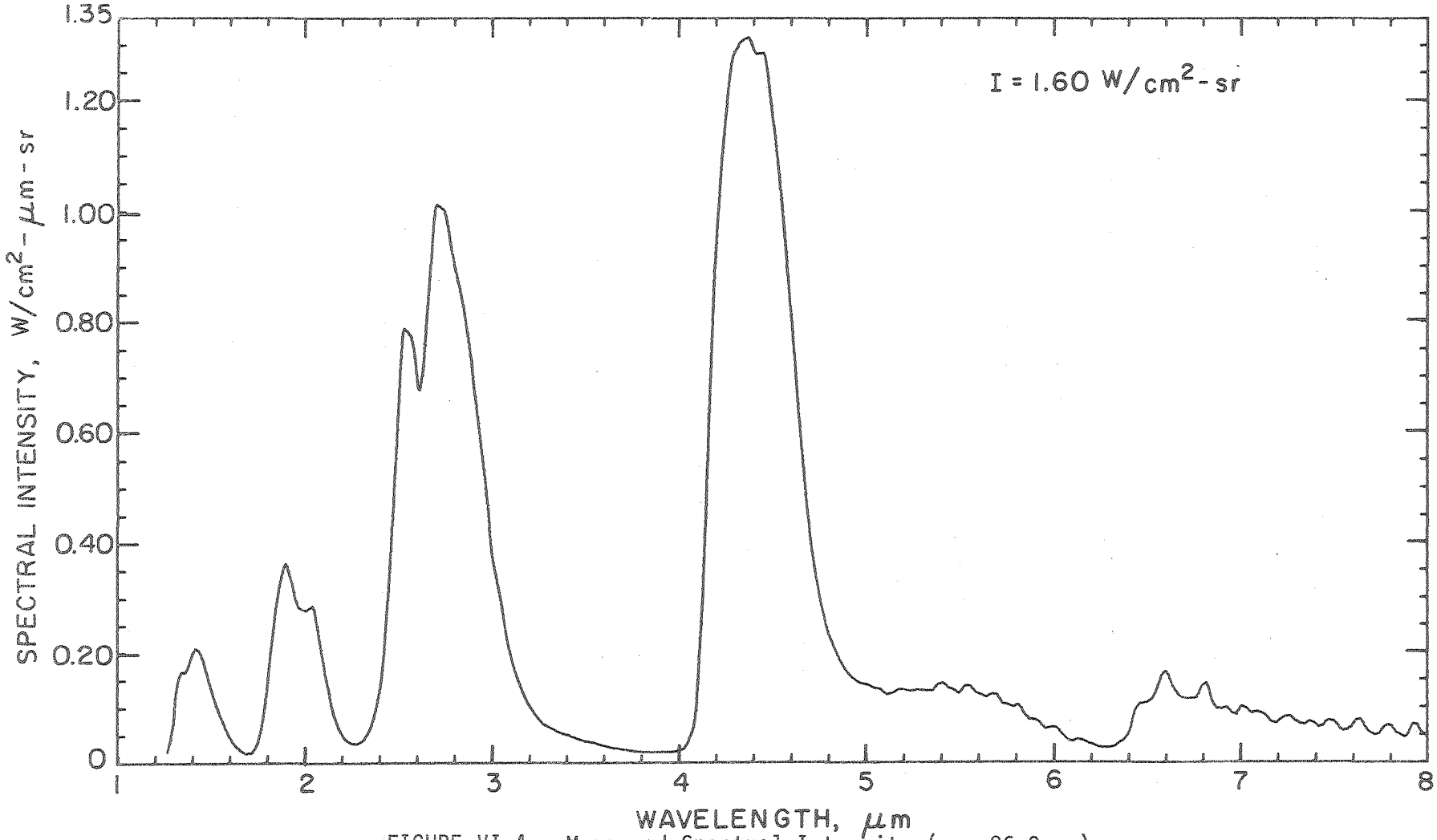

FIGURE VI-4. Measured Spectral Intensity (x = 26.9 cm)

The low broad band centered at 6.27 μm and stretching from below 5 to greater than 8 μm is also due to water vapor. Since it is the area under the peak and not the absolute maximum which is important, this band makes an appreciable contribution to the total heat transferred from the flame.

In addition to the above vibration-rotation bands, Figure VI-3 shows evidence of a band at 3.3 μm which is due to C-H vibrations. By a position 26.9 cm downstream, the hump at 3.3 μm is not discernable above the wing of the 2.7 μm band, indicating that most of the fuel has been consumed by that time. A careful inspection of the four spectra at 5 μm shows a change in slope from negative at 12.7 cm downstream to about zero at 26.9 cm to positive at 58.4 and 86.9 cm. This is due to the gradual disappearance of carbon monoxide, which has a peak at 4.67 μm, as the combustion gases continue to react.

Since the water and carbon dioxide approach their equilibrium values early in the furnace and maintain them, the change in height for the major peaks can be attributed mostly to the change in furnace temperature. The peak intensities are moderate at 12.7 cm, reach a maximum at 26.9 cm, are again modearate at 58.4 cm, and have diminished to half their maximum values by 86.9 cm. The shoulder which appears on the left side of the 4.26 μm peak in Figure VI-5 and 6 is due to absorption by a relatively cool layer of CO_2 which sits just in front of the monochromator window.

If each of these spectra are integrated across wavelength, the result is the total intensity leaving the flame at any given axial position in a horizontal direction perpendicular to the furnace axis. The total intensity is shown in Figure VI-7 plotted as a function of axial distance downstream of the fuel nozzle. A maximum intensity of about 1.6 W/cm^2-sr

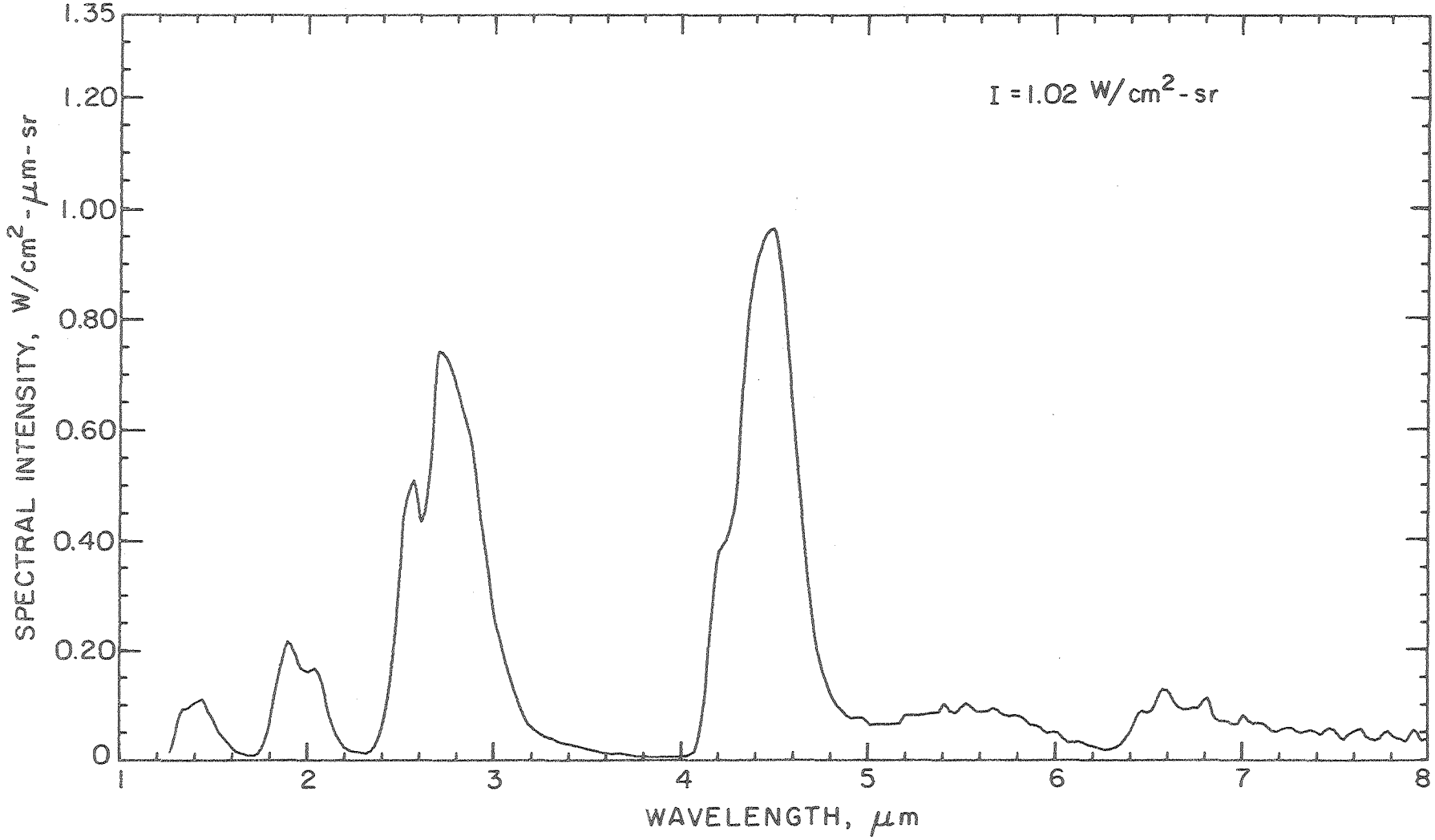

FIGURE VI-5. Measured Spectral Intensity (x = 58.4 cm)

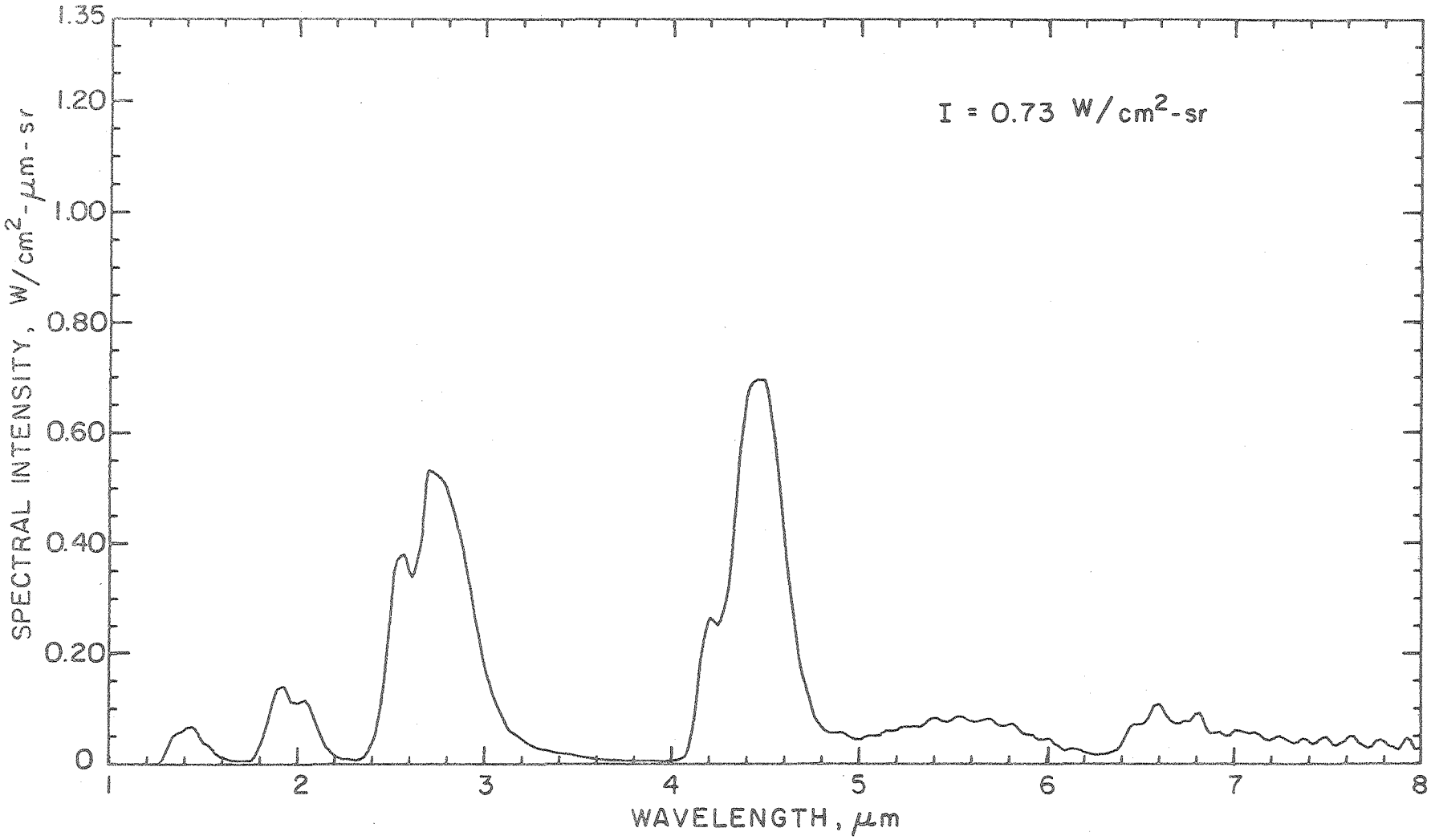

FIGURE VI-6. Measured Spectral Intensity (x = 86.9 cm)

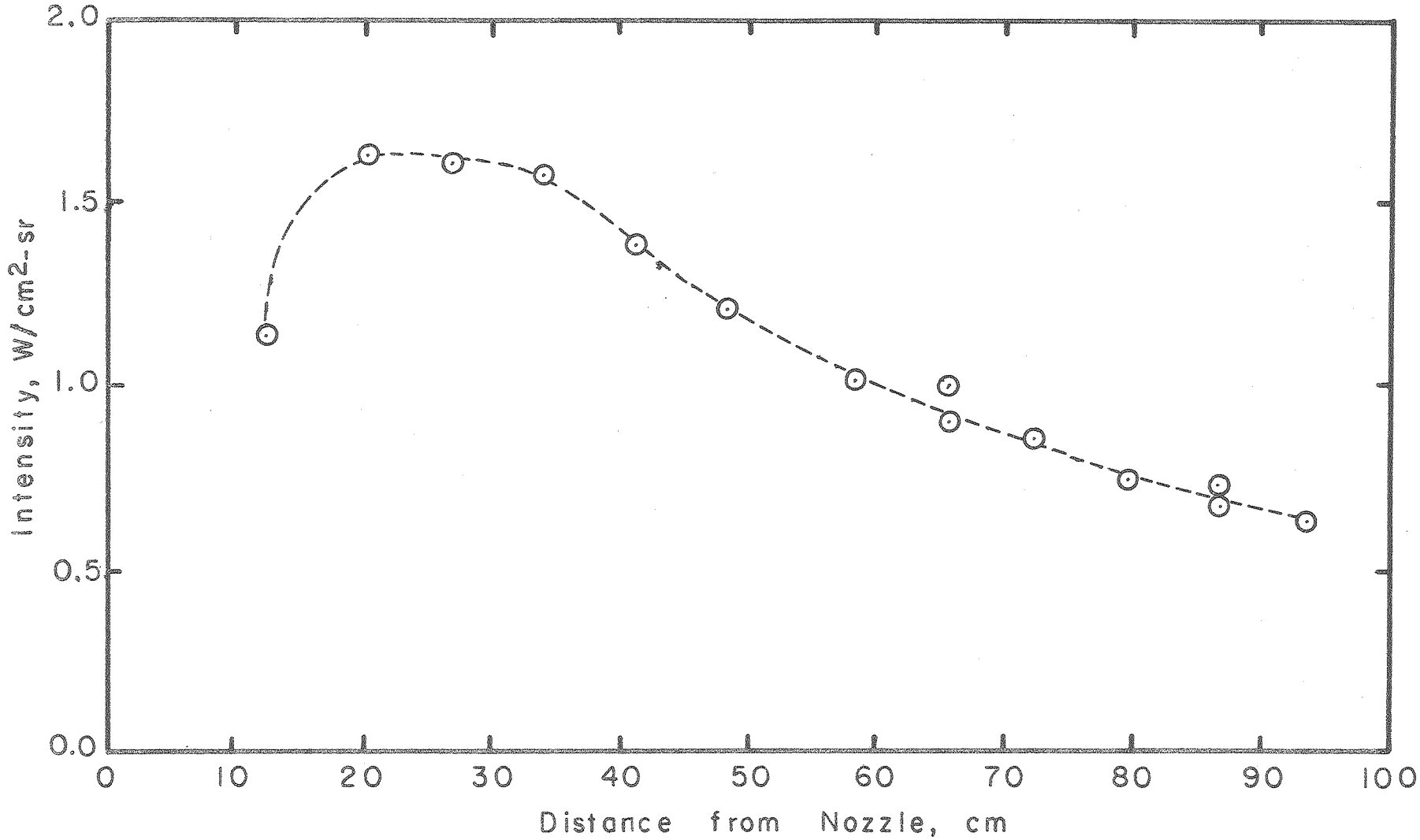

FIGURE VI-7. Total Intensity Variation Along Axis of Methanol Furnace

is reached 20 cm downstream, and the intensity drops to about .65 W/cm^2-sr at the furnace exit. The double set of points at axial positions of 66 and 87 cm is from a duplication of runs taken on different days with differing calibrations. The reproductability is good.

B. Methanol/Coal Slurry as the Fuel

Radiant intensity measurements similar to those in the pure methanol flame were taken. The intent was to quantify the effect of adding 5.3% coal to the fuel on the flame intensity, assuming the basic structure of the flame was not significantly perturbed by the coal. As mentioned in Chapter IV, the nozzle diameter had to be increased to allow burning of the slurry, resulting in a significant change in the structure of the flame near the furnace entrance.

Figure VI-8 shows the spectral intensity taken 26.9 cm downstream of the nozzle. The dotted line is included to allow comparison between the two fuel systems. Of primary interest in this experiment was to observe the increase in continuous radiation by adding coal to the fuel. The continuous radiation can be observed by looking between the peaks, especially at 1.7 and 2.3 μm. Even though the total radiation from the gaseous species has been decreased by the change in flame structure, the continuous radiation at these locations has increased considerably.

Figures VI-9 and 10 show two more spectra taken 58.4 and 86.9 cm downstream of the nozzle, respectively. Just as the flame structure of the two fuel systems becomes more similar with increasing axial distance, so does the flame intensity. The difference in the banded radiation is not large in these two figures. The continuous radiation at 1.7 and 2.3μm is still apparent at 58.4 cm; but, by 86.9 cm the decrease in temperature

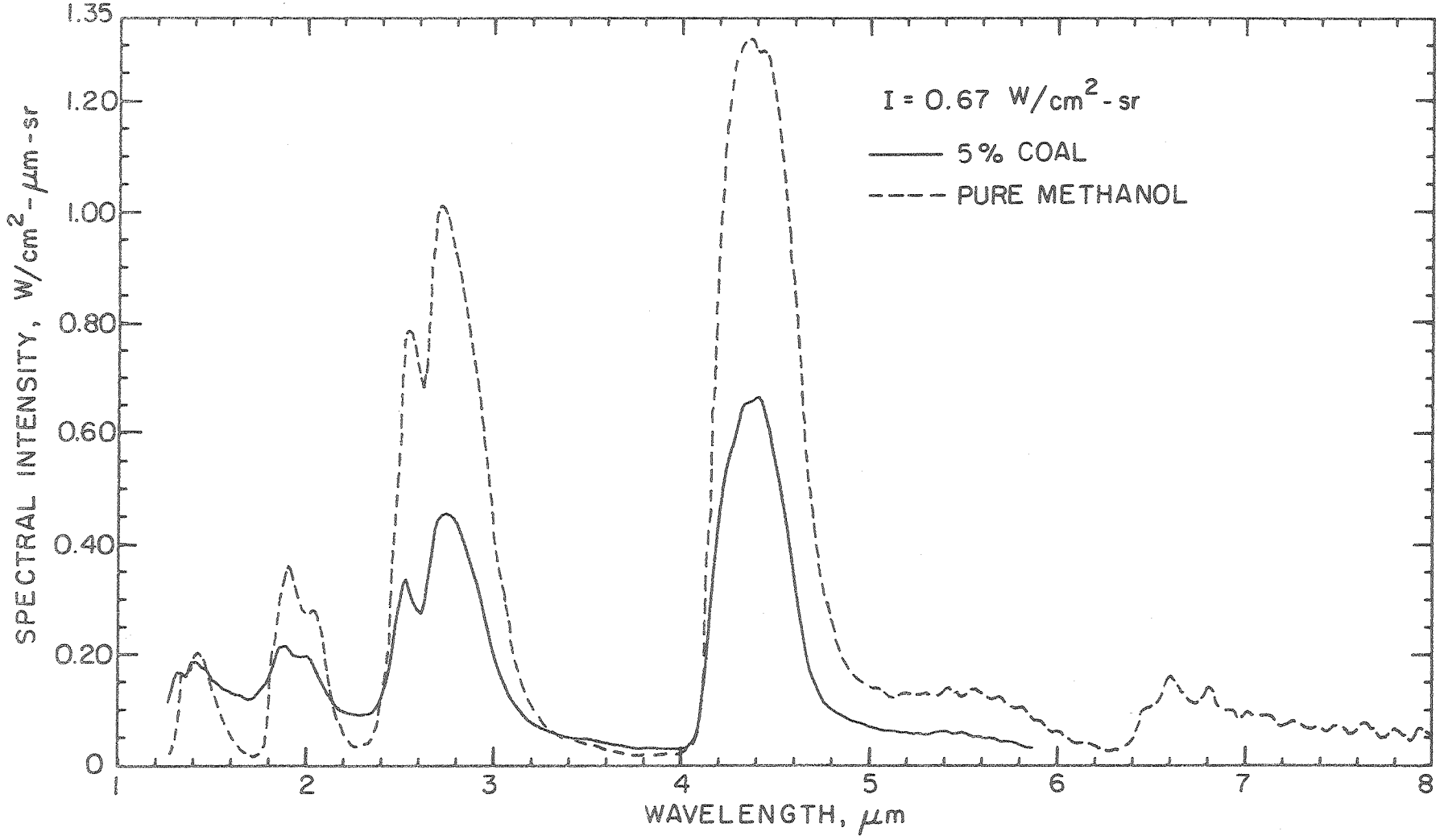

FIGURE VI-8. Measured Spectral Intensity With 5% Coal (x = 26.9 cm)

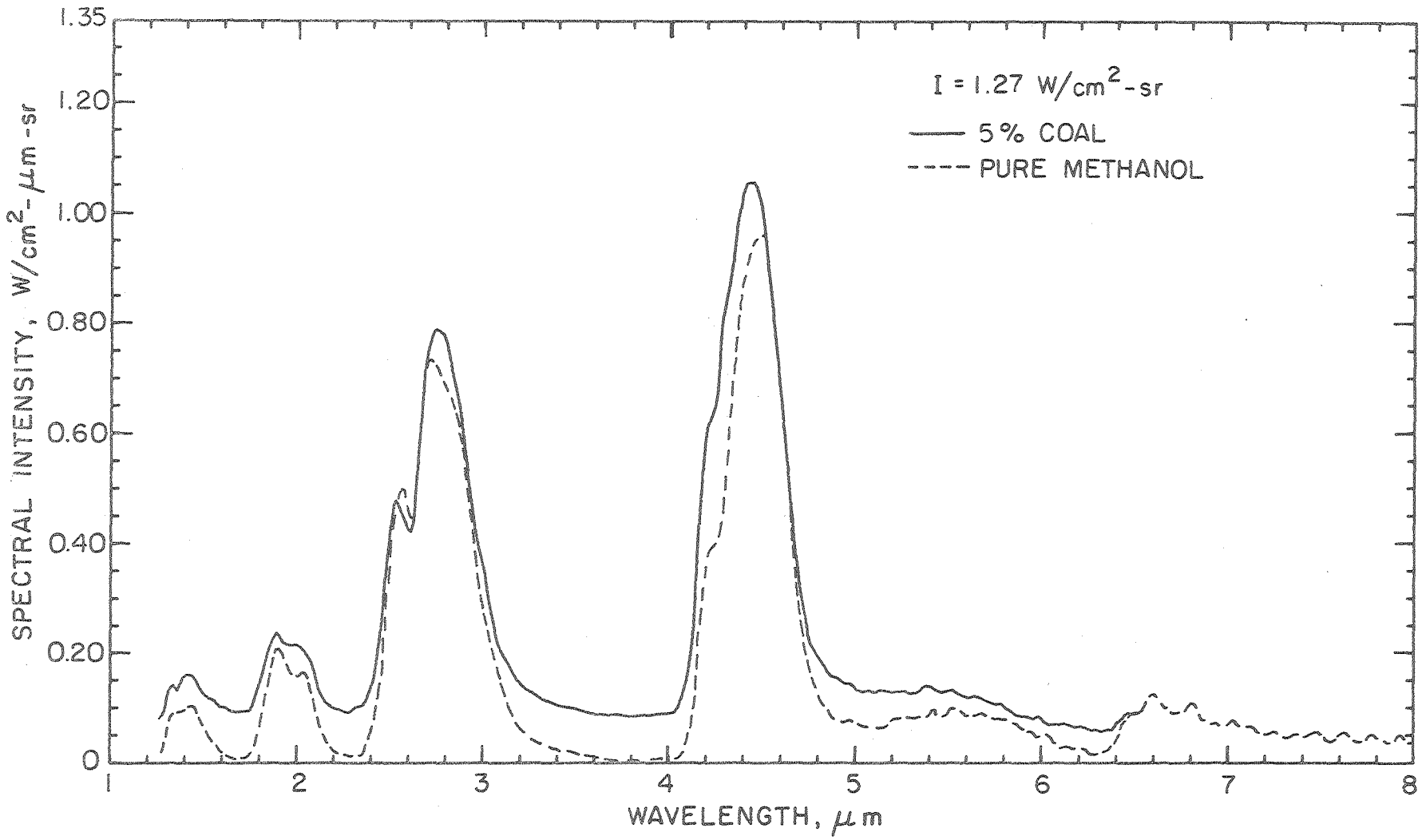

FIGURE VI-9. Measured Spectral Intensity With 5% Coal (x = 58.4 cm)

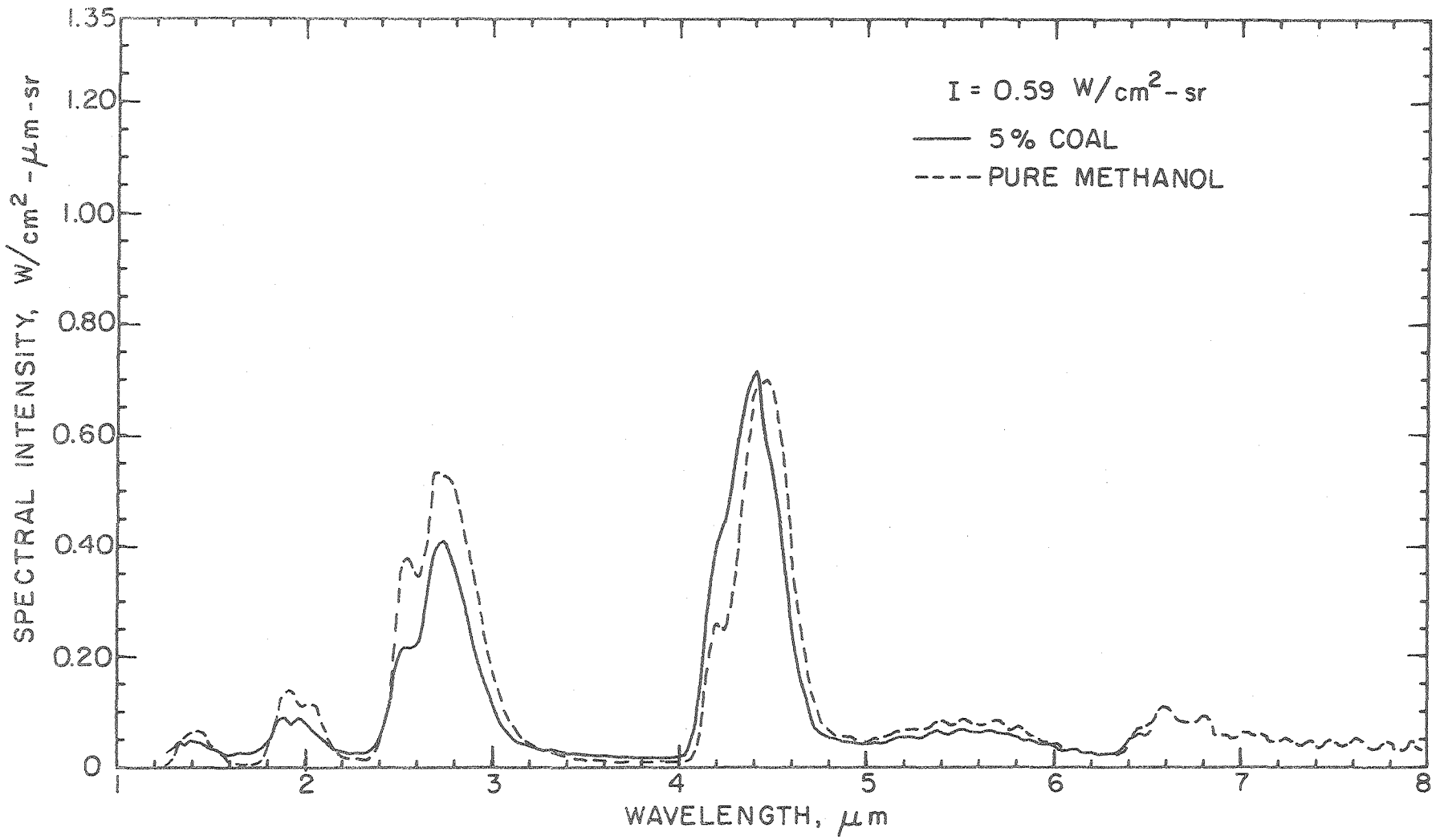

FIGURE VI-10. Measured Spectral Intensity With 5% Coal (x = 86.9 cm)

0 0 0 4 / 0 0 0 9 6

along with the burn-out of the coal has reduced the radiation from the particulates.

The high value of spectral intensity between 3.5 and 4 μm on Figure VI-7 indicates that particles have built up on the walls. The intensity contribution from particles in the flame can be estimated by measurements at 1.7 and 2.3 μm. Based on a reasonable particle temperature of 1500 K, the value of intensity due to the high temperature particle cloud should be reduced by a factor of three at 4 μm. The discrepancy in intensity at 4 μm can be made up if it is assumed the walls act as a blackbody at 700 K. Even though the walls are water-cooled and are kept below 373 K with the pure methanol fuel, coal build-up insulates the cold surface from the hot particles which impact on top of this insulation layer. This problem can be avoided in future work by redesigning the furnace wall plugs opposite the viewing ports.

In addition to particel build-up on the walls, there is the problem of particles depositing on the monochromator viewing windows. This is accounted for by taking two spectra consecutively. If there were no build-up on the windows, both spectra would be the same. By measuring the decrease in intensity between the two, it is possible to formulate a degradation factor which is a function of time and wavelength. This is done and the recorded data is corrected in the data reduction program, FLAMRAD (Grosshandler, 1976).

The spectral emittance is defined for a homogeneous volume emittor as the spectral intensity which leaves the volume divided by the spectral intensity that a blackbody would emit at the same temperature and wavelength. The emittance 26.9 cm downstream of the nozzle is plotted in Figure VI-11. The dotted line is for pure methanol and the solid line is

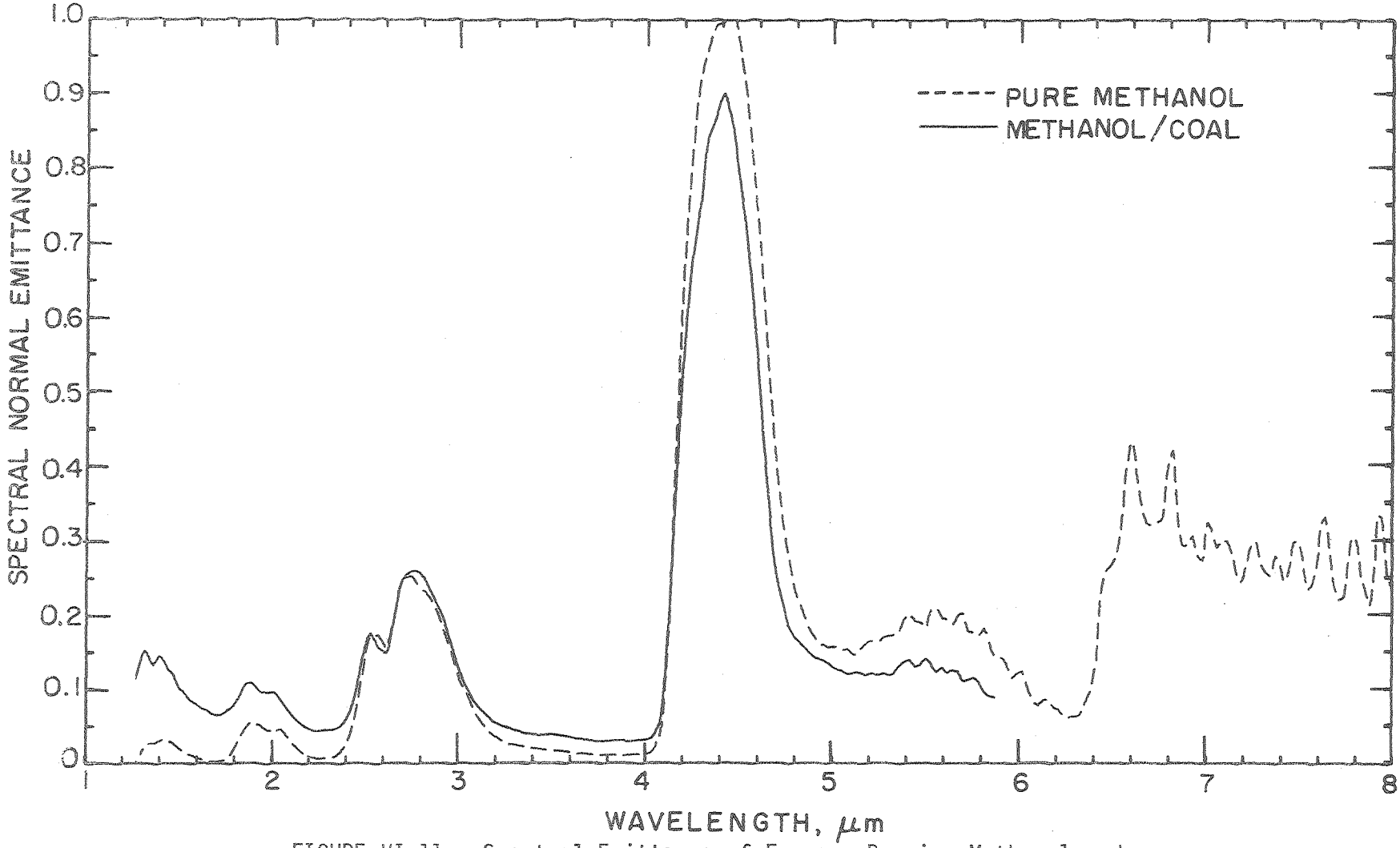

FIGURE VI-11. Spectral Emittance of Furnace Burning Methanol and a Methanol/Coal Slurry (x = 26.9 cm)

with the addition of 5.3 % coal. The line of sight is not homogeneous, so an average fourth power of temperature was used to predict the black-body radiation. The effect of the coal particles is to increase the emittance of the flame at the shorter wavelengths, and the effect of the different nozzle is to decrease the gas emittance. The total emittance for the coal-seeded flame is .135 compared to an emittance of .098 when no coal is added.

Siegel and Howell (1972) suggest that the absorption coefficient of soot can be fitted to an empirical expression of the form

$$Ka_{\lambda_{soot}} = \alpha\tilde{W}\ \lambda^{-\beta(\lambda)}$$

where $\tilde{W}$ is the average soot cloud density, α is a constant related to the size distribution, and β is a constant for a given wavelength which depends on the optical properties of the soot. It is assumed that this expression holds for coal particles as well as soot, and that the wavelength dependence of β is negligible. The emittance is related to the absorption coefficient by

$$\varepsilon_\lambda = 1 - \exp(-Ka_\lambda \ell)$$

Therefore, since the particulates account for all the emittance in the region between the gas bands, values for α and β can be determined from two values of emittance by the relation

$$\frac{\alpha\ \tilde{W}\ell}{\lambda^\beta} = -\ln(1 - \varepsilon_\lambda)$$

The expression for the absorption coefficient then becomes

$$Ka_\lambda = 1.70\ \tilde{W}/\lambda^{1.58}$$

with $\tilde{W}$ in g/cm^3 at flame conditions, λ in μm, and Ka_λ in cm^{-1}. The value of the wavelength exponent is about 50% higher than that for various soots

(Siegel and Howell, 1972). This is due to the much larger size of the coal particles and the difference in optical properties of the coal. A more rigorous treatment for K_{a_λ} was discussed in Chapter V.

The total intensity at each port is graphed in Figure VI-12. A small correction factor has been added to the coal data to allow for the fact that the spectra did not extend all the way to 8 μm as did the pure methanol data. If the point at 34 cm is ignored, a reasonable shape to the curve is obtained. The effect of the coal and the larger nozzle is to reduce the intensity early in the flame and to move the point of maximum intensity further downstream. Near the exit of the furnace, as the importance of the inlet jet momentum declines and the coal particles burn out, the intensities of the two fuel systems approach a common value. There is no apparent justification for discarding the data point at 34 cm except that furnace stability is difficult to achieve, and possibly too much fuel was being burned during this particular run. Also, the particulate deposition on the monochromator windows between 20 and 48 cm was large, leading to another possible source of error.

C. Comparison of Results to Those of Radiation Models

With the radial profiles of species concentration and temperature known, it is possible to verify the intensity measurements with the program RADCALC (see Chapter V and Grosshandler [1976]). Three different axial locations were chosen for each of the two fuel systems. The predicted spectra are shown in Figures VI-13 through VI-15 for the pure methanol and Figures VI-16 through VI-18 for the coal/methanol slurry. The dotted lines on each graph are the corresponding measured spectra.

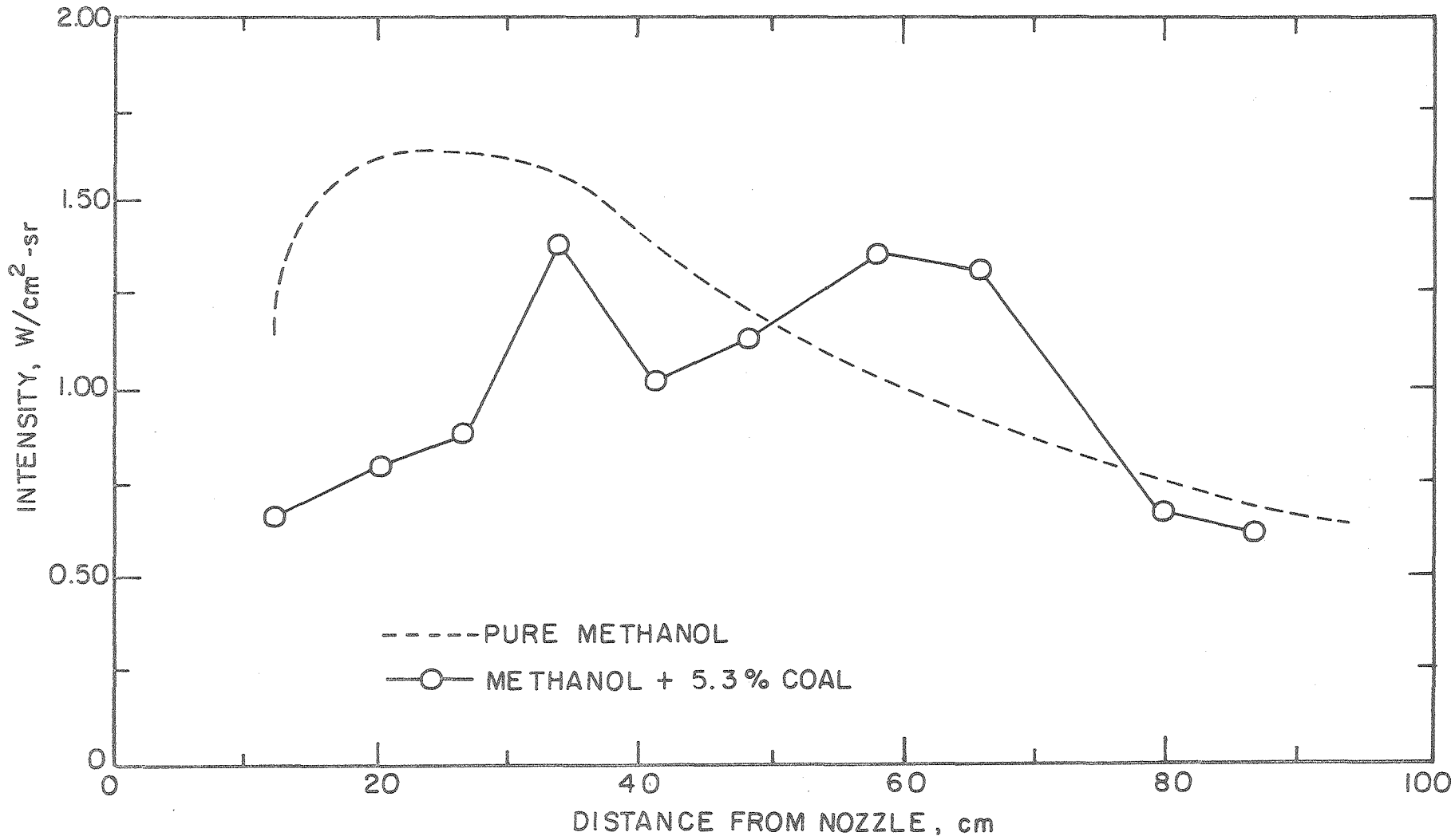

FIGURE VI-12. Total Intensity Variation Along Axis of Furnace

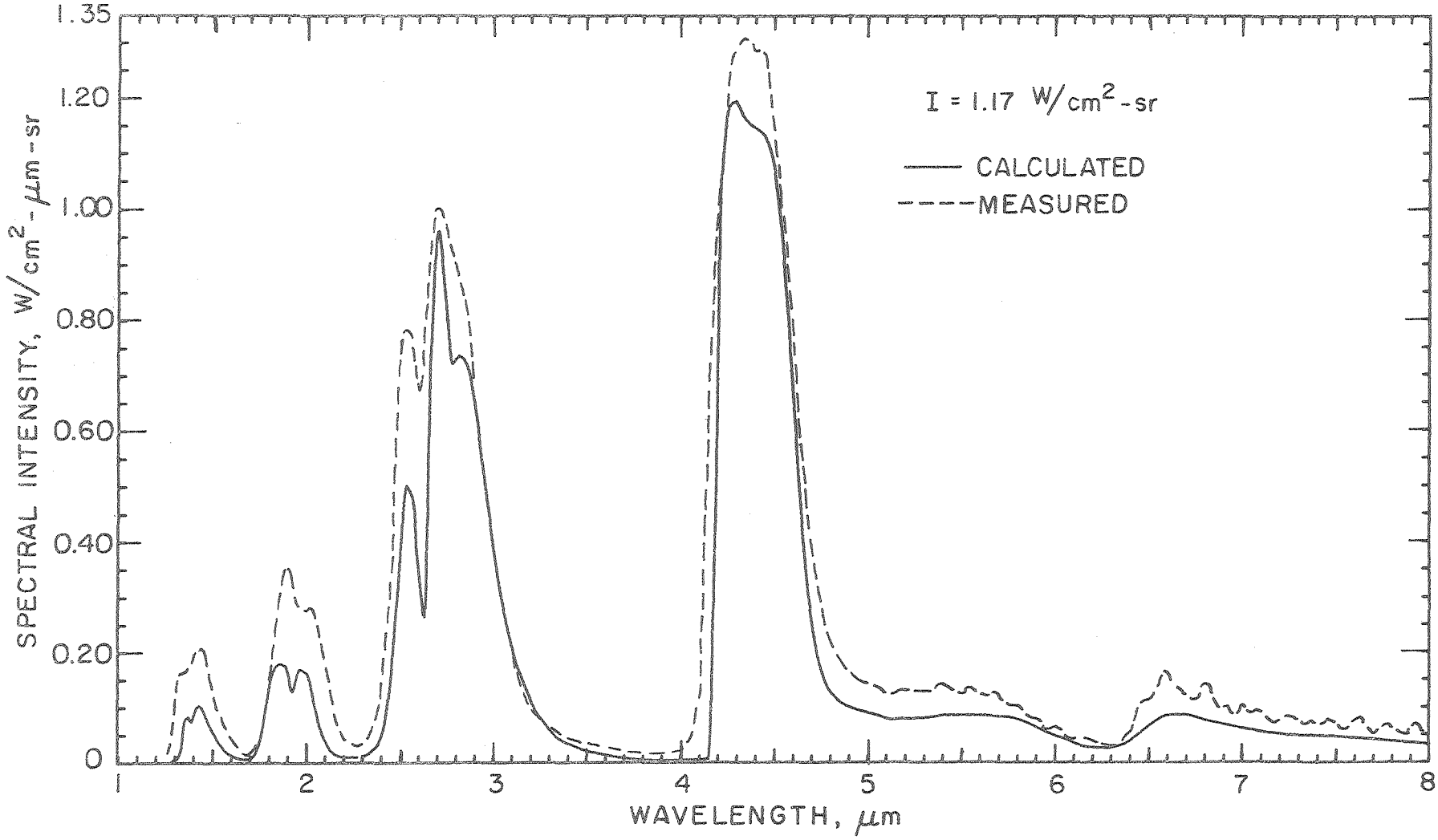

FIGURE VI-13. Calculated Spectral Intensity (x = 26.9 cm)

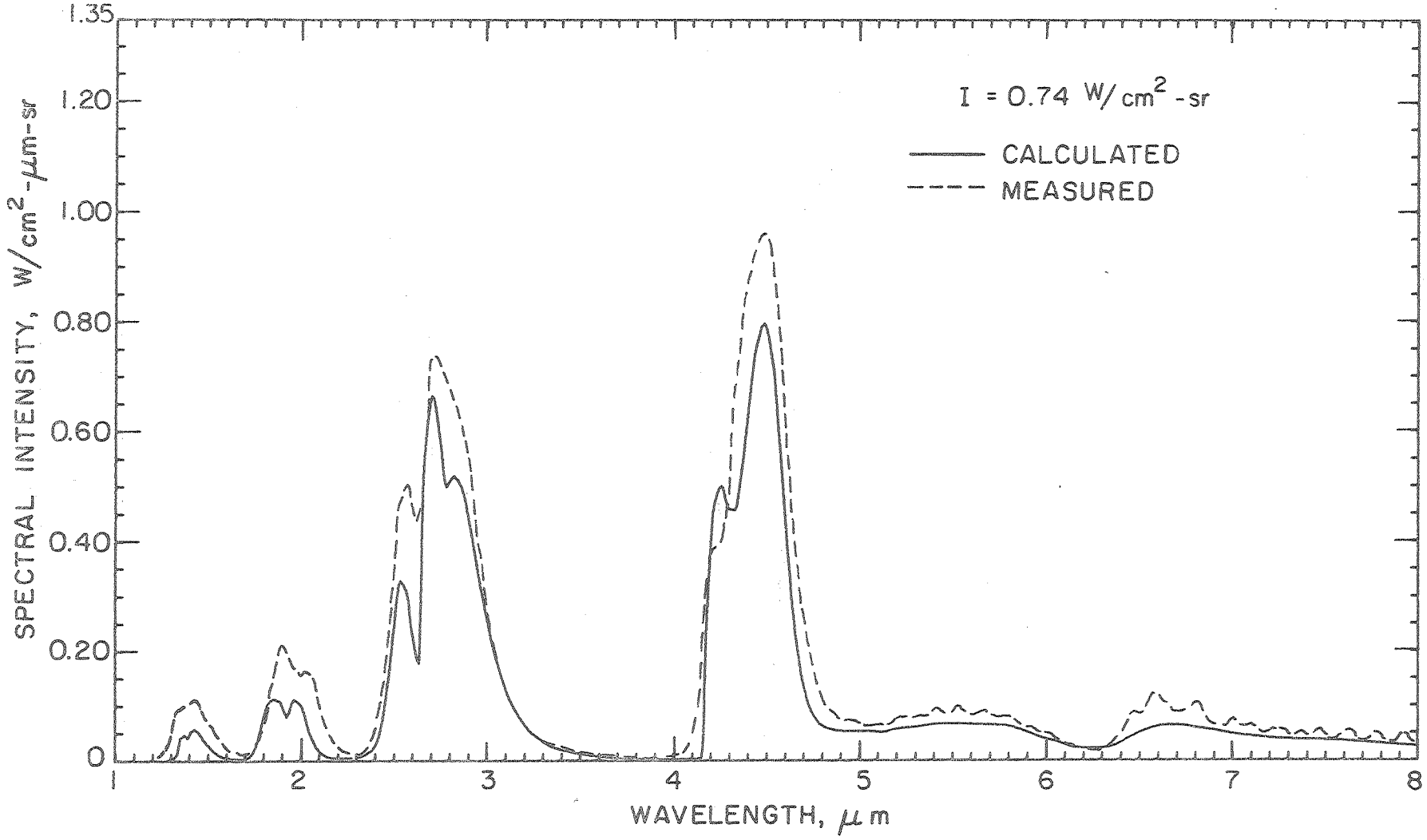

FIGURE VI-14. Calculated Spectral Intensity (x = 58.4 cm)

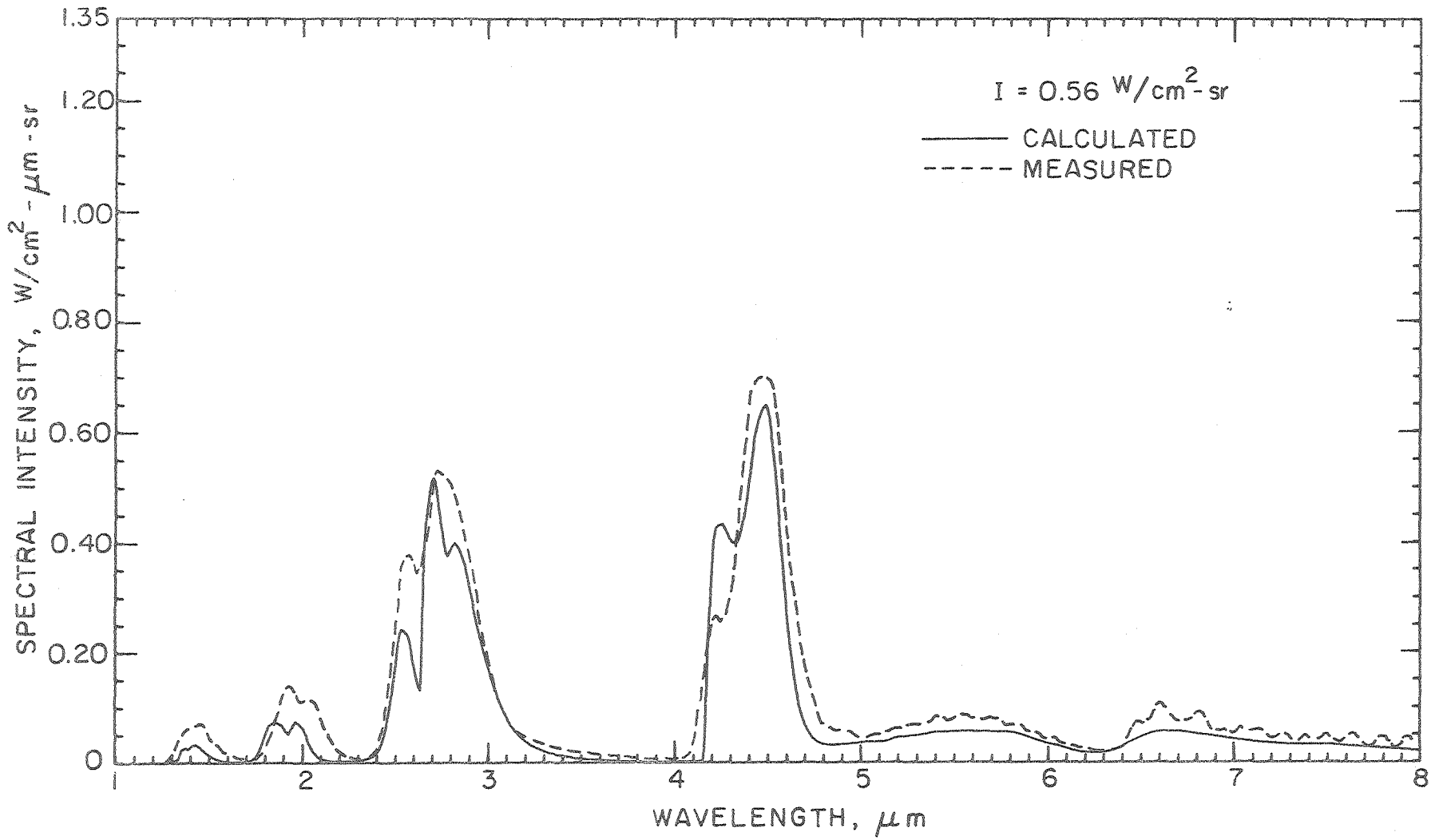

FIGURE VI-15. Calculated Spectral Intensity (x = 86.9 cm)

0004/0040

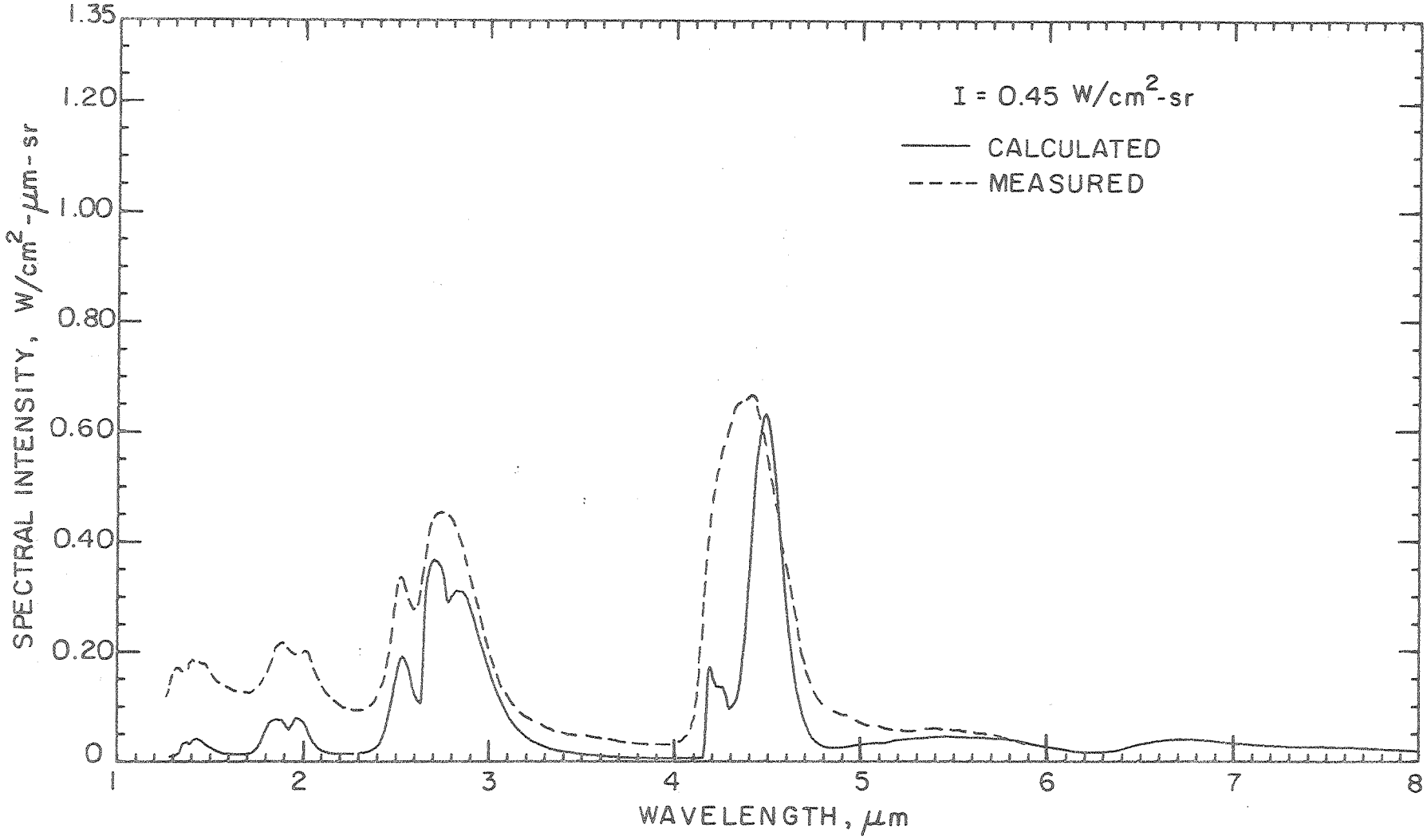

FIGURE VI-16. Calculated Spectral Intensity With 5% Coal (x = 26.9 cm)

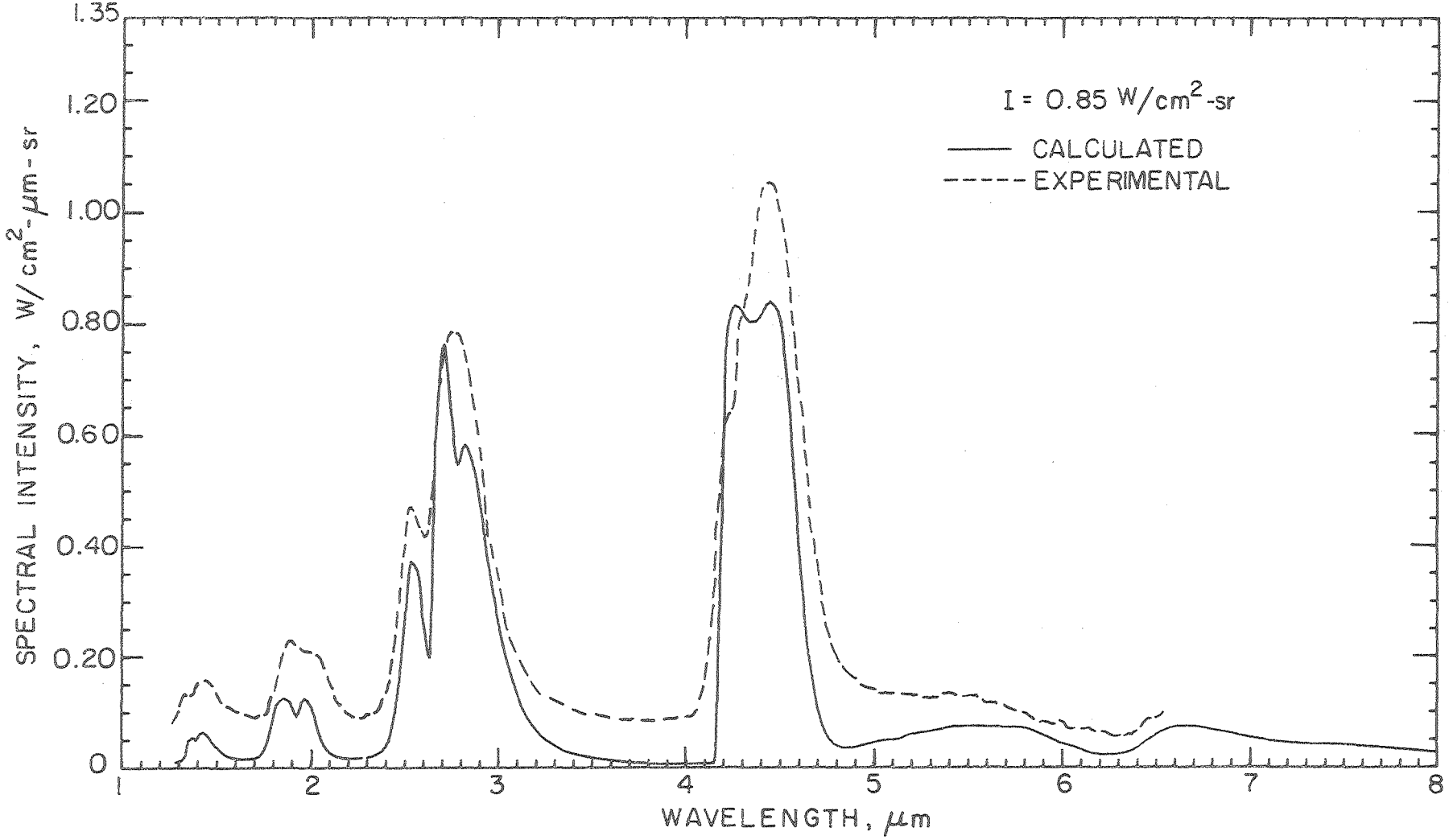

FIGURE VI-17. Calculated Spectral Intensity With 5% Coal (x = 58.4 cm)

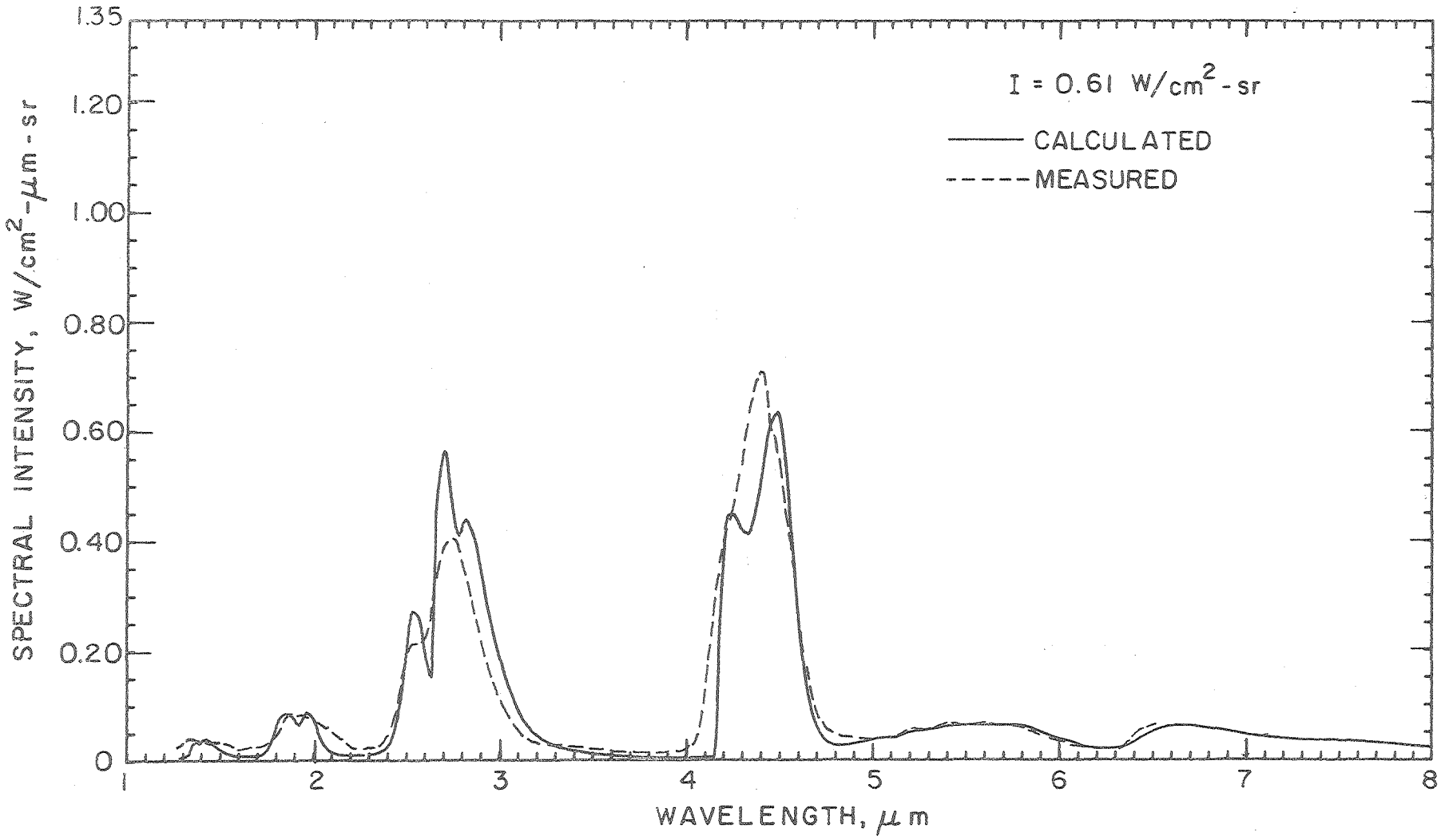

FIGURE VI-18. Calculated Spectral Intensity With 5% Coal (x = 86.9 cm)

Qualitatively, the agreement is satisfactory. All of the major peaks are predicted. The shape of the 4.26 μm CO_2 peak does not agree completely in most cases, nor is the fine structure of the 6.3 μm water band predicted. The major problem, though, is the general under-prediction of the intensity all across the spectrum.

Table VI-1 compares the total integrated intensities of the curves. In all but the last entry, the calculated values are 23 to 33% low. Since the program was verified by using other experimenters' data (excluding particulate radiation), it appears that something else is in error. An explanation is that radiation eminating from the far wall is not negligible. It is true that radiation emitted by the cold wall is negligible, but when a soot layer is allowed to build up, the surface temperature increases and so does the emitted energy. For the pure flame with no soot on the far wall, there is energy which can be reflected into the line of sight.

TABLE VI-1. TOTAL INTENSITIES OF EXPERIMENTAL MEASUREMENTS COMPARED TO CALCULATED INTENSITIES

Axial location	Fuel	Experimental	Calculated	Error
26.9 cm	Pure Methanol	1.60 W/cm^2-sr	1.17 W/cm^2-sr	-27%
58.4		1.02	.74	-27
86.9		.73	.56	-23
26.9	Methanol/Coal	.67	.45	-33
58.4		1.27	.85	-33
06.9		.59	.61	+3

adiabatic equilibrium levels across the entire line of sight. The result is shown in Figure VI-19 for the pure flame case at a distance 58.4 cm downstream. The only noticeable differences are in the 4.26 CO_2 band. Using a larger value of CO_2 than actually exists near the wall results in too much reabsorption, and using the equilibrium value for CO results in an underestimate in intensity at 4.8 μm. Overall, there is a decrease in intensity of less than 3%.

The spectral intensity is much more sensitive to temperature than species. Figure VI-20 shows another calculation with the additional assumption that the temperature is also constant across the diameter and equal to the adiabatic equilibrium value. This causes a gross over-estimation across the entire spectra, yielding a total intensity of 1.86 W/cm^2-sr as compared to .74 W/cm^2-sr when using the measured profile.

In a final attempt, RADCALC was used to predict the intensity with the profiles generated by the Gosman program for recirculating flows. This is shown in Figure VI-21. The agreement is poor when compared to the other calculations and even worse when compared to the measured values. In all fairness to the Gosman program, though, given a finer grid and a more sophisticated turbulence model, the results would be much improved.

To compare the accuracy of the narrow band technique to a wide band model, the Tien-Lowder correlation of the Edwards exponential wide band model was used. For the pure methanol flame at 58.4 cm downstream, the CO_2 and H_2O concentrations and the value of temperature to the fourth power were averaged across the diameter of the furnace. These values (.09 for the CO_2, .185 for the H_2O, and 1549 K for the temperature) were inserted into a program called HMIXRAD to calculate the band radiation.

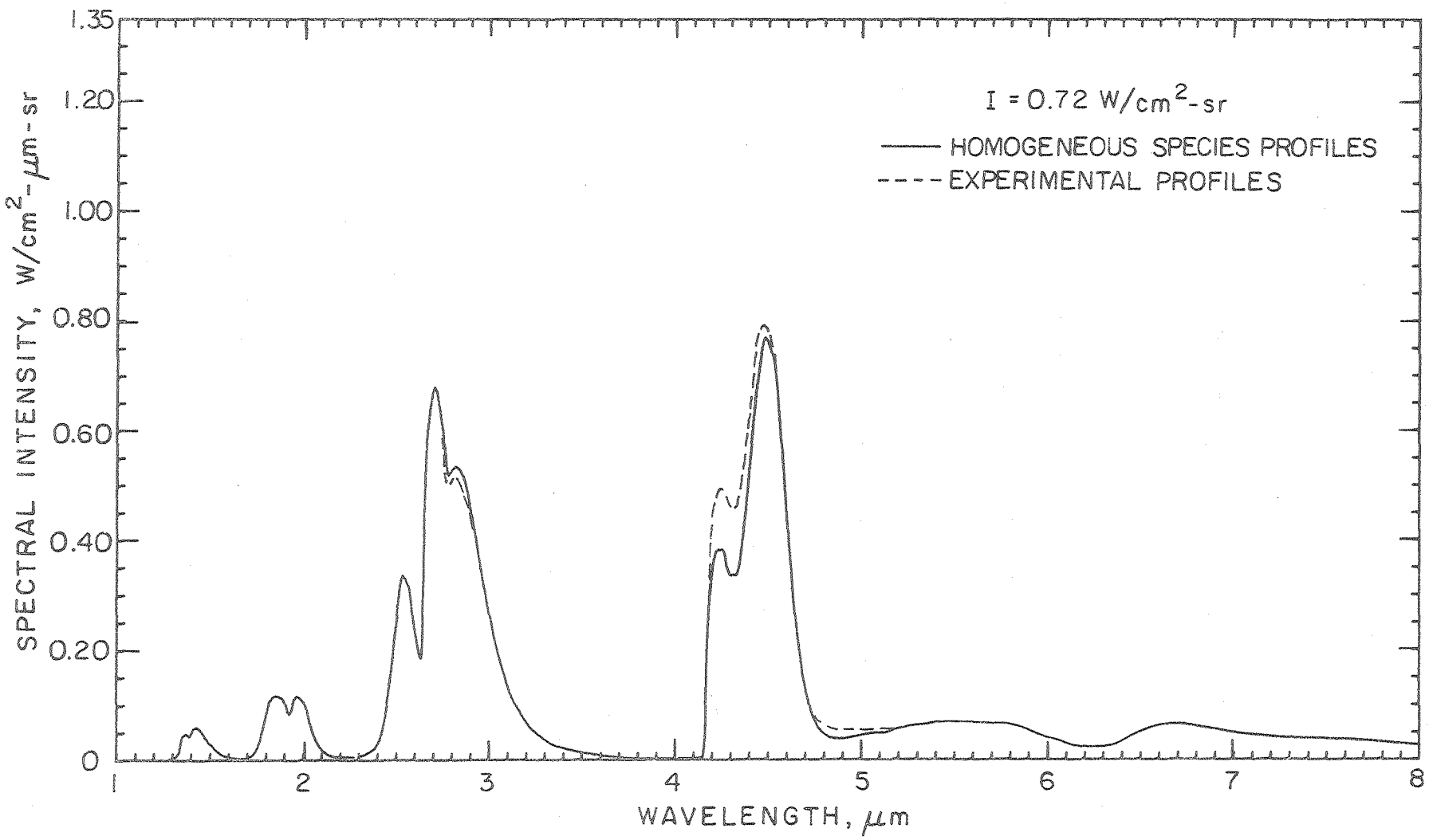

FIGURE VI-19. Calculated Spectral Intensity Assuming Homogeneous Equilibrium Concentrations and Experimental Temperatures (x = 58.4 cm)

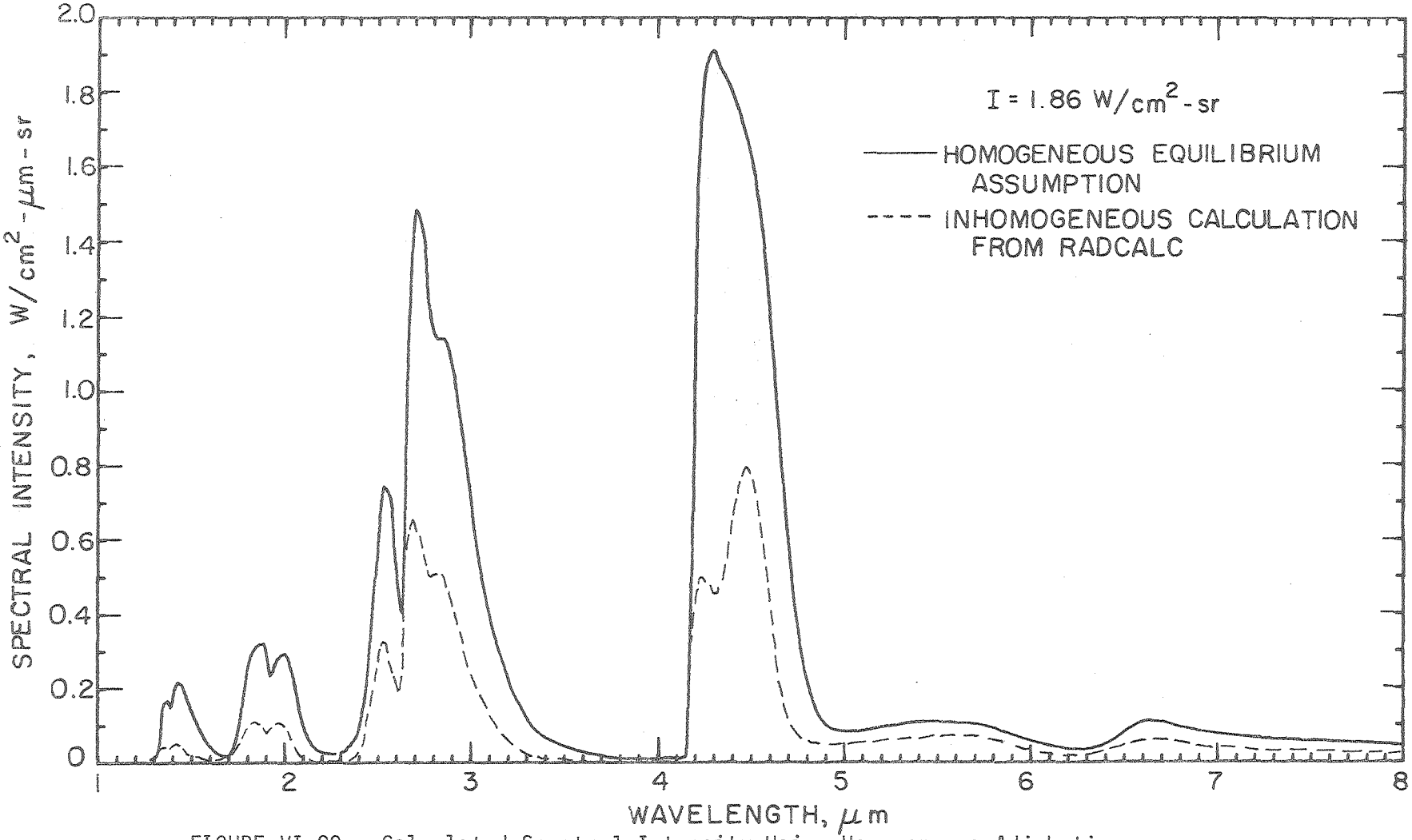

FIGURE VI-20. Calculated Spectral Intensity Using Homogeneous Adiabatic Equilibrium Furnace Conditions

0000470004

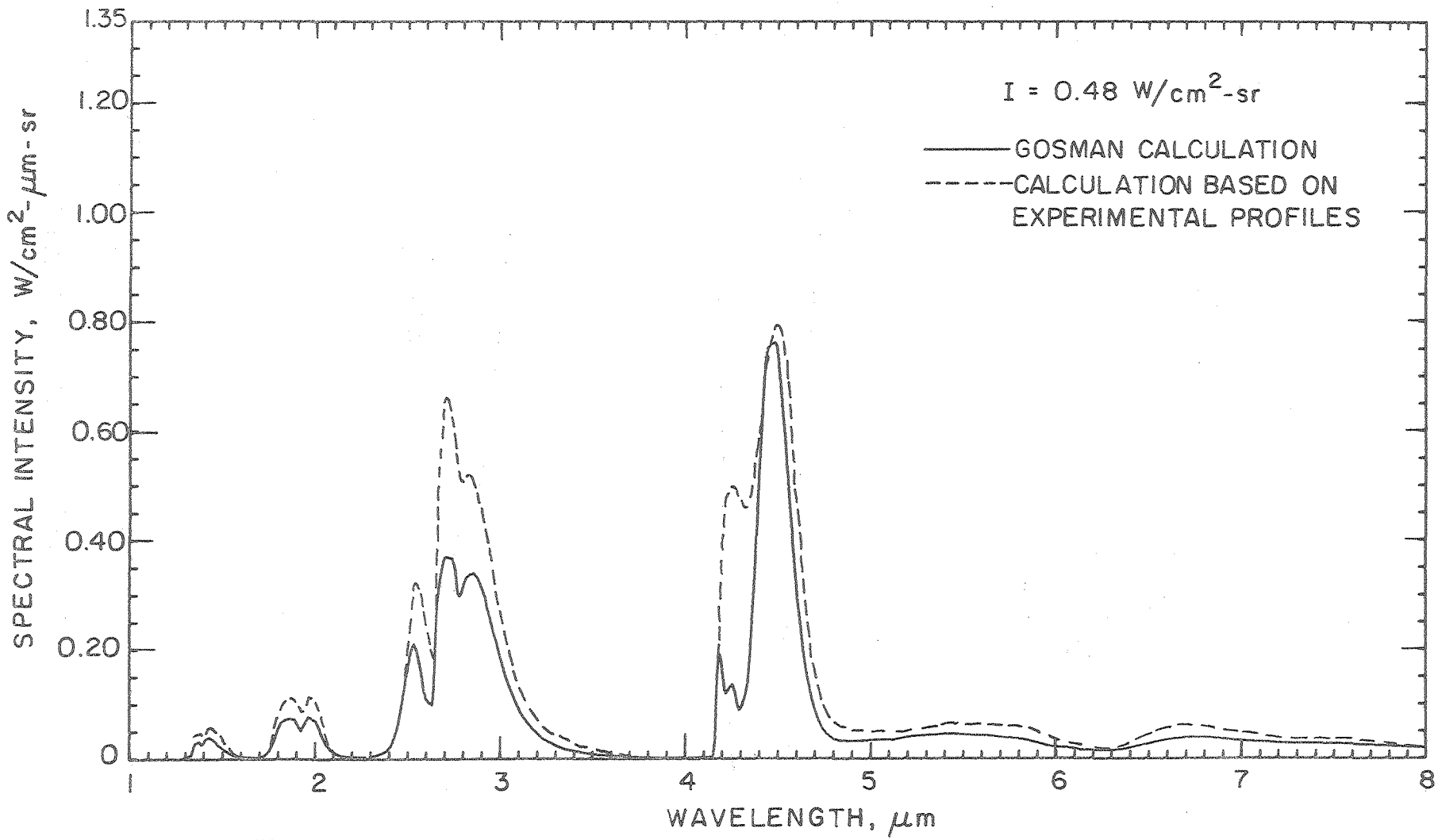

FIGURE VI-21. Calculated Spectral Intensity Using Furnace Conditions Predicted by Gosman Program (x = 58.9 cm)

Grosshandler (1976). The results are plotted on Figure VI-22 and compared to the non-homogeneous narrow band calculation of RADCALC. By its nature, a wide band model cannot predict the spectral intensity in the region of the band; however, the total integrated intensity can give a reasonable prediction. For this case the total intensity from HMIXRAD is .78 W/cm^2-sr as compared to .74 W/cm^2-sr from RADCALC, a remarkable agreement.

The total emittance at this same axial location has been determined based on these intensity calculations and compared to estimates from charts of Hottel (Hottel and Sarofim, 1967). The results are shown in Table VI-2.

TABLE VI-2. TOTAL NORMAL EMITTANCE OF PURE METHANOL FLAME AT X = 58.4 cm ($T = \overline{T^4}^{1/4}$)

Method	Emittance
Experimental Result	.098
RADCALC	.071
HMIXRAD	.078
Hottel Charts	.081

D. Comparison of Results to Those of Other Experimenters

The bulk of applied research into the parameters which affect furnace flame radiation has been done by the International Flame Research Foundation and dates back to the late 1940's. The results of the first trials at IJmuiden (J. Inst. Fuel, 1951 and 1952) deal with the effect of fuel type (fuel oil or creosote), the quantity of fuel, the atomizing agent (water or steam), the amount of atomizing agent, and the amount of excess air on the flame structure and radiation. Additional experiments carried out between 1951 and 1953 looked again at some of the same parameters and determined the effect of burner design (J. Inst. Fuel, 1953

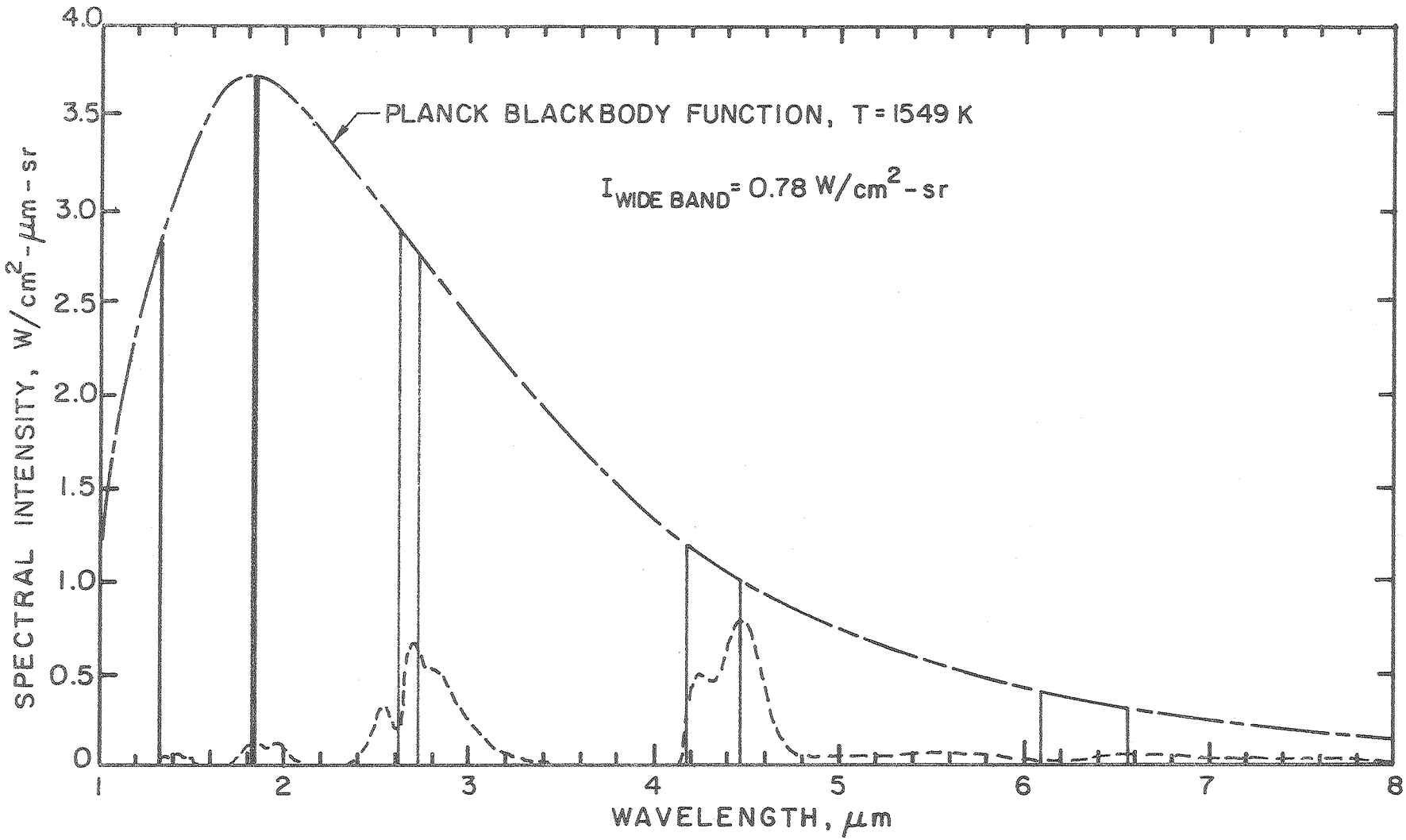

FIGURE VI-22. Calculated Intensity Using Wide Band Model and Average Homogeneous Conditions (x = 58.4 cm)

and 1957). Burning mixtures of liquid fuel with coke-oven gas was the subject of further tests (J. Inst. Fuel, 1956). Carbon black was added to gas oil and fuel oil in another set of experiments (J. Inst. Fuel, 1959) with the intent similar to that of the present experiment. In 1960, Beér and the Flame Research Foundation used a pressure jet burner in the IJmuiden furnace and studied the effect of adding a flame stabilizer disc on the radiation and structure of the flame (J. Inst. Fuel, 1962).

On a smaller scale, Holliday and Thring (1957) performed experiments at the University of Sheffield using a pressure jet burner. Their interest was the correlation of the average flame emissivity with fuel carbon to hydrogen ratio and boiling point. They were moderately successful in predicting emissivities of larger furnaces based upon experiments in their own smaller furnace.

Another important research group and experimental facility is at Kyoto University. Their work has dealt with measuring and predicting radiation heat transfer from luminous flames and high temperature particle clouds (Sato and Matsumoto, 1961; Sato and Kunitomo, 1965; Sato, Kunitomo, Nakashima, and Fujii, 1966; Sato and Kunitomo, 1969; Sato, Kunitomo, Yoshii, and Hashimoto, 1969). The most recent work is interesting since it is the only one which deals with the monochromatic distribution of radiation.

The problem of comparing results of the present study with other experimenters' is to find a common ground. No one has reported radiation measurements from a methanol flame and each experimenter has had a different size furnace with different burners and wall conditions. The best that can be done is to report all the results with these differences in mind.

If the intensity and emissivity are plotted as a function of length/diameter, the effect of the different furnace sizes is reduced. These are shown plotted in Figures VI-23a and 23b for seven different fuel systems. The intensity is non-dimensionalized on the incoming fuel energy rate, $\mathring{q}$, and the internal surface area of the furnace, A. This parameter can be viewed as the fraction of incoming energy which is transfered by radiation to the walls. Values greater than one are possible since the intensity used is the normal value which is greater than the average hemispherical value. Also, the entire unobstructed surface area of the cool walls is not available to each volume of gas.

Values for the present work are plotted with the solid symbols. The high value for emittance at L/D of .6 for the pure methanol flame is from the fuel droplets. At larger L/D ratios the emittance of the methanol/coal fuel is higher than that of the methanol, but the intensity is lower due to lower flame temperatures. The city gas study by Sato and Kunitomo shows an emittance larger than the present work, but their furnace is about twice as large. Coke-oven gas, which has less methane and more hydrogen than city gas, would have a lower emittance under similar experimental conditions, but the furnace of the International Flame Research Foundation has a cross-section five times that of the Kyoto furnace. The three experiments run with oil show the largest values for emittance and intensity. The emittance values determined by Holliday and Thring are surprisingly high considering the difference in size between the Sheffield and IJmuiden furnaces. The effect of adding 5.3% carbon black to the gas oil shows the expected increase in both emittance and intensity. If the three intensity curves excluding this study are extrapolated to large values of L/D, they will approach a common value of about .4. This can

a) Non-Dimensional Intensity

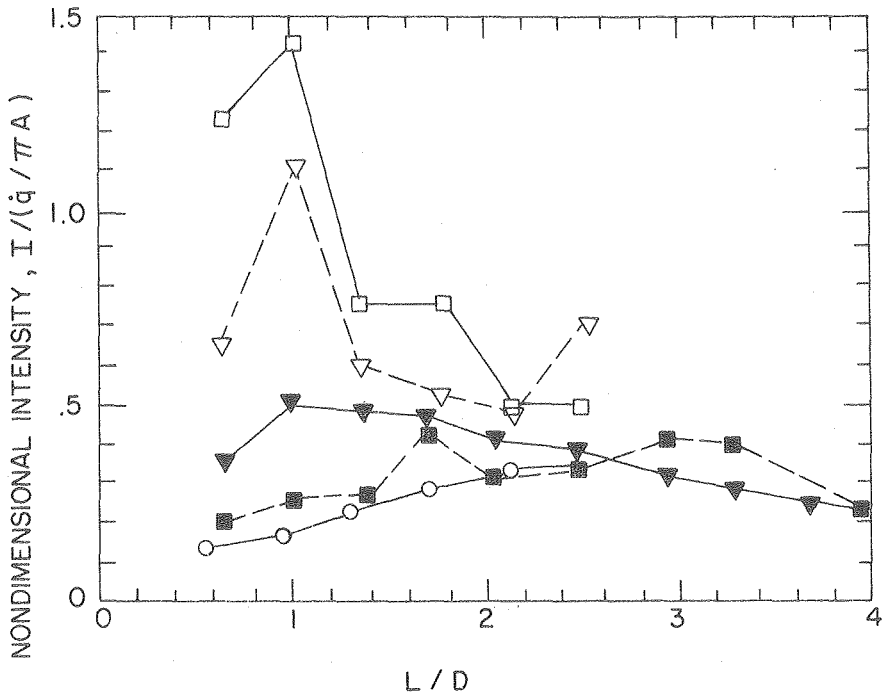

b) Total Emittance

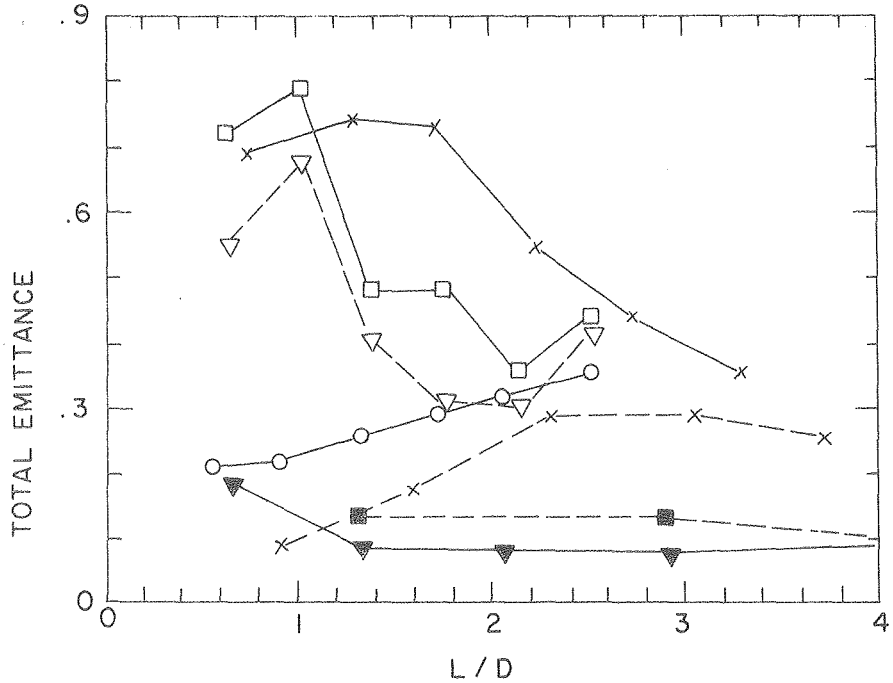

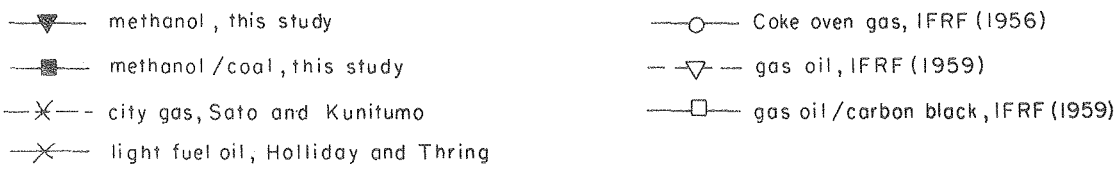

FIGURE VI-23. Intensities and Emittances of Various Fuels and Furnace Systems

be explained by the fact that the soot will have had time to burn completely and that the radiation will be dominated by the equilibrium combusted gas mixture, which varies little between hydrocarbon fuels. The intensity of the methanol furnace would likewise approach this value if its walls were adiabatic rather than water cooled.

The monochromatic distribution of emittance from city gas and heavy fuel oil burning in the Kyoto furnace is shown in Figure VI-24.(Sato, et al., 1969). This can be compared to the results shown in Figure VI-9. Ths 1.88 and 2.7 μm bands are similar for the gas and methanol fuels, but the 4.26 m band shows much more reabsorption by cold CO_2 in Sato's work. There is also no noticeable CO in the Kyoto furnace. The continuous particulate radiation is dominant for the heavy fuel oil and the wavelength dependence of the soot absorption coefficient can be seen.

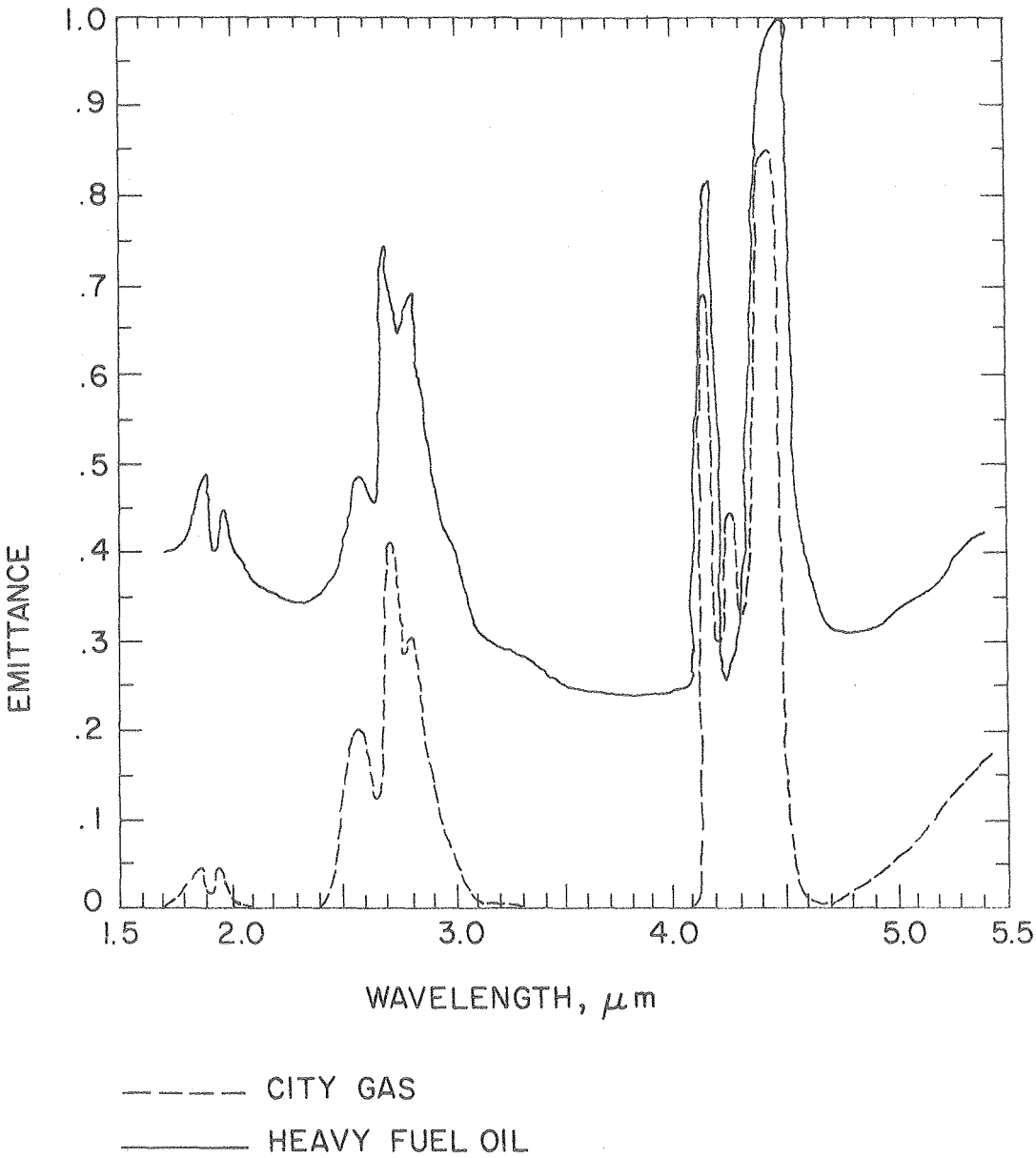

FIGURE VI-24. Spectral Emittance of a Furnace Burning City Gas or Heavy Fuel Oil (from Sato, et al., 1969)

VII. CONCLUSIONS

A. Summary of Results

A model water-cooled furnace has been built to study the structure and radiation heat transfer in a pure methanol flame and one burning a methanol/coal slurry. For pure methanol, the temperature and concentration of stable species have been mapped throughout the furnace. Concentrations of H_2O and CO_2 were found to approach their equilibrium values, but the temperatures measured were 200 K and more below the adiabatic flame temperature. The carbon monoxide conentrations were high early in the flame and decreased to about .4% by the furnace exit. Levels of NO were low throughout the furnace and were 15 ppm at the exit. Total NX concentration was less than 25 ppm. Methanol concentration was less than 1 ppm and formaldehyde was undetected in the exhaust. However, attempts to measure formaldehyde at levels less than 75 ppm were unsuccessful.

The addition of 5.3% coal had a significant effect on nitric oxide and total NX levels. These pollutants increased four-fold, which implies a 40% conversion of the coal bound nitrogen to NX. The temperature field was also changed when burning the slurry, but it has not been possible to separate the effect of the coal from the effect of the different fuel nozzles. Particulate levels in the exhaust were of the order of .1 g/m^3, as compared to less than .001 g/m^3 in the pure flame. At the furnace exit, temperature and CO_2 profiles of the two flames became similar.

The monochromatic radiation intensity has been measured for both fuel systems. No continuous particulate radiation was emitted from the methanol flame, but band emissions from CO_2, H_2O, CO and CH_3OH were observed. The maximum intensity was 1.64 W/cm^2-sr at an L/D ratio of 1.0. The effect of adding coal was to increase the total normal emittance from .098 to .135 due to the particles but to decrease the total intensity in the first half of the furnace due to lower temperatures. The contribution from the coal particles to the monochromatic intensity could be seen underlying the banded gas radiation.

Various models were used to compare the measured intensity with the calculated intensity. In most cases, the predicted intensities were about 25% low because none of the models accounted for radiation which eminated from the far wall. Total intensity calculations using a narrow band model with non-homogeneous path agreed with a wide band homogeneous path model. The particulate radiation was underestimated because of uncertainties in the particle size distribution and simplifications in the intermediate size particle range.

B. Conclusions

The following conclusions can be drawn from the present study:

1. The model furnace is a useful tool in comparing relative heat release rates, flame emittances, and pollutant formation for different fuels and operating conditions. Careful consideration of geometry and residence times must be taken to extrapolate absolute results to full scale systems.
2. Methanol can be burned in a furnace to produce low levels of oxides of nitrogen and soot without emitting high levels (less than 50 ppm) of formaldehyde.

3. Addition of small amounts of coal containing bound nitrogen to a methanol diffusion flame will increase the NO levels.
4. A computer code was developed for the prediction of the spectral intensity along a known non-homogeneous path with negligible radiation from the boundaries.
5. The infrared spectra of a methanol diffusion flame contains no significant particulate radiation.
6. The emittance of a furnace burning methanol can be enhanced by the addition of pulverized coal to the fuel.
7. The fluid mechanical structure of a furnace burning a methanol/coal slurry is as important in controling the radiant intensity as is the amount of coal in the slurry.

REFERENCES

Adelman, G., D.G. Andrews and R.S. Devoto, "Exhaust Emission from a Methanol Fueled Automobile," SAE Paper 720693, August, 1972.

Allen, J.D., Billingsley and J.T. Shaw, "Evaluation of the Measurement of Oxides of Nitrogen in Combustion Products by the Chemiluminescence Method," J. Inst. Fuel 42, 275 (1974).

Altenkirk, R. and A.M. Mellor, "Predicting Emissions from Prevaporizing Combustors via Continuum Flow Techniques," Western States Section/ The Combustion Institute, Fall 1975.

Babcock and Wilcox Company, Steam: Its Generation and Use, Babcock and Wilcox Company, N.Y., 1963.

Bagwell, F.A., K.E. Rosenthal, D.P. Teixera, B.P. Breen, N. deVolo, S. Kerho, "Utility Boiler Operating Modes for Reduced Nitric Oxide Emissions," J. Air Pollution Control Association 21, 703 (1971).

Barr, W.H. and D.E. James, "Nitric Oxide Control--A Program of Significant Accomplishments," ASME, Winter Meeting, 1972.

Barrow, G.M., Molecular Spectroscopy, McGraw-Hill Book Company, Inc., (1962).

Beér, J.M. and N.A. Chigier, Combustion Aerodynamics, Applied Science Publishers, Ltd., Essex, (1972).

Bradley, D. and K.J. Matthews, "Measurement of High Gas Temperatures with Fine Wire Thermocouples," J. Mech. Eng. Sci. 10, 299 (1968).

Cernansky, N.P., "Formation of NO and NO_2 in a Turbulent Propane/Air Diffusion Flame," University of California, Berkeley, Mechanical Eng. Report ME-74-5, 1975.

Colket, M.E., D.W. Naegeli, F.L. Dryer, and I. Glassman, "Flame Ionization Detection of the Carbon Oxides and Hydrocarbon Oxygenates," Envir. Sci. and Tech., 43, Jan. 1974.

Combustion Engineering, Glenn Fryling, Ed., Combustion Engineering, N.Y. 1966.

Dalzell, W.H. and A.F. Sarofim, "Optical Constants of Soot and Their Application to Heat-Flux Calculations," J. Heat Tranfer 91, 100, (1969).

Felske, J.D. and C.L. Tien, "Calculation of the Emissivity of Luminous Flames," Comb. Sci. and Tech. 7, 25 (1973).

Foster, P.J. and C.R. Howarth, "Optical Constants of Carbons and Coals in the Infrared," Carbon 6, 719 (1968).

Fristrom, R.M. and A.A. Westenberg, Flame Structure, McGraw-Hill, N.Y., 1965.

Goody, R.M., Atmospheric Radiation I, Theoretical Basis, Oxford at the Clarendon Press, 1964.

Gordon, S. and B.J. McBride, Computer Program for Calculation of Complex Chemical Equilibrium Composition, Rocket Performance, Incident and Reflected Shocks, and Chapman-Jouget Detonations, NASA SP-273, 1971.

Gosman, A.D., W.M. Pun, A.K. Runchal, D.B. Spaulding and M. Wolfshtein, Heat and Mass Transfer in Recirulating Flows, Academic Press, 1969.

Grosshandler, W.L., " A Study of a Model Furnace Burning Methanol and a Methanol/Coal Slurry," Ph.D. Thesis, Department of Mechanical Engineering, University of California, Berkeley, 1976.

Handbook of Chemistry and Physics, Chemical Rubber Publishing Company, Cleveland, Ohio, 1972.

Herzberg, G., Spectra of Diatomic Molecules, Vol. II, Van Nostrand, Princeton, N.J., 1950.

Herzfeld, C.M. (Editor in Chief), Temperature: Its Measurement and Control in Science and Industry V3, 2, Reinhold Publishers, N.Y., 1961.

Hiller, H., F. Marschner, and E. Supp, "The Lurgi Low Pressure Methanol Process," and "The ICI Low Pressure Methanol Process," Chem. Econ. and Eng. Review 3, 9 (1971).

Holliday, D.K. and M.W. Thring, "The Radiation from Flames in a Small-Scale Oil-Fired Furnace," J. Inst. Fuel 30, 127 (1957).

Holman, J.P., Heat Transfer, 3rd Edition, McGraw-Hill Book Company, 1972.

Hottel, H.C. and A.F. Sarofim, Radiative Transfer, McGraw-Hill Book Co., 1967.

Hubbert, M. King, "The Energy Resources of the Earth," Scientific America 224, 60, (1971).

International Flame Research Foundation, "1949 Performance Trials at IJmuiden," J. Inst. Fuel 24, S.1 (1951).

International Flame Research Foundation, "1949 Performance Trials at IJmuiden," J. Inst. Fuel 25, S.17 (1952).

International Flame Research Foundation, "Flame Radiation Research Joint Committee: Reports of Burner Trials at IJmuiden," J. Inst. Fuel 26, 189 (1953).

International Flame Research Foundation, "The Radiation from Turbulent Jet Diffusion Flames of Liquid Fuel/Coke-Oven Gas Mixtures," J. Inst. Fuel 29, 23 (1956).

International Flame Research Foundation, (Riviére, M.), "The Influence of Mixing Conditions on Flame Characteristics, Performance Trials No. VI, Carried out on Original Furnace," J. Inst. Fuel 30, 556 (1957).

International Flame Research Foundation, (E.H. Hubbard), "Comparison of Different Methods of Fluid-Atomizing Oil Flames and the Effect on Flame Emissivity and Radiation of the Addition of Carbon Black to Liquid Fuels," J. Inst. Fuel 32, 328 (1959).

International Flame REsearch Foundation, (Beér, J.M.), "Some Results of the First Trials on Pressure Jet Oil Flames in the IJmuiden Furnace," J. Inst. Fuel 35, 3 (1962).

Kaskan, W.E., "Dependence of Flame Temperature on Mass Burning Velocity," Sixth Symposium (International) on Combustion, 134, Reinhold, N.Y., (1957).

Kent, J.H., "A Noncatalytic Coating for Platinum-Rhodium Thermocouples," Combustion and Flame 14, 279 (1970).

Kent, J.H. and R.W. Bilger, "Measurement Techniques in Turbulent Diffusion Flames," First Australasian Conference on Heat and Mass Transfer, 1973.

Ludwig, C.B., W. Malkmus, J.E. Reardon, and J.A. Thompson, Handbook of Infrared Radiation From Combustion Gases, NASA SP-3080, 1973.

Malkmus, W., "Infrared Emissivity of Carbon Dioxide (2.7-μ Band)," General Dynamics/Astronautics AE63-0047, 1963.

Malkmus, W., "Infrared Emissivity of Carbon Dioxide (4.3-μ Band)," J. Optical Soc. America 53, 951 (1963).

Malkmus, W. and A. Thompson, "Infrared Emissivity of Diatomic Gases for the Anharmonic Vibrating-Rotator Model," J. Quant. Spectrosc. and Radiat. Transfer 2, 17 (1961).

Matthews, R.D., O.J. Smith, N.J. Brown, and R.F. Sawyer, "Measurement of Low Molecular Weight Nitrogen Compounds in Flame Systems," Western States Section/The Combustion Institute, Fall 1975.

Milne, T.A., F. Greene and J. Beachey, "Pulverized Coal Combustion Studies on Flat Flame Burners," Western States Section/The Combustion Institute, Spring 1974.

Morita, A. H. Takahashi, and T. Koseki, "Methanol Production by JGCC Process," Chem. Econ. and Eng. Rev. 3, 23 (1971).

Pacific Gas and Electric Company, "Pittsburg Power Plant, Units 1-7," PG&E.

Pagni, P.J., "Analysis of Particulate Pollution," Combustion Sources of Air Pollution and Their Control, University Extension and College of Engineering, University of California, Berkeley, 1973.

Patterson, J.A., M.W. McElroy, R.F. Sawyer, and T. Singh, "A Prototype Chemiluminescent NO Anlayzer," University of California, Berkeley, Report No. TS-70-9.

Penner, S.S., "Infrared Emissivity of Diatomic Gases," National Bureau of Standards Circular No. 523, 1954.

Pitz, R., R. Cattolica, F. Robben, and L. Talbot, "Premixed Hydrogen-Air Flame Temperature from Rayleigh Scattering," Combustion and Flame (to be published).

Pratt, D.T., "Combustion of Ammonia and Air in a Well-Stirred Reactor," University of California, Berkeley, Report No. TS-68-3, 1968.

Reed, T.B. and R.M. Lerner, "Methanol: A Versatile Fuel for Immediate Use," Science 182 (1973).

Rudzki, E.M., B.K. Pease and T.H. Weidner, "Use of Coal-in-Oil Mixtures to Improve Open-Hearth Furnace Performance," J. Inst. Fuel 38, 154 (1965).

Samuelsen, G.S., "Analytical and Experimental Investigation of an Ammonia/Air Opposed Reacting Jet," University of California, Berkeley, Report No. TS-70-10, 1970.

Sato, T. and T. Kunitomo, "Radiation from Fine Particle Clouds in High-Temperature Combustion Gas," Memoirs of Faculty of Engr., Kyoto University, 27, Part I, 75 (1965).

Sato, T. and T. Kunitomo, "Experimental Study on Luminous Flame," Memoirs of Faculty of Engr., Kyoto University 31, Part I, 47 (1969).

Sato, T., T. Kunitomo, F. Nakashima, and H. Fujii, "Study on Radiation from Luminous Flame," Bul. Japan Soc. Mech. Engr. 9, 768 (1966).

Sato, T., T. Kunitomo, S. Yoshii, and T. Hashimoto, "On the Monochromatic Distribution of the Radiation from the Luminous Flame," Bul. of Japan Soc. Mech. Engr. 12. 1135 (1969).

Sato, T. R. Matsumoto, K. Veda and K Ohira, "Radiant Heat Transfer from Luminous Flame," (Japanese), Trans. Japan Soc. Mech. Engr. 26, 177 (1961).

Schefer, R.W., "Pollutant Formation in Fuel Lean Recirculating Flows," University of California, Berkeley, Mech. Engr. Report No. UCB-ME-76-5, 1976.

Schefer, R.W., R.D. Matthews, N.P. Cernansky, and R.F. Sawyer, "Measurement of NO and NO_2 in Combustion Systems," Western States Section/ The Combustion Institute, Fall 1973.

Siegel, R. and J.R. Howell, Thermal Radiation Heat Transfer, McGraw-Hill Book Company, 1972.

Steinberg, M., F. Salzano, M. Beller, and B. Manowitz, "Methanol as a Fuel in the Urban Energy Economy and Possible Source of Supply," Brookhaven National Laboratory 17800, April, 1973.

Street, J.C. and A. Thomas, "Carbon Formation in Premixed Flames," Fuel 34, 4 (1955).

Tani, M. and T. Fukawa, "Nissui-Topsoe Intermediate-Pressure Methanol Synthesis Process Using New Catalyst," Chem. Econ. and Engr. Rev. 3, 17 (1971).

Tien, C.L., " Thermal Radiation Properties of Gases," Advances in Heat Transfer 5, 253, Academic Press Inc., N.Y., 1968.

Tien, C.L. and J.H. Lienhard, Statistical Thermodynamics, Holt, Reinhart, and Winston, Inc. 1971.

Tien, C.L. and J.E. Lowder, "A Correlation for Total Band Absorbtance of Radiating Gases," Int. J. Heat Mass Trans. 9, 698 (1965).

Turner, D.W., R.L. Andrews and C.W. Siegmund, "Influence of Combustion Modification and Fuel Nitrogen Content on Nitrogen Oxides Emissions from Fuel Oil Combustion," Combustion, 21, August, 1972.

Zolner, W.J., "The Measurement of Ammonia Utilizing the Thermo Electron Chemiluminescent Analyzer," Application Note 72-1, Thermo Electron Corporation.

This report was done with support from the United States Energy Research and Development Administration. Any conclusions or opinions expressed in this report represent solely those of the author(s) and not necessarily those of The Regents of the University of California, the Lawrence Berkeley Laboratory or the United States Energy Research and Development Administration.

0 0 0 0 4 5 0 2 2 9 4